Engineering High Capacity Alternative Ion Battery Electrodes Through Mechanistic Insight

By

Keith Share

Dissertation

Submitted to the Faculty of the

Graduate School of Vanderbilt University

in partial fulfillment of the requirements

for the degree of

DOCTOR OF PHILOSPHY

in

Interdisciplinary Materials Science

May 31, 2018

Nashville, Tennessee

Approved:

Cary L. Pint, PhD
Sharon Weiss, PhD
D. Greg Walker, PhD
David Cliffel, PhD
Richard Haglund, PhD

ACKNOWLEDGEMENTS

I would like to thank my advisor, Prof. Cary Pint for bringing me to Vanderbilt and passing on knowledge that has made my work both higher quality and more interesting. Thanks for providing me the flexibility to find and follow my own passions in the research world. I would also like to thank my dissertation committee: Prof. Sharon Weiss, Prof. Greg Walker, Prof. David Cliffel, and Prof. Richard Haglund for their support and feedback during my PhD research.

Thanks to the members of the Pint lab, both past and present, who have brought excitement and laughs into the lab. Specifically, thanks to Landon Oakes and Shahana Chatterjee for patiently training me on practically all of the lab equipment when I started. Thank you, Adam Cohn and Rachel Carter, for their open and critical discussions about research. Also, thank you Rachel and Kate Moyer for their help with TEM. The images they took were crucial to many of my projects. Big thanks to my other lab mates Nitin Muralidharan, Andrew Westover, Anna Douglas, Mengya Li, and Janna Eaves for their insight during group meeting. Especially big thanks go to Janna for her help networking. Thanks to the Prof. Rizia Bardhan and the members of her lab, Will Erwin, Joe Webb, Holly Zarick, and Naiya Soetan for allowing me to use their lab and get in their way.

I would like to thank Jack Lewis and Supriyadi Tasim, the undergraduates that I worked with who helped with my research.

Thank you to the National Science Foundation Graduate Research Fellowship (NSF GRFP) for providing financial and curricular support. This fellowship was critical to achieving my accomplishments in graduate school because of the support and flexibility it provided me.

Thanks to the Vanderbilt Institute of Nanoscale Science and Engineering staff for training me and maintaining so many valuable tools. Using that equipment was some of the most interesting and exciting work I did. Specifically, thanks to Ben Schmidt, Tony Hmelo, Alice Leach, and Bill Martinez.

My climbing friends and family were an invaluable part of my time in Nashville. Thanks to my parents for their guidance and support. Thanks to my sister Cara and brother-in-law Matt for raising my nephew Jonah to be such a funny and amazing kid. Lastly, I would like to thank my girlfriend Ellis and dog Han for their support and helping me to take a step back and laugh more often.

TABLE OF CONTENTS

Page

LIST OF FIGURES

Figure Page

LIST OF ABBREVIATIONS

ANL – Argonne National Lab
CDI – capacitive deionization
CMC – carboxymethyl cellulose
CV – cyclic voltammetry
CVD – chemical vapor deposition
d-FLG – defective few-layer graphene
DFT – density functional theory
DOE – Department of Energy
EDS – electron dispersive x-ray spectroscopy
EV – electric vehicle
DEC – diethyl carbonate
EC – ethylene carbonate
EDS – energy dispersive x-ray spectroscopy
FLG – Few-layer graphene
FWHM – Full width at half maximum
G_c – Charged G peak
GIC – graphite intercalation compound
GITT – galvanostatic intermittent titration technique
G_{uc} – Uncharged G peak
LIB – lithium ion battery
LSV – linear sweep voltammetry
N-5 – pyrrole-like nitrogen
N-6 – pyridine-like nitrogen
N-FLG – Nitrogen doped few-layer graphene
N-Q – graphitic nitrogen
NCA – $Ni_xCo_yAl_zO_2$
NMC – $Ni_xMn_yCo_zO_2$
NMP – n-methyl-2-pyrrolidone
NP – nanoparticle
PC – propylene carbonate
PIB – potassium ion battery
PVDF – polyvinylidene fluoride
RO – reverse osmosis
SCE – saturated calomel electrode
SEI – solid electrolyte interface
SEM – Scanning electron microscope
SIB – sodium ion battery
TEM – transmission electron microscope
TMD – transition metal dichalcogenide
XPS – X-ray photoelectron spectroscopy
XRD – X-ray diffraction

LIST OF PUBLICATIONS

Portions of this dissertation have been drawn from the following publications:

1. **Share, K.;** Lewis, J.; Oakes, L.; Carter, R.E.; Cohn, A.P.; Pint, C.L. "Tungsten Diselenide (WSe_2) as a High Capacity, Low Overpotential Conversion Electrode for Sodium Ion Batteries." *RSC Adv.* 5 (123) **2015**, 101262-101267.
2. **Share, K.;** Moyer, K.; Muralidharan, N.; Cohn, A.P.; Pint, C.L. "Tuning Silver Nanoparticle Size to Reduce Energy Consumption of a Desalination Battery." *In Submission*
3. **Share, K.;** Cohn, A.P.; Carter, R.E.; Pint, C.L. "Mechanism of Potassium Ion Intercalation Staging in Few Layered Graphene from in-situ Raman Spectroscopy." *Nanoscale*, 8 (136), **2016**, 16435-16439
4. **Share, K.;** Cohn, A.P.; Carter, R.E.; Rogers, B.; Pint, C.L.; "Role of Nitrogen-Doped Graphene Growth: Mechanistic Insight from in-situ Raman Spectroscopy." *ACS Nano*. 10 (10), **2016**, 9737-9744

Chapter 1 Introduction

1.1 Economic and Environmental Motivation for Renewables

For both economic and environmental reasons, the global energy infrastructure has begun to change from a fossil fuel base to a renewable and distributed system. Initially environmental reasons, such as mitigating CO_2 emissions, were the driving forces to produce energy from renewable sources such as solar, wind, biofuels and hydroelectric. As these technologies and policies regarding them have evolved, there is now an additional economic incentive. Solar and wind are now the same price or cheaper in over thirty countries (Figure 1.1).[1]

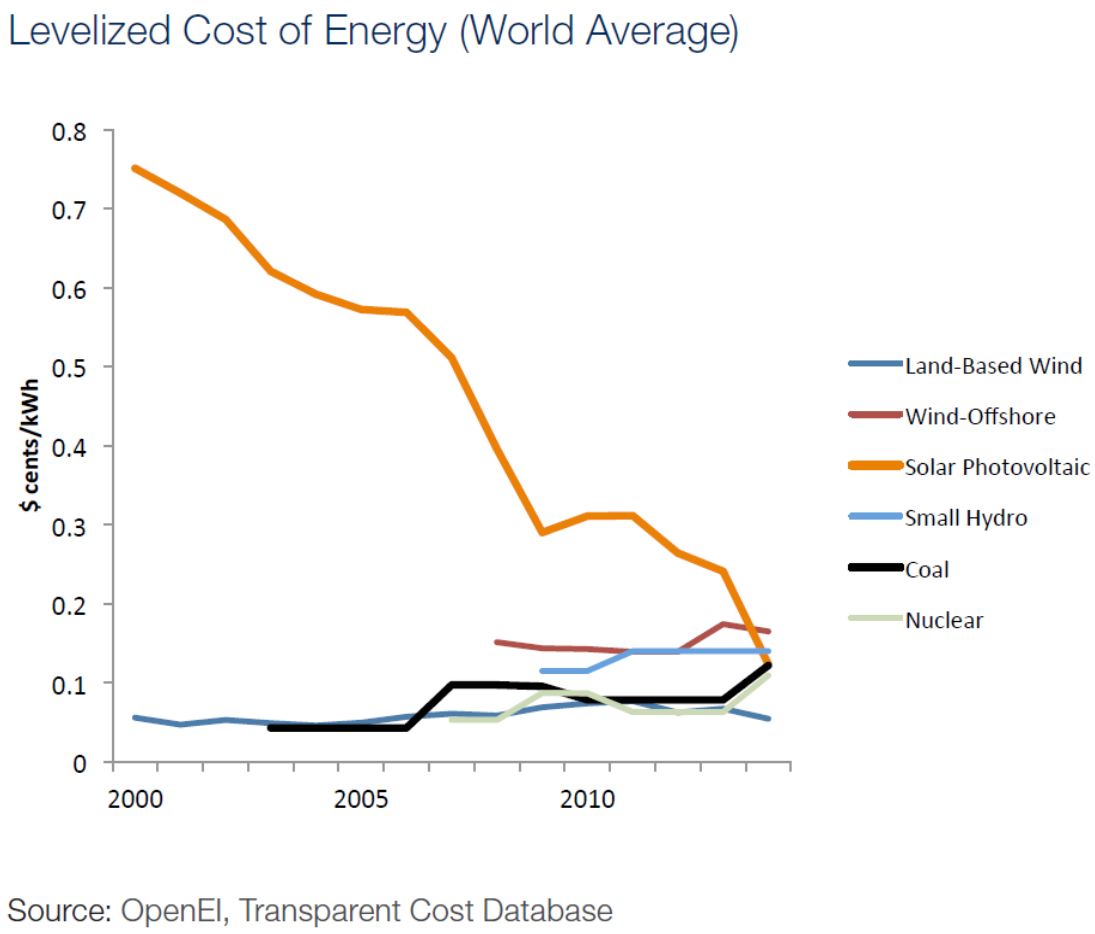

Figure 1.1 Levelized cost of energy for power generation

Even states that rely heavily on the coal and gas industry such as Texas understand the economic importance of renewables as they are also the largest wind producing state. Under Governor Rick Perry (now Secretary of Energy) wind power surged, with over eighteen GW installed and another five GW under construction according to the American Wind Energy Association.[2, 3] Competitive energy costs completely change the incentive of renewables from environmental to an economic driver that can provide both jobs and cheaper energy. In fact, in Q1 and Q2 of 2016, 374,000 solar jobs were added in the US, more than in the generation of nuclear, fossil fuels, or advanced gas (Figure 1.2).[4]

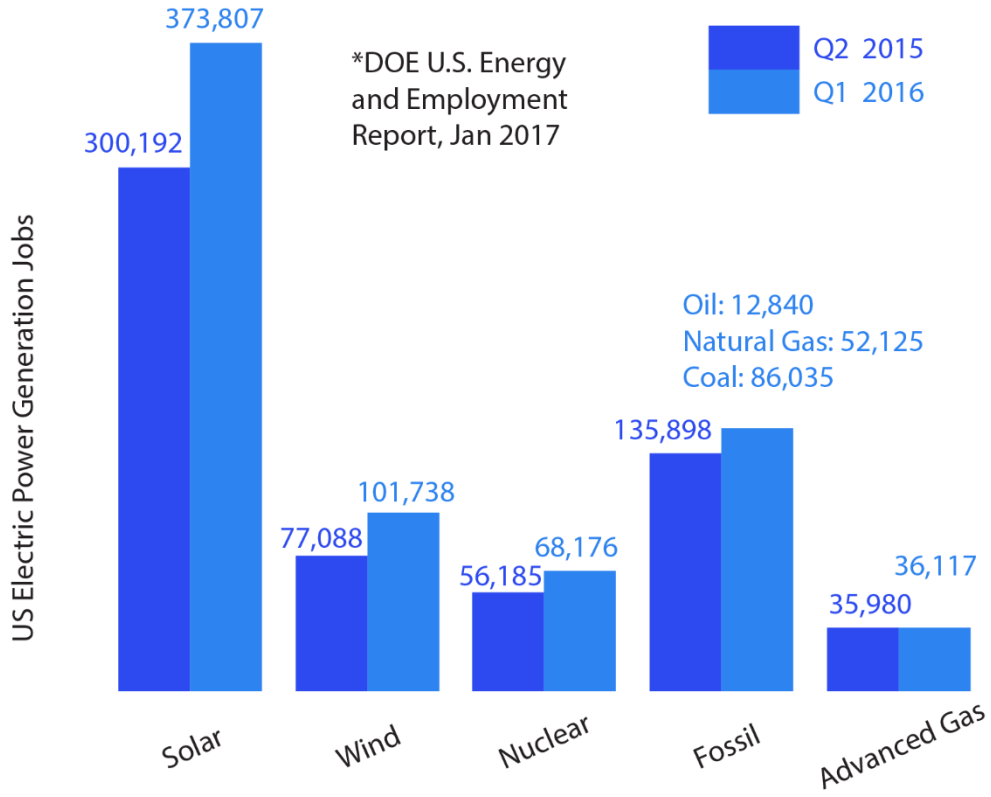

Figure 1.2 New jobs related to power generation broken down by industry

One of the biggest changes from coal and natural gas power generation to renewable generation is the ability to provide energy on demand. Coal and natural gas plants can ramp up and down as needed and there are plants designed to specifically come online when demand is high. This is not the case for

renewables since it is much more difficult to tell the sun to shine or the wind to blow. A crucial part of the renewable infrastructure is the storage and release of these intermittent. Also, as more wind and solar are installed, a larger percentage of the power produced from these sources is wasted because of its unpredictability, known as curtailment (Figure 1.3a).[5, 6] Batteries are the solution to these problems. Batteries are needed for both short term and long term storage of energy when there is excess and releasing power to the grid when needed (Figure 1.3b).[7] Unfortunately, batteries were not a major focus during the boom of wind and solar so the cost and performance of batteries is insufficient for renewable grid storage.

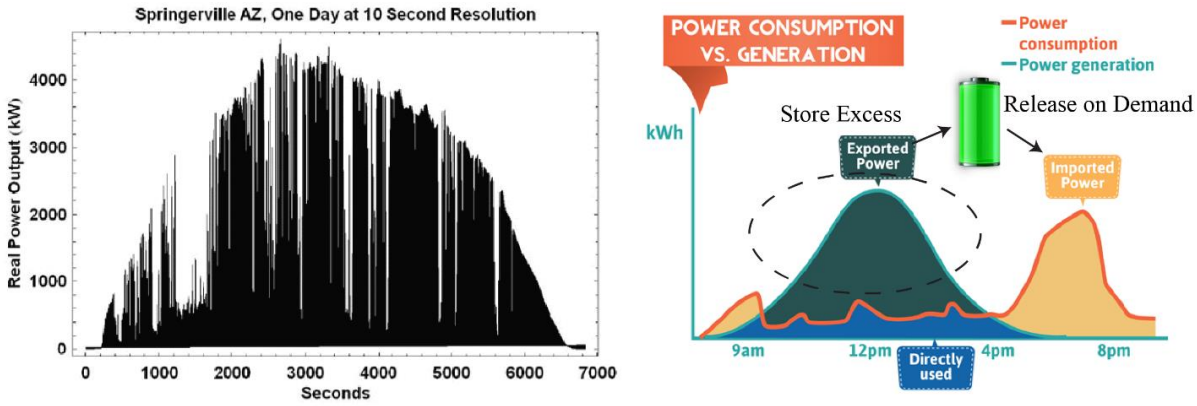

Figure 1.3 a) Real power output data from Tucson Electric Power over one full day in summer (3 June 2004) at one min sampling frequency. b) Excess solar produced during that day that can be stored and released by batteries in demand

Another growing application for batteries is electric vehicles (EVs), requiring over 20 GWh of lithium ion batteries (LIBs) in 2016 with over 400 GWh expected in 2025.[8] Although EVs are becoming more popular in the US, foreign nations are the main driving forces. The United Kingdom and France have announced that by 2040 gasoline and diesel cars will not be sold in their countries. The Chinese government has proposed production quotas on their auto manufacturers with the goal of generating a market for 5 million new energy cars between 2016 and 2020.[9] The market in the US is dominated by Tesla and Panasonic who have partnered on the Tesla Gigafactory with an expected production of

500,000 EVs per year. Batteries are still prohibitively expensive in full electric vehicles, to the point where the annualized cost to the consumer is higher for full electric vehicles than hybrid electric or combustion vehicles.[10] This means that the upfront price of the battery is so high that it is not balanced by the gas savings over the lifetime of the car. A sensitivity analysis of EV costs on battery price shows that meeting the DOE 2030 price goal would make EVs cost competitive with other technologies (Figure 1.4). The battery price is critical for full electric vehicles to have both economic and environmental benefits and to become a competitor in the transportation market.

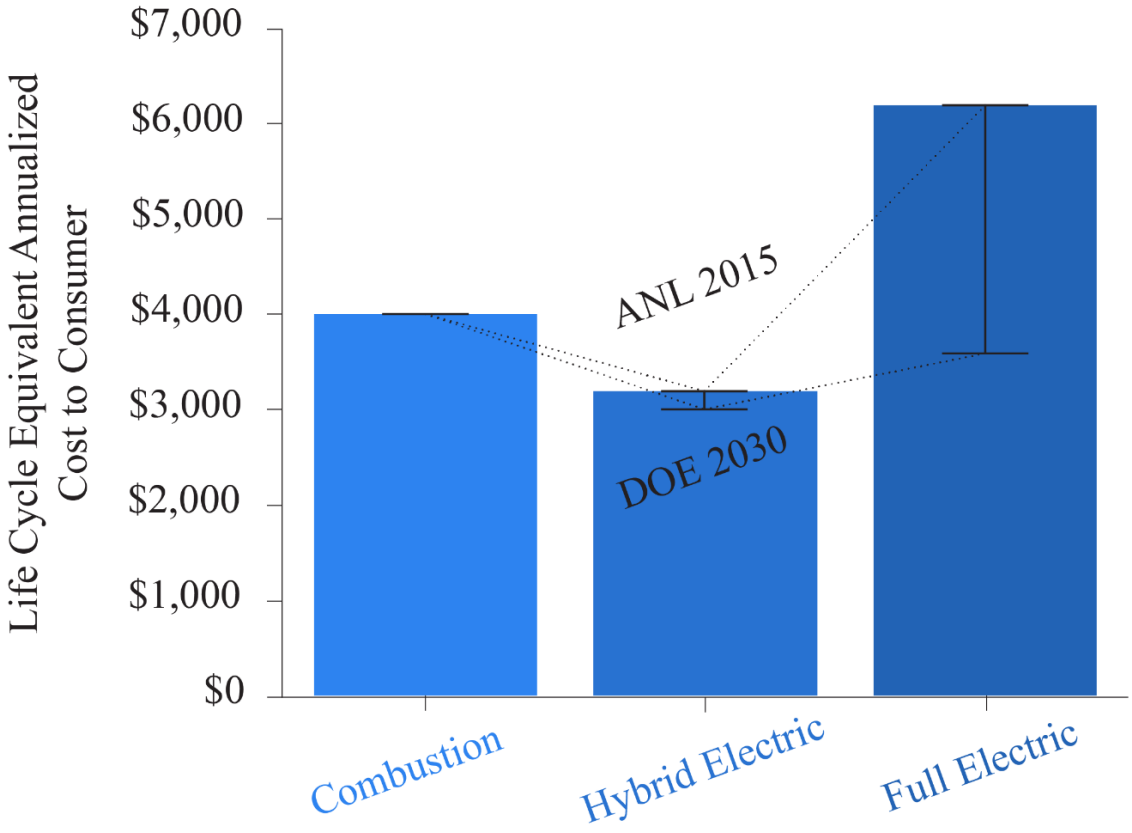

Figure 1.4 Sensitivity Analysis of Battery Cost on Annualized Cost to Consumer for City Driving. Reproduced from ref. [10] with permission from Elsevier

The growing importance of both renewable energy and electric vehicles has dramatically increased the demand for batteries, particularly lithium ion batteries.[11] Unfortunately, the cost and performance of LIBs both need to be improved before batteries can really thrive in EV and renewable applications. I decided to get my PhD to specifically tackle these issues. Before graduate school I had worked at a solar cell and panel manufacturer and it became clear that competitive solar technologies existed while competitive batteries did not. One of my favorite parts of my job was the interdisciplinary nature of the work where I learned new ideas in chemistry, physics, statistics, and more. In graduate school I tried to continue this by learning about many different fields. My dissertation will focus on methods to produce a less expensive battery with new materials for alternative ion batteries. My research has been guided by trying to solve the main engineering challenges of these systems by first understanding the fundamental storage mechanisms and then leveraging that knowledge to improve the performance.

1.2 The Lithium Ion Battery

The battery technology best poised for both EVs and renewable storage is the lithium ion battery. The modern LIB was invented in 1976 by Stanley Whittingham who found that lithium ions could be shuttled back and forth between high energy lithium metal (the anode) and low energy TiS_2 (the cathode).[12] Despite his discovery, commercial success of this design was limited due to the instability of lithium metal both in air and upon repeated stripping and plating while the battery was being used. It was not until after the replacement of the cathode with $LiCoO_2$ and the anode with graphite in the 1990s that Sony was able to manufacture the modern LIB. These materials are still commonly used in LIBs today, although development of alternative cathodes such as $LiNi_{1-x-y}Mn_xCo_yO_2$ (NMC) and $LiNi_{1-x-y}Co_xAl_yO_2$ (NCA) can provide energy, cost, and safety benefits.[13]

A LIB operates by shuttling Li^+ through a lithium salt containing electrolyte between electrodes in a high energy and low energy state. Using a charged $LiCoO_2$/graphite LIB as an example (Figure 1.5), in

a charged state, the lithium ions are stored in the anode as LiC_6 while the cathode has the lithium deficient state of $Li_{0.5}CoO_2$. Upon discharging lithium ions and electrons are removed from the graphite at ~0.1 V vs Li/Li^+. The lithium ions then travel through the electrolyte to the cathode while the electrons travel through an external circuit and provide power to the car, house, or any attached device. The e^- then reduces Co^{3+} to Co^{2+} and the Li^+ is inserted into the cathode to maintain charge balance at ~4V vs Li/Li^+. (voltage and energy are inversely related, so a higher voltage means the electrons are lower energy). The voltage difference between the two electrodes is the operating voltage of the battery which must be smaller than the electrochemical window of the electrolyte otherwise the electrolyte will be depleted through oxidation or reduction. The number of ions stored in an electrode is referred to as its capacity and is reported in mAh/g (a fancy way of stating the amount of charge stored per mass of electrode). $LiCoO_2$ can only reversibly form $Li_{0.5}CoO_2$ yielding a capacity of 136 mAh/g. Further Li^+ removal causes irreversible structural changes. Graphite on the other hand has a theoretical capacity of 372 mAh/g when forming LiC_6.

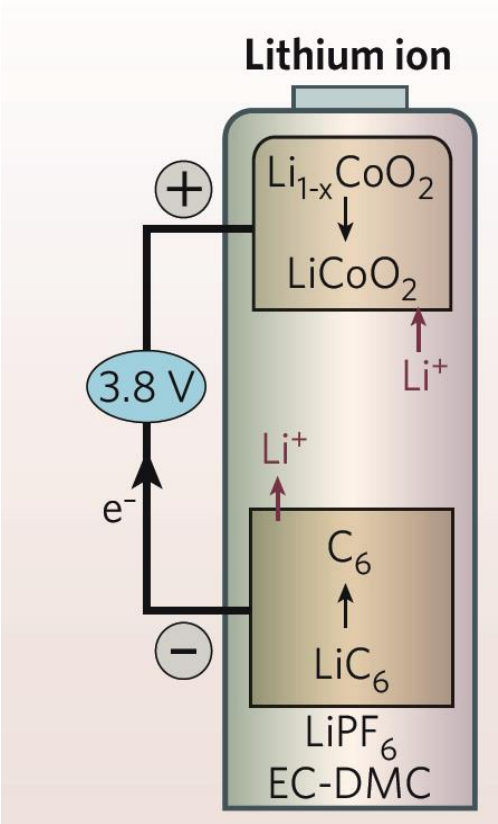

Figure 1.5 Operation of a standard lithium ion battery upon discharge. Reproduced from ref. [11] with permission from Nature

1.2.1 Challenges for Lithium Ion Batteries

As LIB demand is rapidly increasing there are mounting cost and material concerns. Lithium is the 33rd most abundant element and is not well distributed in the earth's crust, both of which contribute to its relatively high price (Figure 1.6).[14] Although Australia is the biggest exporter of lithium, most of the reserves are found in Chile and China, countries that can be politically challenging for the US to work with.[15] For these reasons, concern has arisen about potential Li shortages and price increases in the future. Although there is enough Li on Earth to meet the near term demands for LIBs, there is a major lag time between building a mine and exporting lithium. The demand for batteries is rapidly increasing due

to EV sales and storage of renewables and if the mining operation cannot keep up, the price of Li will drastically increase.[16]

Figure 1.6 Major lithium deposits

Another limitation of current LIBs is that the general design has not changed much since its initial introduction in the 90s. The cost of LIBs has dropped due to cell technology advancement and economies of scale, but they are closing in on their minimum. Further advances in energy density and cost must come from materials changes.

1.3 Alternative Ion Batteries

The challenges facing LIBs has motivated the field of alternative ion batteries that substitute lithium with more abundant metals whose raw material costs are well below that of lithium, such as sodium,[17, 18] potassium,[19-22] or aluminum.[23] Sodium, potassium, and lithium are all alkali metals and in many cases, this enables direct application of knowledge gained from LIB research to be readily applied in sodium ion battery (SIB) and potassium ion battery (PIB) systems since common cathodes, such as transition metal oxides or phosphates, have Na or K equivalents.[18,4,24] Sodium and potassium are around 800 times more abundant and around twenty times cheaper than Li while also having a wider distribution

in the earth's crust (Figure 1.7a,b).[18, 25] These alternative ion batteries operate very similarly to a LIB where the ion is inserted and extracted from two electrodes, but new challenges arise mostly due to the larger ionic radii of the K^+ and Na^+.

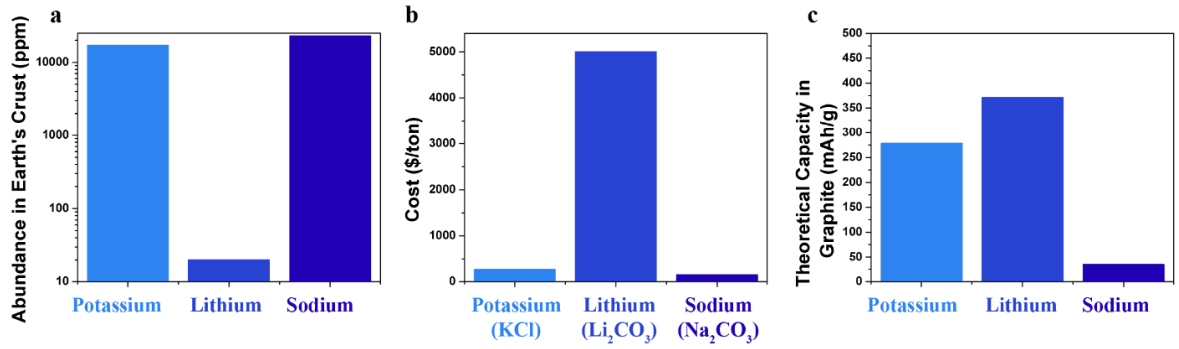

Figure 1.7 a) Abundance in the earth's crust. b) Cost of relevant precursors. c) theoretical capacity in graphite

1.3.1 Challenges for Sodium Ion Batteries

The major challenge for SIBs arises from the lack of Na^+ storage in graphite. While graphite has a capacity of 372 mAh/g in an LIB, it only has a capacity of 37 mAh/g in a SIB because only NaC_{60} can be formed (Figure 1.7c).[26, 27] Sodium is unique in its inability to be stored in graphite in large quantities, since many other graphite intercalation compounds can be formed with larger cations and anions such as K^+, $AlCl_4^-$, Cs^+, and others.[28-30] The origin of the low sodium capacity in graphite arises from the diverging trends between ionization energy, binding energy, and carbon straining in increasing alkali and alkali earth metals. Even though larger ions have a higher carbon strain energy, they also have a much more favorable decohesion and binding energy that allows for a favorable formation energy. For Na^+ however, the less favorable binding energy becomes the driving force for poor formation energy.[31]

This underlines the need for the exploration of new electrode materials for SIBs that can be competitive in performance with commercially available lithium-ion cells. SIB research has focused on alternative electrodes that can replace graphite such as hard carbons[25, 32] or other layered materials beyond graphite such MoS_2[33, 34] or expanded graphite.[35] Whereas efforts are being made to develop and

understand sodium storage in carbons, typically mediated by defects, the non-conventional storage processes associated with such materials (*e.g.* pore filling and defect-activated storage) are still being understood.[36] Chapter two will introduce transition metal dichalcogenides as sodium ion battery electrodes and will show the first use of layered WSe_2 as a low overpotential conversion reaction electrode through electrochemical testing and ex-situ characterization.

1.3.2 Challenges for Potassium Ion Batteries

Compared to SIBs, K-based battery systems have significant appeal due to (1) the known formation of a stage I graphite intercalation compound (KC_8), (2) comparable earth abundance to sodium, and (3) a standard reduction potential 0.2 V lower than sodium, allowing for higher energy densities.[20] Also, the lower charge density of K^+ can provide increased mobility within the electrolyte and electrodes compared to Li^+.[37] The ability to use graphite, the commercial LIB anode, means that it may be possible to transfer existing battery manufacturing approaches to K-ion without significant manufacturing limitations. This is in stark contrast to other emerging battery technologies such as lithium sulfur that offer promises of high capacities and energy densities but require very different electrode processing methodologies that may limit manufacturing efforts.[38]

In this spirit, only in late 2015 have studies emerged demonstrating the electrochemical intercalation of K^+ into graphite using organic solvents.[39, 40] Whereas earlier studies had confirmed the presence of K-ion GICs formed by heat and vacuum treatment, the work of Jian *et al.* and Luo *et al.* demonstrate that electrochemical processes can be used to achieve KC_8 (stage I) potassium ion storage in graphite materials for the first time. These studies demonstrate in excess of 250 mAh/g during cycling at slow rates (< 50 mA/g).

Compared to LIBs and SIBs, very little is known about the electrochemical storage mechanism of PIBs. The only previous insight into the mechanism comes from *ex-situ* x-ray diffraction (XRD) and density functional theory (DFT) calculations. *Ex-situ* XRD at different states of charge revealed peaks

attributed to the structural signature of stages III, II, and I that correspond to KC_{36}, KC_{24}, and KC_8.[39] However, no studies have been performed that elucidate the real-time electrochemical pathways for K-ion insertion into graphitic carbons or to understand the staging characteristics in comparison to Li-ion or Na-ion batteries. Besides for better understanding of K^+ storage in graphite, the capacity and rate capability are still lower than Li^+ in graphite and need to be improved.

Chapter four will show the first in-situ characterization for the electrochemical intercalation of K^+ into graphite, providing fundamental understanding of the staging process. The staging of K^+ is compared to Li^+. Chapter five will then build upon that knowledge to improve the capacity and rate capability of the graphite anode by engineering the graphite electrode with nitrogen defects. Performance on par with LIBs is achieved. The role of these defects is explored with in-situ Raman spectroscopy.

1.4 Introduction to Water Desalination

Another major social issue I have been able to apply battery technology to is water scarcity. Water scarcity is a serious problem facing the world with over one third of the world's population currently living in water-stressed countries, with an expected increase to nearly two thirds by 2025.[41] Cities like Cape Town are perpetually staving off the arrival of Day Zero when the water taps will be completely emptied despite the cities location near the huge reservoir of water in the ocean.[42] Current technologies such as reverse osmosis (RO) have been deployed to process salt water into drinking water consuming three to four Wh/L, but the cost of these systems increases dramatically for small-scale distributed systems.[43, 44] The advantages of delocalized water infrastructure are similar to a distributed electrical grid such as mitigation of large scale disruptions and lower susceptibility to attacks that can disrupt the critical water supply. Electrochemical desalination techniques such as capacitive deionization (CDI) have the potential to provide a more cost and energy effective distributed desalination system.[45, 46] Although CDI can operate at high rates, it is typically used with lower concentration brine solutions instead of high concentration feeds like seawater due to the limited number of ions that can be stored in the double layer of carbons.[47]

1.5 A Desalination Battery

A new electrochemical desalination method, coined "a desalination battery" was first proposed by Pasta et al. using $Na_{2-x}Mn_5O_{10}$ nanorods and Ag microparticles as a Na^+ intercalation electrode and Cl^- removal electrode respectively.[48] A desalination battery operates by removing ions from the electrolyte through Faradaic reactions, storing energy during the charge cycle while releasing the ions into a waste brine solution and simultaneously releasing energy during discharge (Figure 1.8). A desalination battery can enable a distributed desalination system for processing seawater with higher total dissolved solids because Faradaic electrodes can store more ions compared to the double layers storage on high surface area carbons in CDI. Although a desalination battery will likely encounter solution resistance issues as the total dissolved solids are significantly lowered during charging, this system could be used as a low energy first stage in series with other desalination techniques that require significantly less energy to process lower concentration feeds.

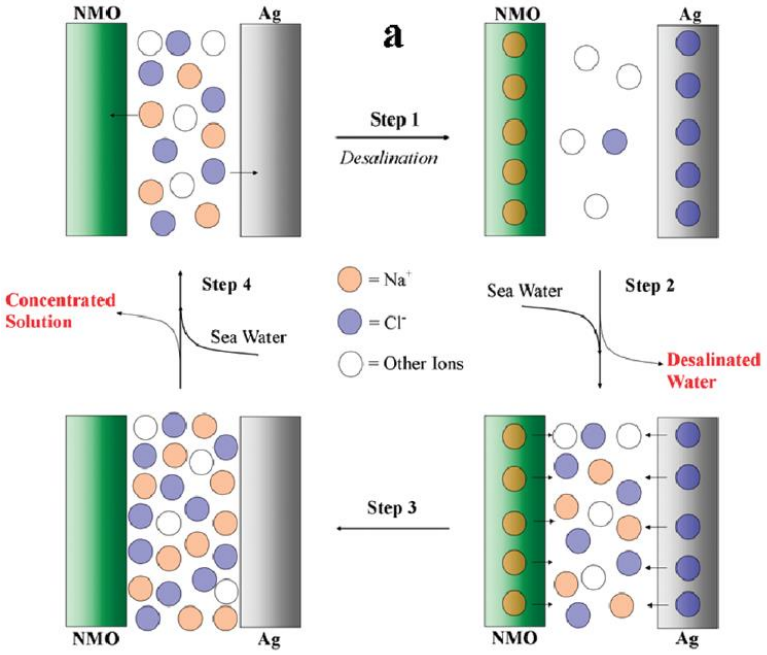

Figure 1.8 Operation of a desalination battery. Reproduced from ref. [48] with permission from ACS

Aqueous sodium ion battery research has been directly applied to desalination battery research with papers exploring Na^+ electrodes such as $NaTi_2(PO_4)_3$,[49] $Na_{0.7}MnO_2$,[50] and Prussian Blue analogues.[51-54] Suss and Presser recently published a short review of Faradaic water desalination, highlighting the use of alternative ion battery knowledge for cation desalination but also pointing out the lack of research on chloride removal electrodes.[47] Development and understanding of Cl^- electrodes is of equal importance to Na^+ electrodes but little work has focused on optimizing these materials for a desalination battery since most desalination papers have focused on Na^+ intercalation and there is only a limited selection chloride ion battery papers.[55, 56] Silver has been the chloride capturing electrode used in almost every desalination battery and has shown stable performance for 200 cycles while also reducing the voltage gap between the charge and discharge curves, leading to a lower desalination energy.[49, 57, 58]

Whereas researchers have used nanoscale materials in desalination battery electrodes, there remains little understanding regarding how controlled nanoscale dimensions can steer energetics and kinetics dictating desalination battery performance. Specifically for Ag electrodes, this is important because AgCl nucleates as a new phase at the surface of the Ag particle, leading to size dependent diffusion processes and nucleation energetics.[59-61] Chapter three will discuss my work using size-controlled Ag NP electrodes to modulate energy consumption and kinetics enabling a desalination battery with 40% reduced energy consumption.

1.6 Description of Electrochemical Tests

The electrochemists first tool when probing electrochemical reactions is cyclic voltammetry (CV). In a CV the voltage is increased or decreased at a constant scan rate while the current is measured (Figure 1.9a, b).[62] The current changes to satisfy the Nernst equation as the concentration of the oxidized or reduced species changes as a result of an electrochemical reaction.[63] For a typical diffusion limited CV the current will decay proportional to $time^{-1/2}$. An increase current during a positive sweep of the voltage corresponds to an oxidation reaction while a decrease in current during the negative sweep is the result of a reduction

reaction. While a CV can provide information related to the kinetics of electrochemical reactions and diffusion coefficients of electroactive species, it is not the best test for quantitative assessment of an electrode's ability to store ions.

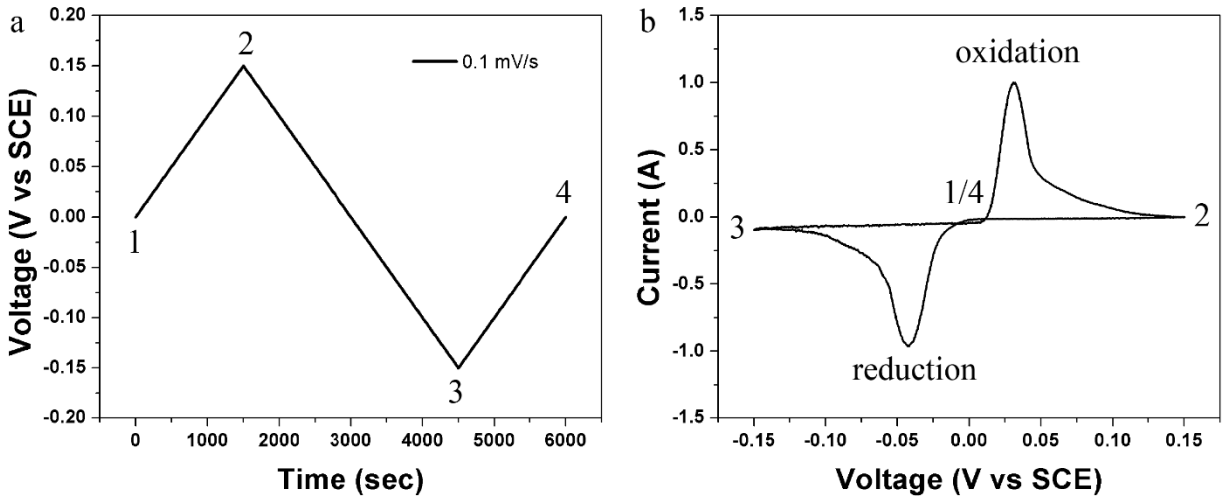

Figure 1.9a) During a CV the voltage is constantly increased or decreased at a certain rate. b) The measured current output during a CV where the peaks correspond to electrochemical reactions

The other main electrochemical test for batteries is a galvanostatic (constant current) charge-discharge (Figure 1.10). In this test, a plateau in a charge-discharge curves corresponds to an electrochemical reaction. A longer the plateau means more ions are being stored. The number of ions stored is quantified as the capacity. The charge or discharge time is easily converted into capacity in mAh/g by multiplying by the charging rate.

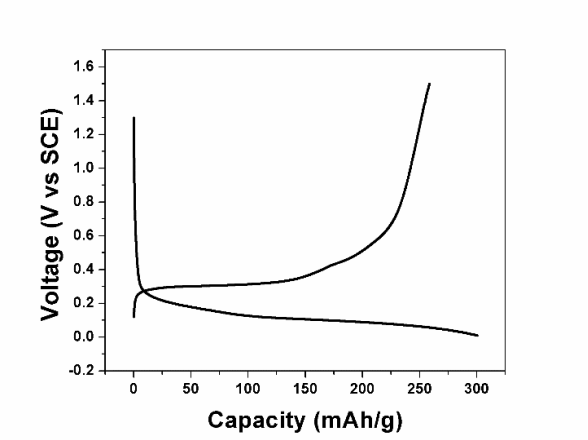

Figure 1.10 An example of a galvanostatic charge-discharge curve where the plateaus correspond to electrochemical reactions

Chapter 2 Tungsten Diselenide (WSe_2) as a High Capacity, Low Overpotential Conversion Electrode for Sodium Ion Batteries

2.1 Introduction

The transition metal dichalcogenides (TMDs) are a family of materials that have recently gained significant attention for their ability to store metal ions such as Li, Na, and Mg.[64-66] TMDs (MX_2 where M=Mo, W and X=S, Se, Te) have a lamellar structure (space group $P6_3/mmc$) similar to graphite but with larger interlayer spacing more appropriate for Na^+ intercalation. Of all TMDs, MoS_2 has been the most widely studied for sodium ion batteries,[67, 68] where storage has been identified to occur through both a high voltage intercalation reaction (products: Na_xMoS_2 ($x<0.5$)) and a low voltage conversion reaction (products: Na_2S + Mo),[65] the former of which is highly reversible.[69] The intercalation reaction shows a 2H (semiconductor) to 1T (metallic) transition while the conversion reaction produces amorphous Mo and a sodium/sulfide species.[70]

Research in TMD-based electrodes for SIBs outside of MoS_2 is limited despite research in other energy-related applications correlating TMD composition to catalytic or chemical performance,[70] due to physical reactivity tuned by the metal to chalcogen composition.[71] For SIBs, $MoSe_2$ yolk shell microspheres and $MoSe_2$ nanoplates have shown high capacities and good cyclability,[72, 73] and WS_2 crystals distributed on graphene sheets have indicated high rate capabilities.[74] However, no studies have been performed to date to assess the ability for WSe_2 to store sodium ions.

In this study, we investigate WSe_2 as a conversion electrode for SIBs for the first time. Bulk WSe_2 is used instead of synthesized nanostructures in order to assess the material properties as opposed to structural effects (SEM of WSe_2 Figure 2.1). Whereas TMDs containing heavier elements such as W or Se may not intuitively be expected to exhibit high specific capacities, our work demonstrates superior energetics of WSe_2 compared to WS_2, and comparable or better specific capacity in comparison to other

TMDs containing lighter elements. We highlight the chemical nature of the conversion reaction, speculating on similarities and differences between WSe_2 and heavily studied MoS_2 materials that give promise to WSe_2 as a candidate material for next-generation SIB platforms.

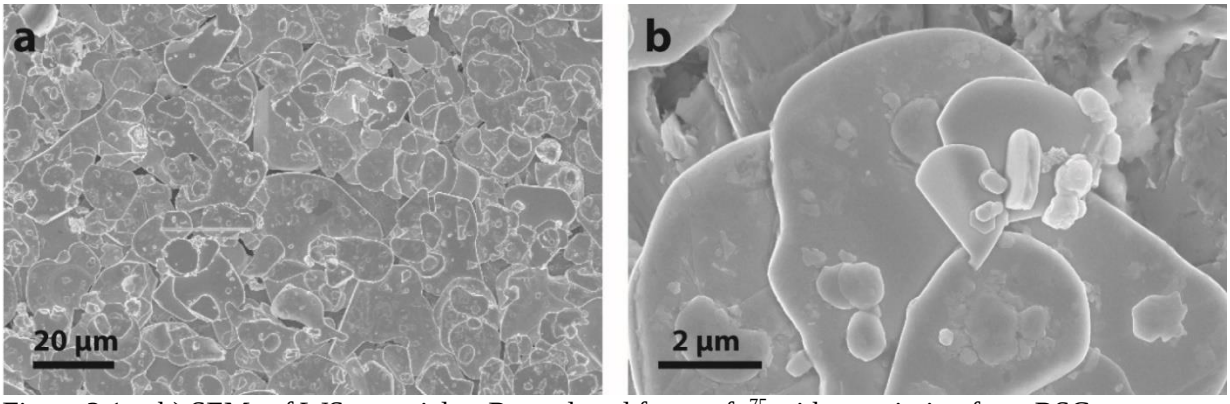

Figure 2.1 a, b) SEMs of WSe_2 particles. Reproduced from ref. [75] with permission from RSC

2.2 Experimental Methods

Commercial TMD powders (WS_2, 99%, two µm, and WSe_2, 99.8%, 20 µm) were acquired from Sigma Aldrich and Alfa Aesar. Working electrodes were prepared by combining the TMD (60 wt.%), super P carbon (20 wt.%) and either PVDF (Alfa Aesar) or CMC (Sigma Aldrich, MW=90,000) binder (20 wt.%) in NMP for PVDF or water for CMC, sonicating for ten minutes, and then drying the slurry on a stainless-steel disk for at least twelve hours at 55°C. Half cell batteries were assembled in an Ar filled glove box using a coin cell with a Na metal (Sigma Aldrich, 99.95%) electrode, 1M $NaPF_6$ (Strem, 99%) in anhydrous PC (Sigma Aldrich, >99.7%), anhydrous EC/DEC in a four: six ratio (Sigma Aldrich, 99%, >99%), or anhydrous diglyme (Sigma Aldrich, 99.5%) as the electrolyte, and a Whatman grade GF/F glass fiber microfiber filter separator (Sigma Aldrich). Cyclic voltammetry (CV) was performed on a Metrohm Autolab multichannel electrochemical workstation. Galvanostatic rate and cycling studies from 0.1 V to 2.5 V were performed on an MTI eight channel battery analyzer. Immediately prior to

all electrochemical tests, the batteries were allowed to reach open circuit voltage over three hours. All electrochemical measurements are normalized to the mass of the TMD. Raman measurements were performed using a Renishaw inVia Raman spectrometer with a 785 nm laser. X-ray diffraction was performed using a Scintag XGEN 4000 system with a CuKα (λ=0.154 nm) radiation source. A FEI Tecnai Osiris TEM with EDX capability was used for elemental analysis. To prepare ex-situ samples, coin cells were disassembled in an Ar filled glovebox and the working electrode was removed and either washed in PC or untreated and then dried under vacuum for 24 hours. Raman measurements were carried out in a homemade air tight system.

2.3 Electrochemical Results

Previous studies have indicated that PVDF with carbonate electrolytes can compromise the integrity of the electrode through unwanted side reactions.[76, 77] Recently, Wang *et al* studied the effect of binders on microscale MoS_2 in EC/DEC and found that CMC had the highest capacity and also degraded much less than PVDF.[78] In this manner, our first efforts aim to identify WSe_2 electrode, binder, and electrolyte combinations that yield the best battery performance (Figure 2.2). Figure 2.2a-c and d-f show differential capacity plots and cycling data for each electrolyte combined with PVDF and with CMC respectively (charge-discharge profiles Figure 2.3).

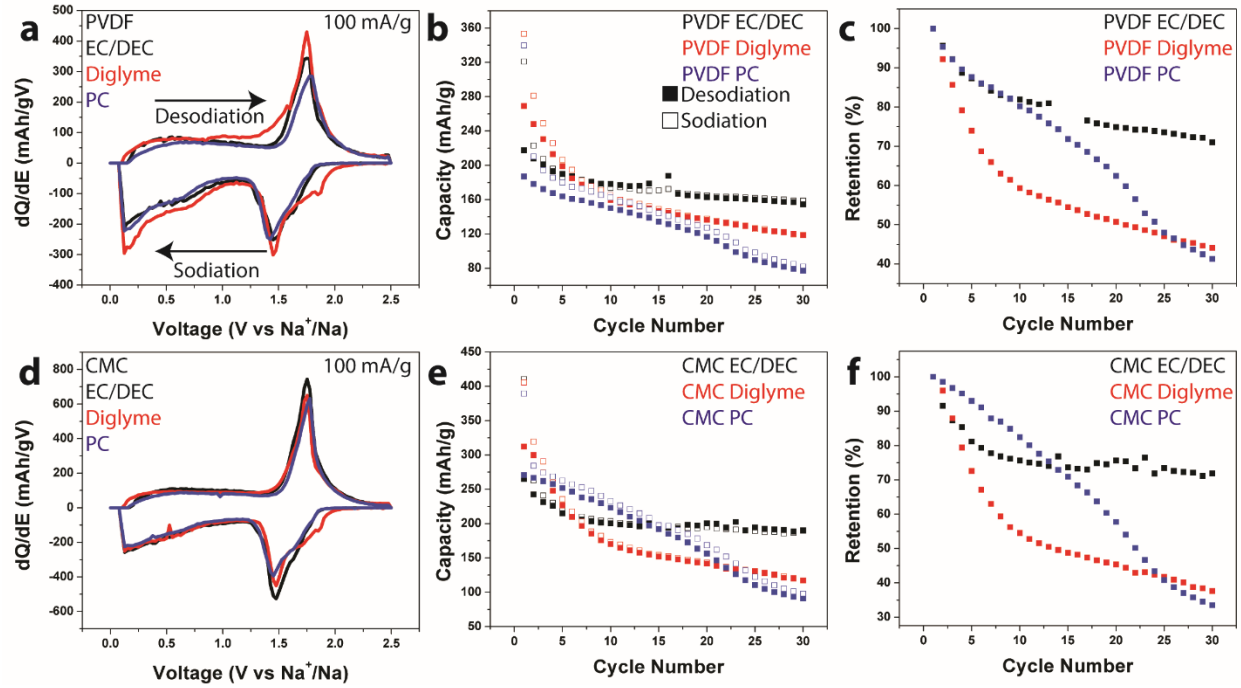

Figure 2.2 a) dQ/dE for PVDF binder with 1M $NaPF_6$ in EC/DEC, diglyme, and PC b) Cycling capacity at 100 mA/g for PVDF with all three electrolytes c) Capacity retention based on PVDF samples at 100 mA/g d) dQ/dE for CMC binder with 1M $NaPF_6$ in EC/DEC, diglyme, and PC e) Cycling capacity at 100 mA/g for CMC with all three electrolytes f) Capacity retention based on CMC samples at 100 mA/g

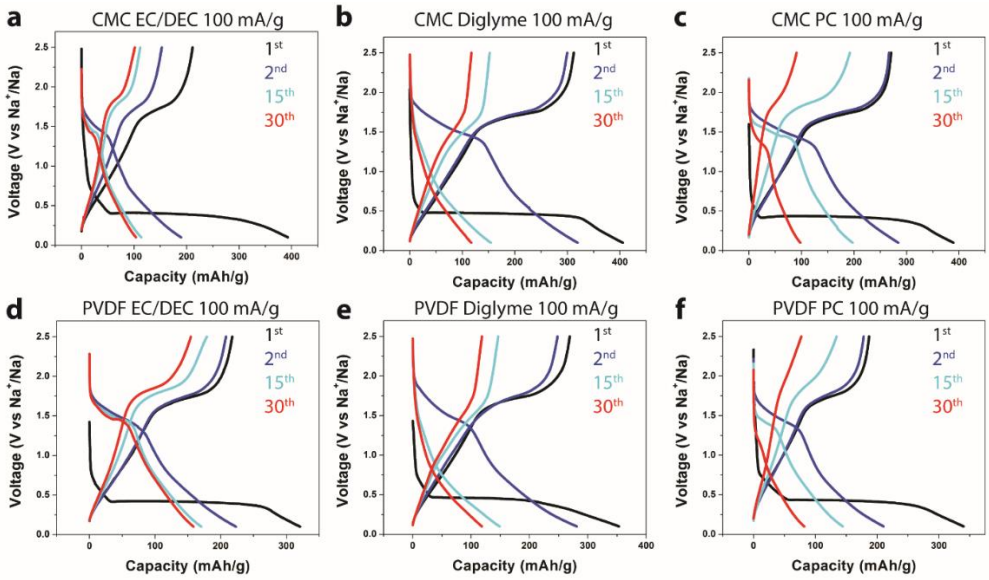

Figure 2.3 Charge-discharge curves for the first, second, fifteenth, and thirtieth cycle for each electrolyte/binder combination. The electrolyte/binder combinations have no effect on the energetics of the reaction, only the performance. CMC with a) EC/DEC b) diglyme c) PC. PVDF with d) EC/DEC, e) diglyme, f) PC

Differential capacity data are obtained by differentiation of galvanostatic charge-discharge profiles. These provide the same information as the charge-discharge profiles but more obviously highlights the energetics of the reaction. In each case, the sodiation and desodiation reactions remain invariant across the different electrolytes, even in the case of diglyme where solvent co-intercalation reactions can occur that drastically change the energetics.[79] Galvanostatic charge-discharge cycling tests were carried out for thirty cycles at 100 mA/g (Figure 2.2 b,e), which distinguish the stability of different electrolyte-binder combinations in this system. In all cases, the capacity of CMC-based electrodes is comparable to or greater than the equivalent system with PVDF. For both binders, diglyme electrolytes exhibit higher capacity for the first few cycles but the capacity quickly fades by over 50% after ~ten cycles with a final capacity of 118 mAh/g with PVDF and 117 mAh/g with CMC after thirty cycles. Propylene carbonate electrolytes combined with both CMC and PVDF binders also exhibit rapid capacity fade over thirty cycles, while EC/DEC electrolytes lead to a stable capacity through thirty cycles following the first few cycles. We attribute the adverse cycling performance of both PC and diglyme electrolytes to irreversible side reactions occurring between the electrolyte and binder. Such irreversible side reactions are also apparent for PC electrolytes through the low Coulombic efficiency between charge and discharge. EC/DEC samples have the highest capacities at the end of thirty cycles for both PVDF (155 mAh/g) and CMC (190 mAh/g), with stable cycling performance. This allows us to establish the best electrolyte-binder combination for WSe_2 electrodes, which is EC/DEC combined with CMC binders. This combination shows virtually no capacity fade over the last twenty-five cycles and exhibits the highest reversible capacity of all electrolyte-binder combinations following five cycles of consecutive cycling. Even after sixty cycles this best battery composition has a capacity around 100 mAh/g (Figure 2.4). Therefore, this binder/electrolyte combination was used for the rest of the testing.

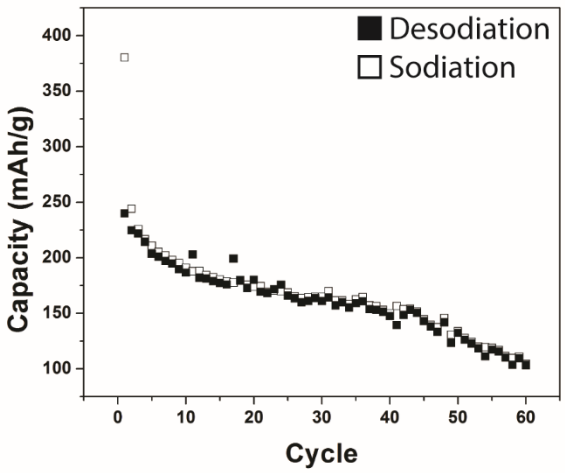

Figure 2.4 Capacity for 60 cycles at 100 mA/g of WSe2 with CMC in EC/DEC. The capacity after 60 cycles is around 100 mAh/g.

Cyclic voltammetry (CV) curves for WSe_2 taken at a scan rate of 0.5 mV/s are shown in Figure 2.5a for the first, second, and third cycles with sodiation and desodiation processes labeled. The first sodiation involves a reaction peak at low voltages (< 0.25 V vs. Na/Na^+) without any signature of higher voltage chemical processes. The second cycle also shows this low voltage signature combined with two higher voltage reaction peaks between 1.2 and 1.85 V vs. Na/Na+. In the third cycle, the low voltage peak is absent, and only a series of two peaks between 1.2 and 1.85 V are observed.

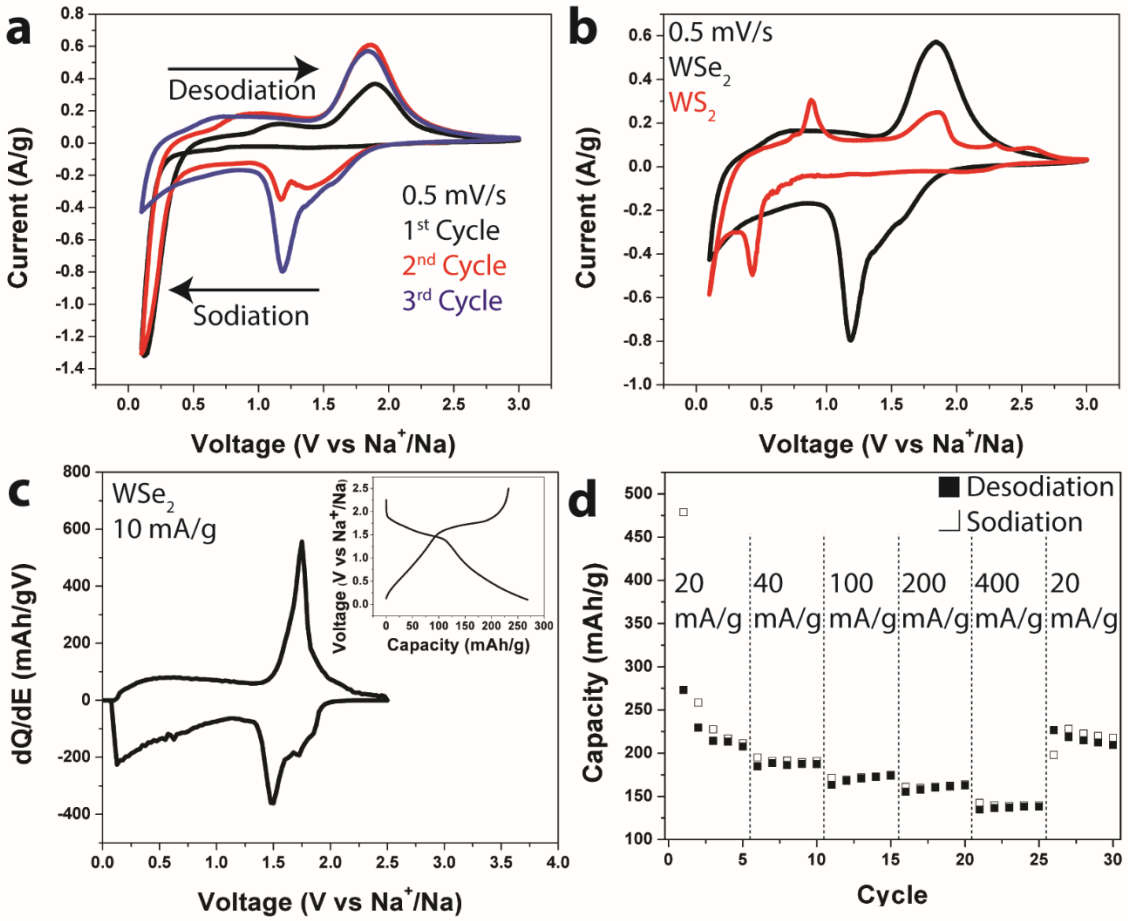

Figure 2.5 a) CV scans for the first three cycles from WSe_2 devices with CMC and EC/DEC b) CV scans comparing the energetics of chemical storage in WSe_2 and WS_2 during the third cycle c) dQ/dE of a WSe_2 electrode at 10 mA/g, inset) charge discharge curves at 10 mA/g d) Galvanostatic rate study at 20, 40, 100, 200, and 400 mA/g

Based on this result, we infer that this low voltage (<0.25V vs Na/Na^+) signature is evidence of Na^+ intercalation into WSe_2, which upon sodiation goes through a reversible conversion reaction. After the second CV cycle, the absence of this low voltage peak indicates a fully converted WSe_2 electrode material. The conversion reaction proposed for TMDs, which we later confirm with STEM EDS mapping, produces a Na/chalcogenide conversion product. In the case of WSe_2, the reaction would be

$$WSe_2 + 2x\ Na^+ + 2x\ e^- \leftrightarrow 2\ Na_xSe + W \quad (1)$$

The second and third cycles display a cathodic peak at 1.25 V and anodic peak at 1.85 V that correspond to a coupled reaction centered near 1.6 V vs. Na/Na^+. At scan rates of 0.5 mV/s, the energetics of this redox process are far better than that observed during chemical conversion of WS_2 (Figure 2.5b). Tungsten disulfide displays an anodic peak also near 1.8 V but a cathodic peak centered near 0.4 V, yielding a much higher overpotential that would bottleneck the energy efficiency of a full cell device. The chemical conversion reaction is further isolated through galvanostatic measurements, where charge and discharge profiles are differentiated with respect to voltage to yield plots of dQ/dE (Figure 2.5c). The charge-discharge curves for the dQ/dE can be found in the inset. Analogous to CV curves, a low overpotential (0.26V) conversion reaction is isolated at currents of ten mA/g. Low overpotentials are critical to the operation of an electrode in a full cell configuration where energy efficiency is a benchmark for performance, and our work distinguishes the low overpotential for the WSe_2 conversion reaction from both WS_2 as well as other studied TMDs such as MoS_2 which has an overpotential of 1.3 V for the intercalation reaction and 0.4 V for the conversion reaction.[65]

In addition to the cyclability and energetics another important characteristic of an electrode material is the rate capability (Figure 2.5d). Tungsten diselenide was tested at 20, 40, 100, 200, and 400 mA/g (Figure 2.6). Capacities of WSe_2, which range from over 200 mAh/g at the lowest rate to near 135 mAh/g at the highest rates, are higher than the best results reported for bulk MoS_2, the most studied TMD in SIBs.[34, 65] This is notable since both W and Se are heavier elements than Mo and S, which implies WSe_2 to have superior volumetric storage capacity compared to MoS_2 – an important concept for many emerging energy storage applications. Tungsten diselenide displays a large average extraction capacity of 228 mAh/g at 20 mA/g and maintains over 60% capacity (130 mAh/g) at a 20x faster charging rate of 400 mA/g. The average capacity of the final five cycles at 20 mA/g show only two percent degradation compared to the average capacity of the initial five cycles.

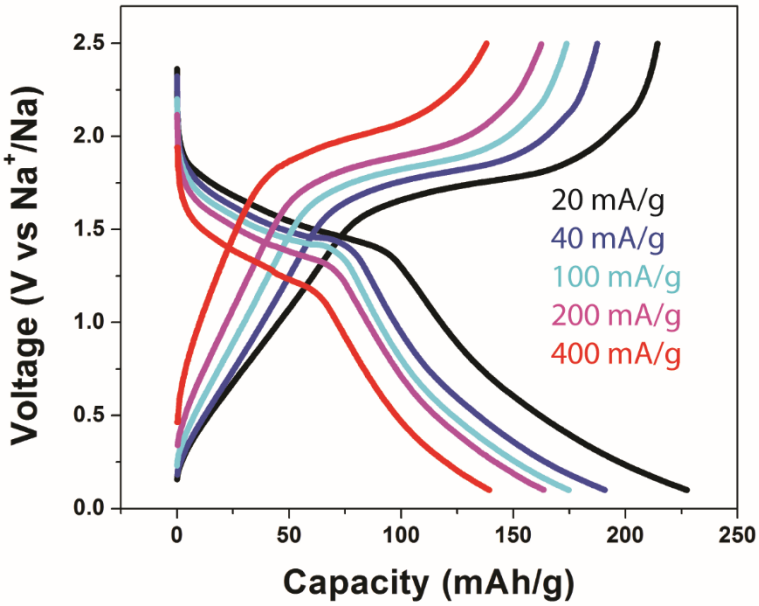

Figure 2.6 Charge-discharge curves of WSe_2 with CMC in EC/DEC at different charging rates. The overpotential increases at faster charging rates due to resistive effects.

2.4 Characterization of the Mechanism through Ex-Situ Techniques

Whereas the premise of this work thus far is that WSe_2 exhibits a conversion reaction in a manner consistent with that observed in MoS_2 materials, *ex-situ* analysis of sodiated WSe_2 materials was performed to assess the signature of the conversion products. A combination of electron dispersive x-ray (EDS) analysis in the transmission electron microscope (TEM), XRD, and Raman spectroscopy was utilized to analyze products following the fifth discharge for EDS, fifth discharge and fifth charge for XRD, and the first discharge for Raman. The fifth cycle was chosen to characterize for EDS and XRD to ensure full conversion of the WSe_2. Analysis of the fifth discharge products with XRD indicates the presence of numerous crystalline products that are not associated with the initial WSe_2/PVDF/carbon black electrode (Figure 2.7a). The low angle peaks at 11.8° and 17.0° corresponding to an interlayer spacing of 7.48 Å and 5.21 Å are likely attributed to a hexagonal Na_xSe material that forms upon

sodiation. The improved crystallinity of WSe_2 conversion products compared to MoS_2 conversion products could lead to lower resistance within the electrode. Additional peaks at 27.9° and 32.4° are consistent with Na_2O (JCPDS card no. 03-1074), likely formed due to the air exposure during the measurement. No peaks related to W metal are observed, indicating that W products may form amorphous or poorly crystalline domains.[70] X-ray diffraction after the fifth charge cycle reveals a change in the low angle peak compared to the previous sodiated state (Figure 2.7b). The peaks at 11.8° and 17.0° are no longer present but the main WSe_2 (002) peak at 13.6° is apparent. The intensity of the WSe_2 peak is lower than the initial state due to a loss in crystallinity but it is obvious that WSe_2 is reformed after sodium extraction.

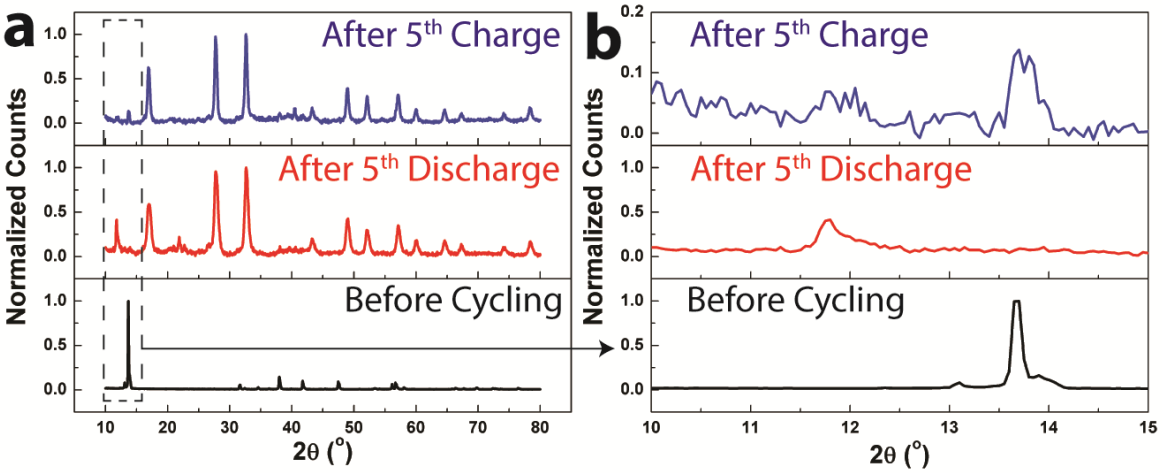

Figure 2.7 a) XRD pattern of the initial WSe_2, the Na_xSe product formed after the fifth discharge, and the less crystalline WSe_2 formed after the fifth charge b) The same spectrum in Fig 3a but zoomed into only the lower angle peaks

E*x-situ* Raman spectroscopy (Figure 2.8) supports the formation of a new crystalline product upon sodiation. The initial spectrum has two main peaks at 251 and 254 cm^{-1} corresponding to the E_{2G} and A_{1G} WSe_2 peaks (inset Figure 2.8).[80] After the first discharge, the WSe_2 peaks are no longer present and new peaks arise at 247 cm^{-1}, 329 cm^{-1}, 816 cm^{-1}, and 930 cm^{-1}. We attribute these to Na_xSe

conversion products formed during sodiation, even though these peaks are not due to cubic Na_2Se (165 cm^{-1}, 225 cm^{-1})[81] or Se (235 cm^{-1}).[82]

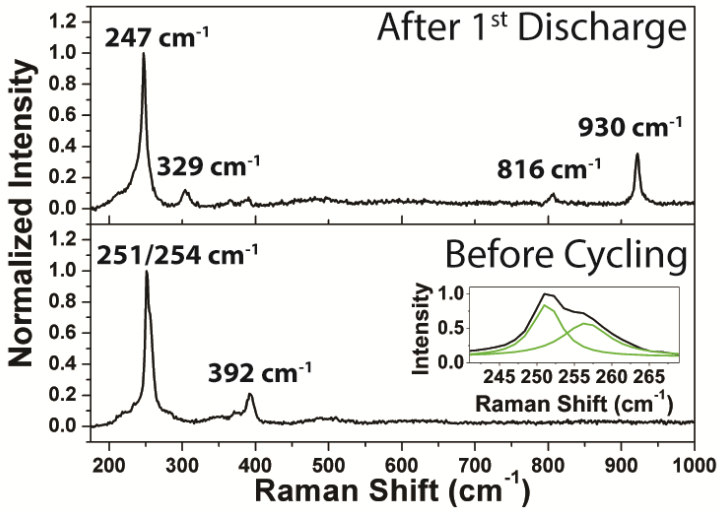

Figure 2.8 Raman spectra of the initial electrode and the electrode after the first discharge. The inset shows the two-peak fit of the WSe_2 Raman modes

Analysis of EDS data from TEM analysis (Figure 2.9a-c) indicates a picture consistent with reports on conversion products in MoS_2 materials.[70] Composite EDS maps of the material before conversion shows a homogenous mix of W and selenide species throughout the sample. EDS maps after the fifth discharge elucidates the formation of isolated W domains adjacent to regions that contain selenides (Figure 2.9b). The Na species is located in the same spatial region as the selenides, supporting the formation of Na_xSe (Figure 2.9c). The separation of the domains is likely due to W diffusion through the lattice.[83] This supports the storage of Na through the conversion reaction discussed in eqn. (1), where domains of Na_xSe and W reversibly interchange between sodiated (W + Na_xSe) and mostly desodiated (Na_xWSe_2) states. Since the capacities we measure are comparable to MoS_2 despite the heavy nature of both W and Se compared to Mo and S, we speculate that the improved conductivity of metal selenides

compared to metal sulfides could play a role to improve the electrical connectivity of sodium-storage converted products in bulk matrices of TMD materials.[84]

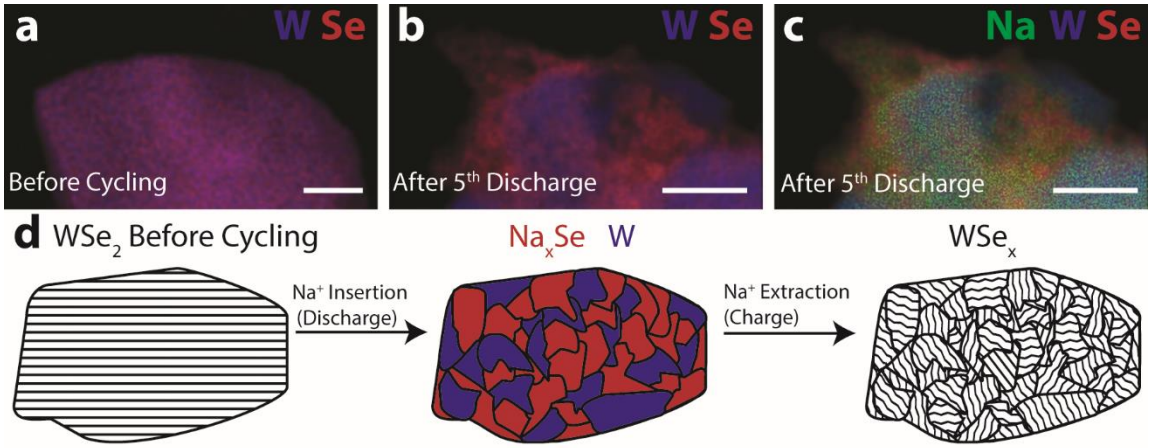

Figure 2.9 a) EDS composite map of a WSe_2 electrode before cycling, scale bar = 100 nm b) EDS composite map of a WSe_2 battery electrode after the fifth discharge showing W and Se, scale bar = 100 nm c) The same EDS spectrum as Fig 5b but with the Na added d) Schematic illustrating the storage mechanism of Na in WSe_2. Upon Na^+ insertion segregated domains of Na_xSe and W form. After the Na^+ has been removed, WSe_2 is reformed but it is less crystalline than in its original state.

Therefore, based on both electrochemical data and the direct assessment of sodiated products through EDS in the TEM, Raman spectroscopy, and XRD, we propose a mechanism of eqn. (1) where crystalline WSe_2 is converted into sodiated products of Na_xSe and poorly crystalline or amorphous W metal. Upon removing the sodium, WSe_2 is reformed but is less crystalline than the original sample. This mechanism is illustrated in Figure 2.9d. This general conversion reaction is consistent with previous studies for MoS_2 materials, even though WSe_2 exhibits an efficient conversion reaction characterized by a crystalline product, low overpotential, good cyclability even in bulk, and improved specific capacity despite the use of a compound with heavier elements. This distinguishes WSe_2 as a strong candidate for high efficiency sodium ion battery electrodes mediated by a sodium-selenium conversion reaction yielding comparable specific capacity and better volumetric capacity compared to widely studied MoS_2 materials.

2.5 Conclusion

In closing, WSe_2 is demonstrated as an efficient electrode material for a sodium ion battery for the first time. Six different binder/electrolyte combinations have been studied and CMC binder with a $NaPF_6$ in EC/DEC electrolyte has been shown to have the highest capacity (190 mAh/g) and best capacity retention (72 %) after 30 cycles with virtually negligible capacity change over the last 25 cycles. Directly comparing the energetics of WSe_2 to WS_2 electrodes, we observe a significantly reduced overpotential of 0.26 V, making the energetics of this conversion reaction practical for high energy efficiency devices. WSe_2 electrodes exhibit over 200 mAh/g reversible specific capacity at 20 mA/g rates and maintain 60% capacity at 400 mA/g. Based on performance alone, this material exhibits storage capability comparable to previous reports on MoS_2, despite the heavier W and Se elemental components – hence improved volumetric capability. Ex-situ analysis including EDS in the TEM, XRD, and Raman spectroscopy indicate the conversion mechanism as the formation of poorly crystalline or amorphous W domains alongside Na_xSe products, which we speculate is enhanced for WSe_2 due to the more conductive nature of Se-based conversion products compared to S-based products. This work highlights WSe_2 as a highly promising and practical electrode material for SIB applications, with a multitude of routes such as nano/microstructuring,[85] surface modification through ALD passivation,[86, 87] or forming graphene-WSe_2 composites,[88-90] to allow for further improving and optimizing the already promising performance for broad impact of this TMD in next-generation battery technology.

Chapter 3 Tuning Silver Nanoparticle Size to Reduce Energy Consumption of a Desalination Battery

3.1 Introduction

Another exciting application of SIB technology has been desalination in aqueous systems using Na^+ intercalation compounds. The vast majority of Faradaic desalination research has focused on Na^+ electrodes, with far fewer papers taking a critical look at the Cl^- electrode. Silver has been the electrode of choice for the anode in virtually every paper. Nam and Choi have proposed the only other Faradaic chloride removal electrode consisting of Bi/BiOCl showing stable capacity over 200 cycles but these electrodes require a large overpotential (~1V) leading to a high desalination energy, while also needing an acidic environment during discharge.[91] Further research of aqueous chloride capturing electrodes could be very promising. System level designs using anion exchange membranes have bypassed the need for a chloride removal electrode but they rely on heavily engineered and potentially expensive membranes.[92, 93]

The major limitation in desalination systems is the desalination energy. In desalination batteries, the energy is partially limited by the formation of AgCl, an electronically and ionically resistive material. Most papers have used either Ag foils or Ag microparticles in excess to mitigate this issue. There has not been a critical look at the mitigation of resistive effects upon de-chlorination of water. The increased ionic and electronic resistance upon AgCl formation can be mitigated by the use of smaller nanoparticles where the size of the AgCl layer formed is inherently limited by the size of the Ag nanoparticles (NPs). In this work, I study how size-controlled Ag NP electrodes can modulate energy consumption and kinetics to enable a desalination battery more energy efficient during operation than RO. My results show that 25 nm Ag particles require 30-40% less energy than 326 nm particles with desalination energies as low at 0.09 Wh/L. Overall, the findings emphasize how nanoscale engineering can be a powerful tool in fine tuning the energetics for Faradaic reactions.

3.2 Experimental Details

3.2.1 Synthesis of Ag Nanoparticles

The synthesis of Ag NPs was similar to the procedure described by Kim et al. but the reaction times and quenching methods were varied to achieve different particle sizes.[94] To summarize, a 50 mL round bottom flask with a stir bar was immersed into a Silicone oil bath on a hot plate. Ten mL of ethylene glycol (ReagentPlus, >99%, Sigma Aldrich) was added to a round bottom flask. 0.030 g of polyvinyl pyrrolidone (MW=10k, Sigma Aldrich) was added and vigorously stirred until dissolved, approximately ten minutes. The stirring rate was reduced to 700 RPMs. 0.424 g of $AgNO_3$ (ACS, Sigma Aldrich) was then added to the round bottom flask. The temperature of the hot plate was controlled to maintain a heating rate of ~six °C/min. 25 nm particles were synthesized by quenching the reaction with DI H_2O when the solution turned grey/green, typically around 117°C. 62 nm particles were made by quenching the reaction with DI H_2O when the temperature reached 120°C. 326 nm particles were synthesized by stopping the reaction five minutes after the temperature reached 120°C, followed by cooling in air. After cooling, the particles were centrifuged three times, removing the supernatant and washing with DI H_2O after each cycle. 25 nm particles were centrifuged for ten minutes at 10,000 RPMs while the other particles were centrifuged at 6000 RPMs for ten minutes. The final concentrated solution of Ag NPs was pipeted onto a glass slide and dried overnight on a hot plate at 50°C.

3.2.2 Preparation of the Electrode

Ag NPs were annealed in a reducing environment of H_2 (100 sccm) in a homemade chemical vapor deposition reactor. The temperature and time varied depending on the particle size. 25 nm particles were annealed at 150°C for five minutes while the 62 nm and 326 nm particles were annealed and 250°C for one hour. Ag NPs, carbon black, and polyvinylidene difluoride (PVDF) were combined in a glass vial in a mass ratio of eight:one:one. NMP was added and mixed for one hour on a stir plate followed by bath sonication

for thirty minutes. The electrode slurry was painted onto carbon cloth (fuelcellstore.com) and dried under vacuum overnight.

3.2.3 Characterization of Materials

SEM imaging was performed using a Zeiss MERLIN with GEMINI II SEM. XRD was performed using a Rigaku SmartLab XRD. TEM was performed using a FEI Tecnai Osiris TEM with elemental mapping capabilities.

3.2.4 Electrochemical Testing

All electrodes were pretreated with high rate (5.0 A/g for 25 nm particles and 2.5 A/g for 62 nm and 326 nm particles) galvanostatic testing between -0.15 and 0.15 V vs SCE. The pretreatment stabilized the performance and was found to be necessary to activate the electrodes and achieve a high salt removal capacity. The fast pretreatment is thought to provide a large number of small AgCl nucleation sites that allow for better utilization of the Ag at slower rates, although the exact mechanism is still being studied. Cyclic voltammograms and galvanostatic pretreatment tests were performed using a Metrohm Autolab Multichannel analyzer between -0.15 and 0.15 V vs SCE. Galvanostatic testing was limited to removing 53 mg Cl^-/g Ag (581 sec at 0.25 A/g and 58.1 sec at 2.5 A/g) in an intermediate range where the particles never become fully chlorination or dechlorinated to minimize large changes in voltage arising from nucleation overpotential and as the reaction reaches completion. This testing method enables a clearer assessment of energy efficiency. All samples were tested in a three-electrode electrochemical cell using Pt foil as a counter electrode and SCE as the reference electrode. 0.6 M NaCl was used as the electrolyte.

3.3 Characterization of Silver Nanoparticles

Ag NPs with average diameters of 25 nm (n = 227), 62 nm (n = 136), and 326 nm (n = 55) were synthesized by varying the reaction time and cooling method in a polyol synthesis based on a recipe developed by Kim et al (insets Figure 3.1a-c).[94] The 326 nm particles have a bimodal distribution with

average diameters around 220 and 400 nm as a result of continuing Ostwald ripening as the reaction time increases. The different particles sizes are shown in SEMs in Figure 3.1a-c.

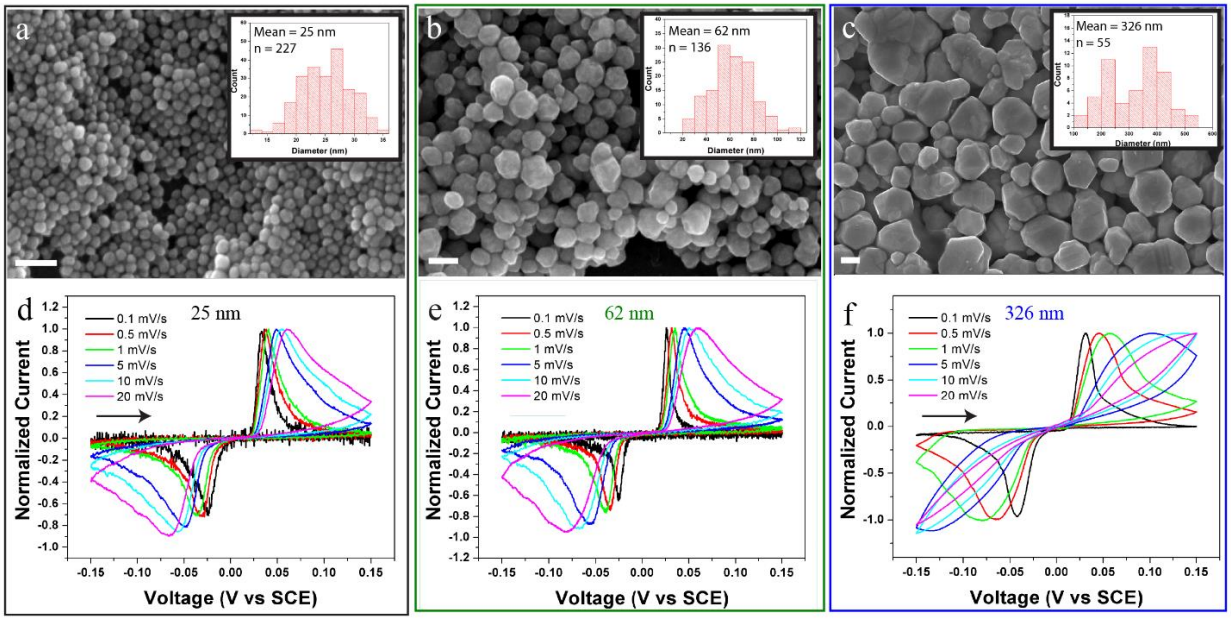

Figure 3.1 (a-c) Scanning electron microscope images of the Ag nanoparticles grown in the three syntheses with particle size distributions, n = sample size (insets) Scale bars = 100 nm. (d-f) Cyclic voltammogram from -0.15 to 0.15 V vs SCE at 0.1, 0.5, 1, 5, 10, and 20 mV/s for each of the corresponding Ag nanoparticle sizes.

X-ray diffraction (XRD) of the nanoparticles shows peaks at 38.1°, 44.3°, 64.5°, and 77.2° corresponding to the (111), (200), (220), and (311) peaks of silver, confirming the synthesis of Ag NPs (Figure 3.2). A transmission electron microscope (TEM) image of a nanoparticle from the 25 nm synthesis reveals a NP containing multiple grains (Figure 3.2 inset), potentially providing diffusion pathways and reactive nucleation sites for AgCl formation during desalination.

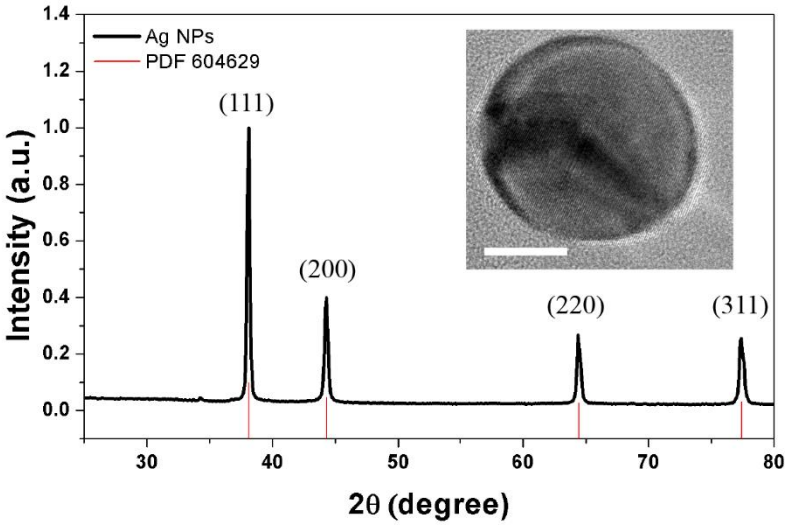

Figure 3.2 XRD pattern of Ag NPs after synthesis. The peaks correspond to Ag, PDF 604629. Inset. TEM of a NP from the 25 nm synthesis

Before electrode assembly, all Ag NPs were annealed at elevated temperatures under hydrogen to remove any oxide that may have developed on the surface.[95] Slight sintering of the NPs occurred at the elevated temperatures used, allowing the NPs to form a well-connected network while maintaining their size (Figure 3.3a-c). Since the melting point and surface energy of a metal changes with nanoparticle size, a lower temperature was used for the smallest particles to maintain their size while still producing a nanoparticle network through sintering.[96, 97] TEM image of the NPs after annealing reveal the slight rearrangement of grain boundaries within the particles (Figure 3.3d).

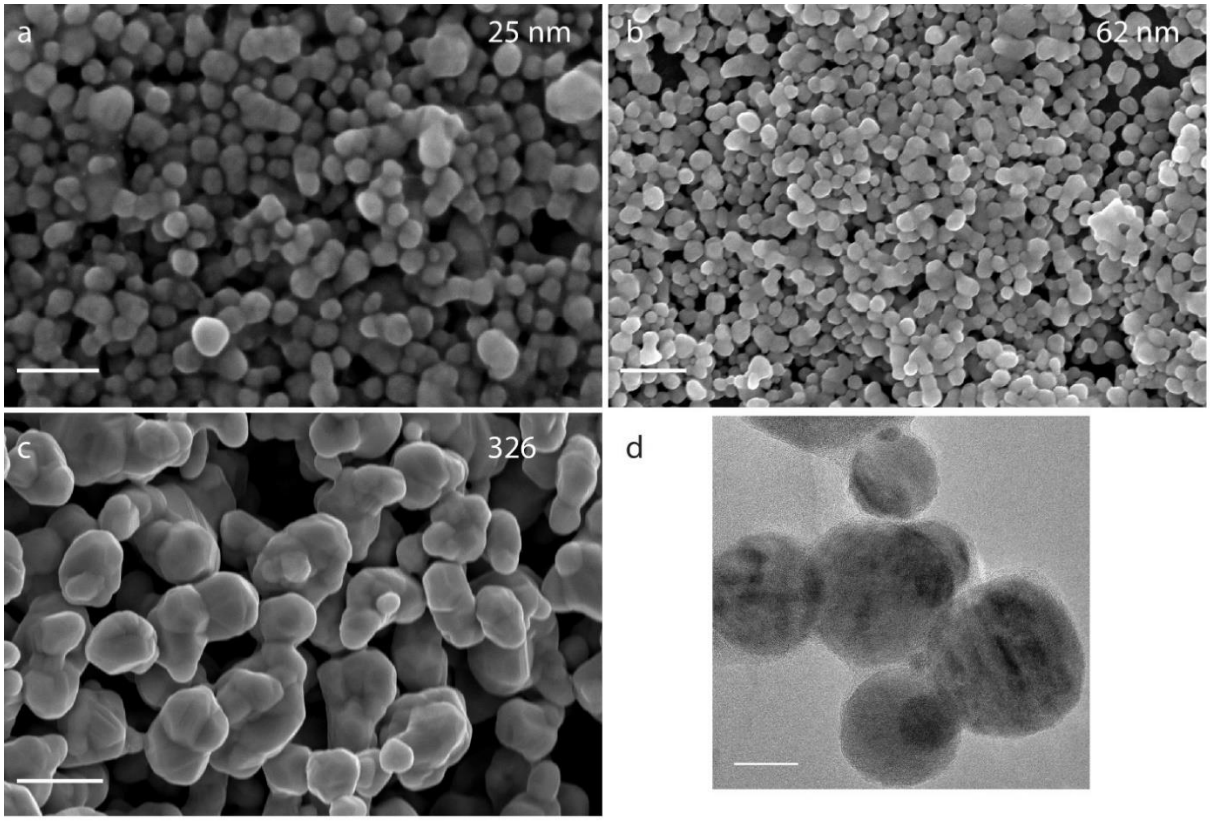

Figure 3.3 SEM images of 25 nm (a, scale bar = 100 nm), 62 nm (b, scale bar = 300 nm), and 326 nm (c, scale bar = 1 µm) Ag NPs after annealing under H2. d) TEM of 25 nm particles after annealing under H2. Scale bar = 20 nm

3.4 Cyclic Voltammetry

Electrochemical testing was used to assess changes in energetics and kinetics as a function of NP size. Cyclic voltammograms (CVs) at 0.1, 0.5, 1, 5, 10, and 20 mV/s were performed between -0.15 V and 0.15 V vs SCE for all NP sizes (Figure 3.1d-f). One oxidation and reduction peak can be seen in the CVs. XRD confirms the oxidation peak forms AgCl (Figure 3.4) through the net reaction $Ag + Cl^- \rightarrow AgCl + e^-$ while the reduction peak is the reverse reaction. The 25 nm and 62 nm CVs look similar at all rates but the shape of the curves for the larger particles drastically deviates from ideal behavior even at slower scan rates. The change from a typical duck shaped CV is indicative of a quasi-reversible reaction that can occur because of diffusion or kinetic limitations.[98, 99] Even at rates as low as 0.5 mV/s the 326 nm particles appear

to reach a quasi-reversible regime while the 25 nm and 62 nm particles remain reversible until around ten mV/s.

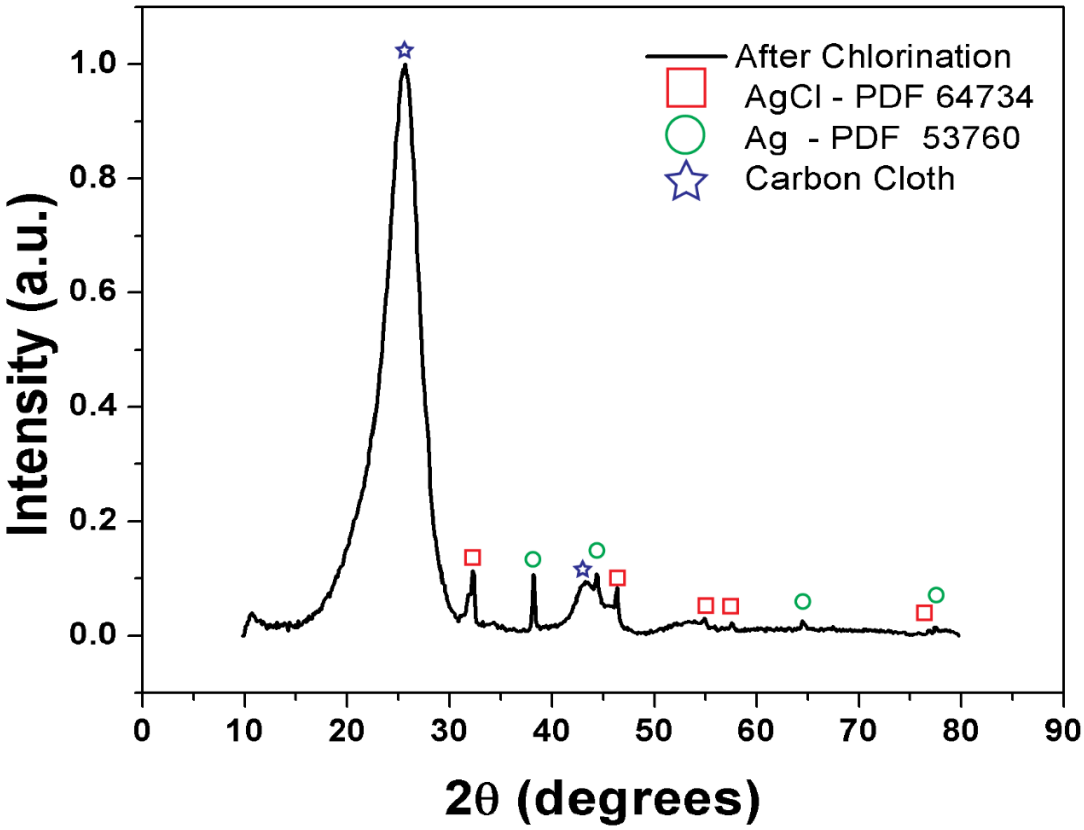

Figure 3.4 XRD after chlorination of Ag NPs. Peak correspond to both AgCl (PDF 64734), Ag (PDF 53760), and the carbon cloth current collector

Although the net reaction is $Ag + Cl^- \rightarrow AgCl + e^-$, during the oxidation process there is an electrochemical reaction ($Ag^0 \rightarrow Ag^+ + e^-$) followed by a chemical reaction ($Ag^+ + Cl^- \rightarrow AgCl$), with the opposite occurring during the reduction. Broadening of the CV peaks indicates a kinetic limitation occurring in the chemical reaction

$$Ag^+ + Cl^- \overset{k_r k_f}{\longleftrightarrow} AgCl$$

where k_f is the rate constant of the forward reaction and k_r is the rate constant of the reverse reaction. The continued reversible behavior of smaller NPs at higher rates indicates that this system is able to mitigate the diffusion and kinetic limitations occurring during the forward and reverse reactions, as discussed later. According to the Randles-Sevcik equation, an electrochemically reversible system, where the electron transfer kinetics are fast compared to mass transport, has a slope of ½ when log(peak current) is plotted vs log(scan rate).[63, 99] Figure 3.5 shows the slope for both the max current and minimum current of all particles is nearly 0.5, indicating an electrochemically reversible system.

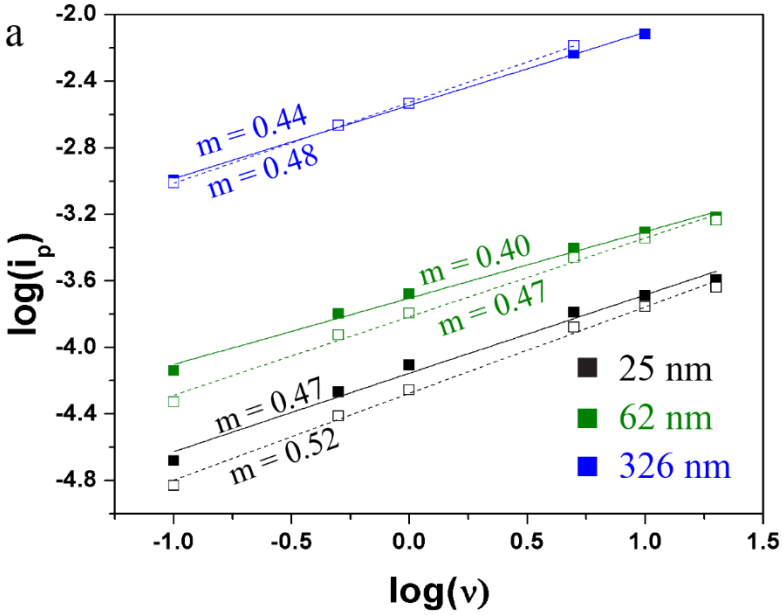

Figure 3.5 log of peak current vs log scan rate. According to the Randel-Sevcik equation, an electrochemically reversible reaction has a linear relationship between i_p and $\upsilon^{1/2}$.

$$i_p = 0.446nFAC^o\left(\frac{nF\nu D_o}{RT}\right)^{1/2}$$

Peak splitting between the oxidation and reduction peaks is proportional to the desalination energy requirements and is affected by ionic and electronic resistances. Figure 3.6a shows the clear distinctions in overpotential between the different size NPs. At 5 mV/s the overpotential of the 326 nm particles is 0.24

V while the smaller particles have an overpotential of only ~0.1 V. Faster scan rates reveal continued improvements in energetics as particle size is reduced with 25 nm particles having lower overpotential than 62 nm particles. Interestingly all particle sizes have larger increases in the reduction voltage than the oxidation voltage as the scan rate increases (Figure 3.6b). Although the oxidation voltages of 25 nm and 62 nm particles are similar at all scan rates, the reduction voltage increases less for the smaller NPs, leading to the reduced overpotential. The potential mechanism explaining the lower reduction voltage will be discussed in more detail below, but likely arises because the smaller NPs have shorter diffusion lengths, mitigating ionic and ohmic losses. The energetics and shapes of the CVs highlight the importance of smaller NPs for maintaining lower desalination energies, especially at faster desalination rates.

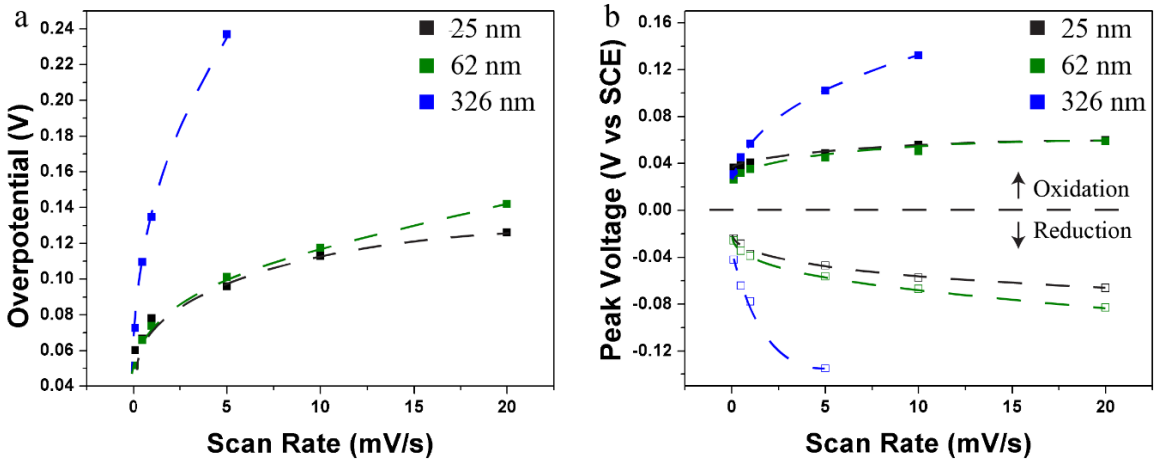

Figure 3.6 (a) Overpotential versus scan rate for each particle size. (b) Changes in the oxidation reduction peak voltages as a function of scan rate for all particle sizes.

3.5 Galvanostatic Charge-Discharge

The desalination energy of the Ag NPs is directly assessed through galvanostatic testing at 0.25 A/g (Figure 3.7a) and 2.5 A/g (Figure 3.7b) with a salt removal capacity of 53 mg Cl^-/ g Ag. Galvanostatic testing was only performed using 25 nm and 326 nm particles because of the larger changes in energy consumption. The salt removal capacity is on par with the highest salt removal capacities reported and are significantly higher than CDI capacities. To put these rates in context, assuming a full cell with a Na

electrode of the same capacity (40 mAh/g or 34.4 mg Na^+/g), at 2.5 A/g a desalination battery could produce fresh water at a rate of ~1850 L/day/kg. Figure 3.7a shows charge discharge curves for 25 nm and 326 nm particles at 0.25 A/g with the 25 nm particles clearly having a lower overpotential due to lower oxidation and reduction voltages. At 2.5 A/g (Figure 3.7b) this trend continues. While charging, the voltage increases linearly due to increased resistance of the AgCl layer, as reported previously.[100] The desalination energies in Wh/L for 25% Cl^- removal are shown in Figure 3.7c and are calculated using the area between the charge and discharge curves. The energy consumed for 25% Cl^- removal is calculated to compare to other literature and because the solution resistance will increase when a large percentage of the ions are removed, causing an increase in energy requirements. The desalination energies of 25 nm and 326 nm particles at 0.25 A/g are 0.09 and 0.15 Wh/L and at 2.5 A/g are 0.26 and 0.39 Wh/L respectively. Notably, the desalination energy of 25 nm particles is 0.06 Wh/L and 0.13 Wh/L lower at the different rates, a decrease of 30-40%. The desalination energies of 25 nm particles at both rates are lower or comparable to reverse osmosis and the initial desalination battery.[44, 48] The lower overpotentials in smaller Ag NPs is partially due to lower strain accommodation energy and lower free energy barriers to nucleating AgCl, similar to size effects of $LiFePO_4$ cathodes hydriding/dehydriding Pd cubes.[101, 102] Pairing the small Ag NPs with an energy efficient anode such as $Na_3V_2(PO_4)_3$ or $NaTi_2(PO_4)_3$ (assuming an overpotential of 50 mV for the Na^+ electrode at 1C) could allow for salt water desalination with extremely low desalination energies around 0.3 Wh/L for 25% salt removal, minimizing energy costs throughout the lifetime of the device.[49, 103]

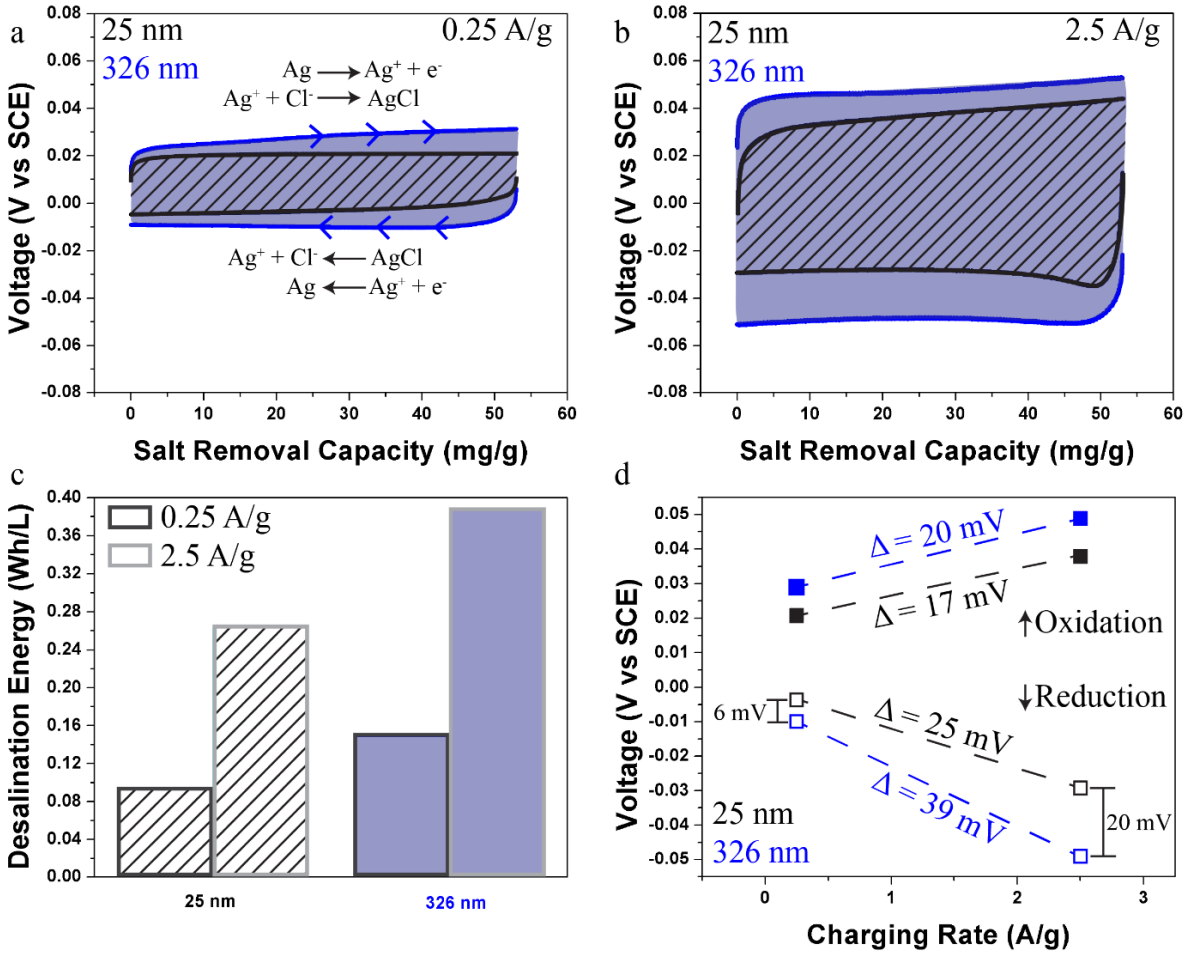

Figure 3.7 (a, b) Galvanostatic charge discharge for 53.3 mg Cl- / g Ag for 25 nm and 326 nm particles at 0.25 and 2.5 A/g respectively. (c) The desalination energy calculated from Figures 3a, b using the area between the charge and discharge curves. (d) Changes in the oxidation and reduction voltages as a function of charging rate.

A closer examination of the charge discharge curves reveals similar trends as seen in the CVs where the main improvement in overpotential for the 25 nm particles arises from smaller changes in the reduction voltages. The average oxidation voltage increases by similar amounts (17 mV and 20 mV) for smaller and larger particles, however the reduction voltage of 326 nm NPs increases in magnitude by 39 mV, while the smaller particles' reduction voltage only increases by 25 mV (Figure 3.7d). This yields a six mV difference between the two particle sizes at 0.25 A/g but 20 mV at 2.5 A/g. The drastically decreased voltage during

the reduction of AgCl arises from a thinner AgCl layer formed on smaller NPs. The thinner layer provides shorter diffusion lengths, decreasing both ionic and electronic resistances.

3.6 Characterization and Mechanism

EDS maps and TEM images confirm the thin AgCl layer grown on 25 nm particles after chlorination at 53 mg/g. Figure 3.9a shows a five to seven nm layer of AgCl grown on top of a small Ag NP with individual maps and a line scan shown in Figure 3.9b-d highlighting the sparse AgCl coating. Although there is overlap between the Ag and Cl peaks in EDS, a survey spectrum of AgCl has a much higher Cl/Ag ratio than Ag (Figure 3.8a).

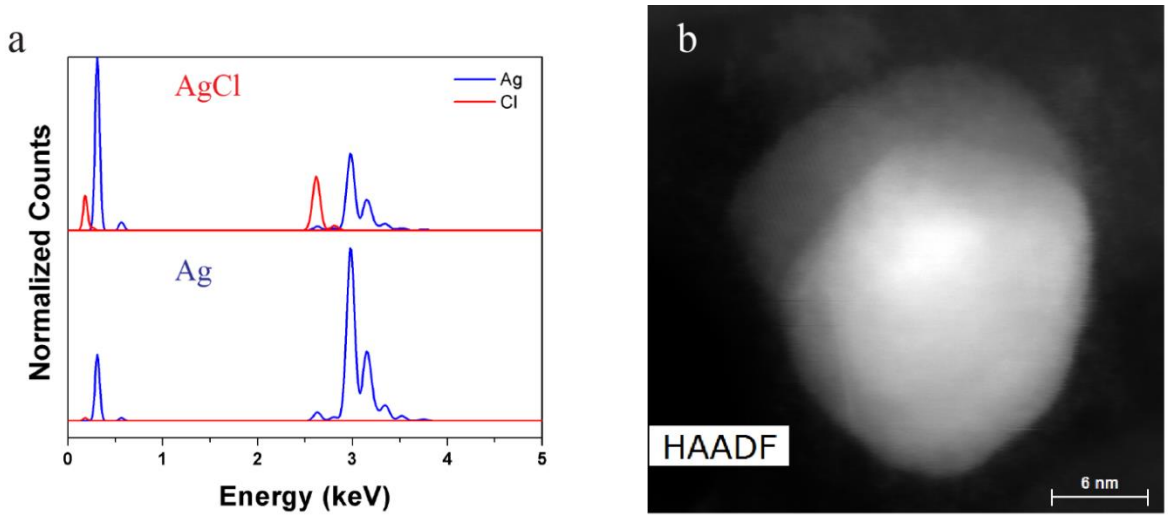

Figure 3.8 a) Spectra from the Ag and AgCl regions of the nanoparticle. Although there is an overlap between a Ag and Cl peak, the Cl/Ag ratio is much higher in the AgCl region. b) HAADF of the Ag NP where the contrast between Ag and AgCl arises from the lower density of AgCl.

TEM of the same particle in the EDS map reveals lattice fringes of both Ag and AgCl (Figure 3.9e). A diffraction pattern for the Ag region shows reflections for the (111) and (220) planes of Ag with an interlayer spacing of 0.232 and 0.148 nm (left inset Figure 3.9e). The diffraction pattern of the AgCl region shows the same Ag spots but an additional reflection corresponding to the (220) planes of AgCl with interlayer spacing of 0.198 nm (right inset Figure 3.9e).

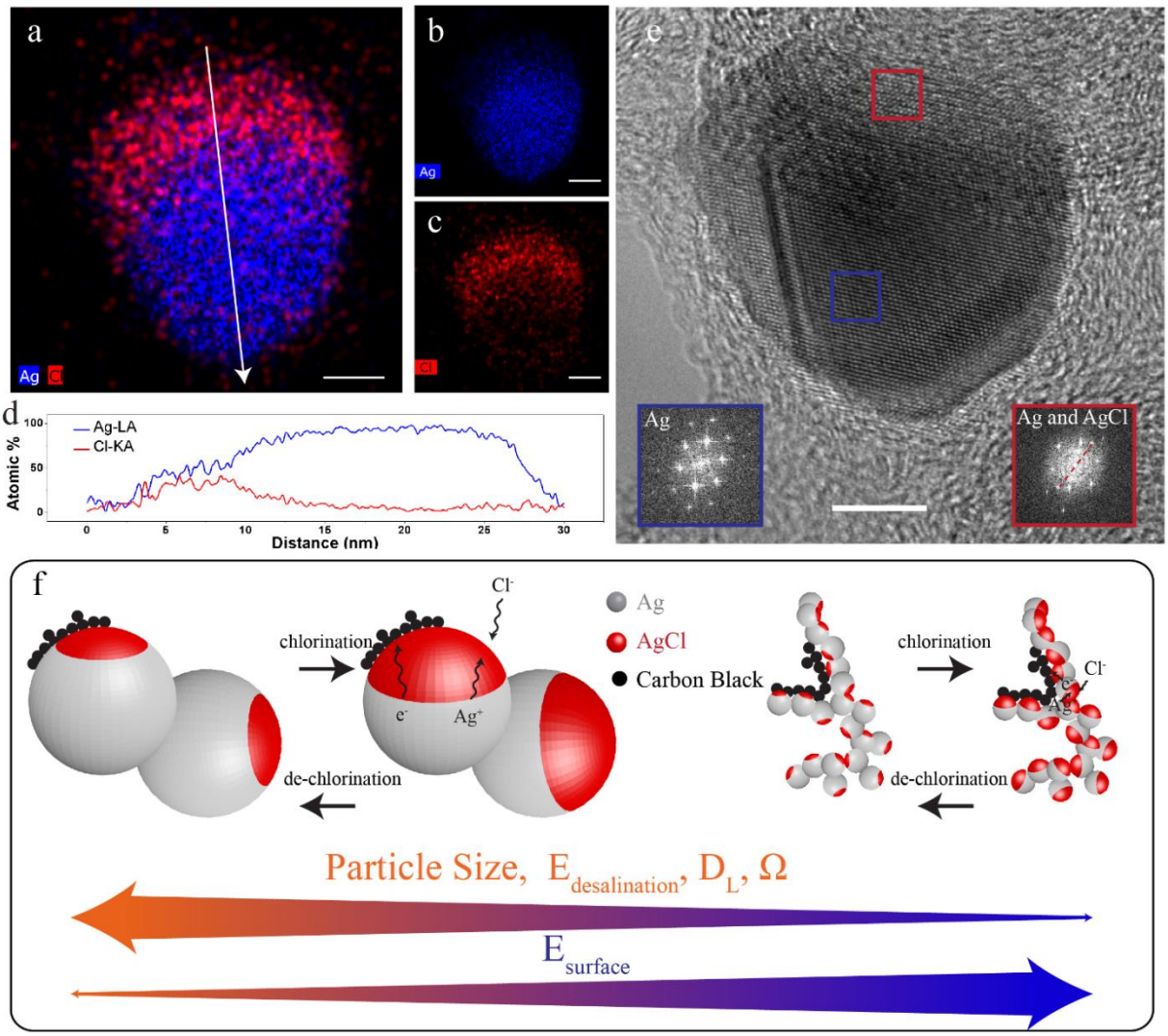

Figure 3.9 (a) STEM image of a chlorinated Ag nanoparticle with the arrow indicating the direction of the line scan in d). (b-c) Individual elemental maps for Ag and Cl. (d) Line scan of the chlorinated particle in a). (e) TEM of the same Ag NP in a. left inset) Diffraction pattern from the Ag region. right inset) Diffraction patter from the AgCl region. f) Schematic of the various process in the electrochemical Ag/AgCl reaction that are influenced by the size of Ag nanoparticle electrodes. All scale bars = 5 nm.

The thin AgCl layer leads to shorter diffusion lengths and smaller ionic and ohmic resistances, enabling lower desalination energies (Figure 3.9f). While there is not complete agreement in the literature of the Ag/AgCl electrochemical mechanism, it is generally accepted that during AgCl formation, the first step is the oxidation of Ag^0 to Ag^+ at the Ag/AgCl interface followed by diffusion of Ag^+ and Cl^- either in solution through microchannels or through the solid state of AgCl, leading to ionic resistances.[100, 104, 105]

The Ag NPs used for desalination also have electronic resistance because there is not necessarily a conductive pathway from the Ag to the conductive carbon black after AgCl films have formed. This work has not focused on determining whether ionic or ohmic resistances are most limiting, but regardless of which ion or charge carrier is most diffusion limited, all the diffusion lengths are reduced when using smaller Ag NPs, decreasing both ionic and ohmic resistances. After diffusion occurs there is a chemical reaction of $Ag^+ + Cl^- \rightarrow$ AgCl at the AgCl/electrolyte interface. Some authors suggest that AgCl islands nucleate and grow outward until a complete layer is formed and then the AgCl continues to grow thicker.[104] During AgCl reduction, the opposite process occurs but the net reaction occurs at the Ag/AgCl interface as opposed to the AgCl/electrolyte interface during oxidation. The larger increase in reduction voltage than oxidation voltage when going from 0.25 A/g to 2.5 A/g shows that the reduction process is more resistive than the oxidation process. Therefore, using smaller NPs has a more drastic effect on energy during the reduction of AgCl. Another possible reason for the differences between the oxidation and reduction voltages at higher currents is the kinetic limitations of the chemical reaction $Ag^+ + Cl^- \leftrightarrow$AgCl. The rate constant of the reverse reaction is likely smaller than the forward reaction, leading to a kinetic limitation as supported by the CV data. Smaller particles have a higher surface energy and enhance the kinetics of the chemical reaction, mitigating this bottle neck, further reducing the overpotential at faster rates.[60] This highlights the decreased resistance and improvement of sluggish reduction kinetics when using smaller NPs.

3.7 Conclusion

The size dependence of the desalination energy of Ag NP electrodes has been shown to decrease with nanoparticle size. 25 nm nanoparticles require 30-40% lower energy to remove 53 mg Cl^-/g Ag than 326 nm particles. This work connects the size dependence of electrochemical and chemical reactions to the performance of a desalination battery. The lower energy requirements are a result of a lower nucleation barrier and decreased diffusion lengths leading to lower ionic and ohmic resistances. A greater

improvement in the limiting process during the reduction reaction was the major contributing factor for lower desalination energies. Controlling the nanoparticle size for both Na^+ and Cl^- electrodes in a desalination battery could continue to reduce the desalination energy and improve high rate desalination capacities.

Chapter 4 Mechanism of Potassium Ion Intercalation Staging in Few-Layer Graphene from in-situ Raman Spectroscopy

4.1 Introduction

As mentioned earlier, potassium ion batteries are an emerging field with the potential of achieving lower costs than LIBs through the use of more abundant and cheaper active materials. Since this field is relatively new, although the performance of graphite anodes in a PIB have been proven, there is little understanding of the staging process. In this work, we experimentally assess the staging characteristics of K-ion batteries by performing *in-situ* Raman spectroscopy on few-layered graphene materials during K-ion intercalation. Although the chemical deintercalation of K-ions from graphite in a high vacuum and high temperature (>200 °C) process has been well studied with Raman,[106] this work focuses on a room temperature electrochemical process. As Raman spectroscopy provides a sensitive and non-invasive probe to assess structural and chemical effects occurring during intercalation, we identify a staging mechanism where K-ions first arrange into a dilute stage I compound, followed by a sequence of ordered staged intercalation compounds that transition from KC_{72} to stage I at KC_8. Raman spectra can be directly used to identify the stage number, as confirmed by X-ray diffraction.[106, 107] This provides greater understanding of the reactions occurring at the peaks and plateaus during electrochemical testing. Our work highlights a mechanism for staging that provides a pathway for a straightforward transition on the anodic side to K-ion batteries building upon the current understanding of Li-ion staging mechanisms.

4.2 Staging of Li^+ in Graphite

The prevalence of a graphite anode in a LIB has preempted many studies on the insertion mechanism of Li^+ in graphite, known as intercalation. Intercalation proceeds through an ordered process known as staging where the stage number is the number of graphene layers between layers of intercalants. It becomes energetically favorable for the ions to fill galleries between the same layers of graphene before

filling galleries between new graphene layers.[108] Staging proceeds from stage VI → V → IV→ III → II → I. Upon reaching a stage I graphite intercalation compound (GIC), every graphene layer is adjacent to two layers of intercalants. The Daumas-Herold model provides a realistic model for intercalation to explain the transition between stages when lithium ions can only move within a plane and not through plane (Figure 4.1).[109] The enhanced strain in the bending of graphene layers around intercalants proposed by the Daumas-Herold model can be seen through sensitive techniques such as Raman spectroscopy.

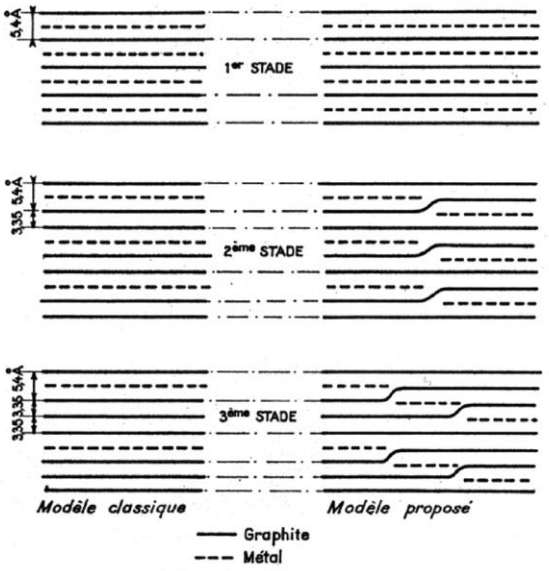

Figure 4.1 Comparison of the idealized view (modele Classique, left) of various stage phases for a metal GIC with the sketch of the realistic model (showing the Daumas-Herold-type defects, modele propose, right). Reproduced from ref. [108] with permission from RSC

Raman spectroscopy is a technique that probes phonon vibrational modes in a material.[110] Carbon materials are particularly useful to study with Raman spectroscopy because changes in local bond configuration, electronic properties, defects, and more can all be detected (Figure 4.2).[111] In-situ Raman spectroscopy has been extensively used to study carbon nanotube growth[112, 113] and Li^+ intercalation into graphite.[107, 114, 115]

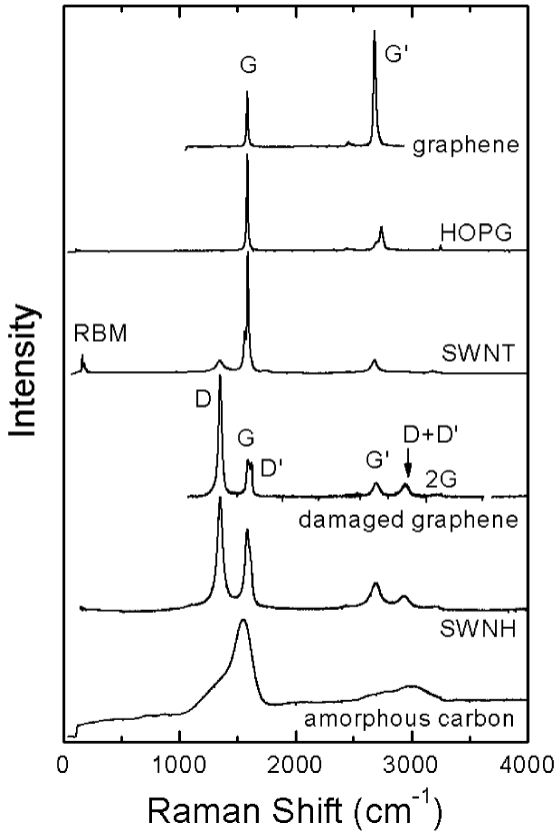

Figure 4.2 Raman spectra from different types of sp^2 nanocarbons. Reproduced from ref. [111] with permission from ACS

When a LASER interacts with a material, most of the photons are absorbed and reemitted at the same wavelength, known as Rayleigh or elastic scattering. Raman scattering occurs when the excited electron reemits a photon of slightly lower energy and a phonon is produced to maintain the conservation of energy (Figure 4.3).[110] In a Raman spectrometer, specialized filters are used to block Rayleigh scattering, allowing the lower energy photons to be detected. The resulting spectra showing the phonon energies of a material can act as a fingerprint to identify and to track changes in the material as it is tested. For example, graphene has a few characteristic peaks known as the G and 2D peaks at ~1580 and ~2700 cm^{-1} respectively.[110] The G peak arises from the in-plane E_{2G} optical phonon mode while the 2D peak is a defect mediated double resonance mode.[110] The relative intensities of the 2D/G peaks can be used to identify the number of graphene layers, with single layer graphene having a maximum intensity ratio

around four.[116] The peak location, full width at half maximum (FWHM), and intensities all give insight into the local atomic and electronic environment. For example, increased biaxial strain causes a red shifting of the G peak position.[106] For these reasons, Raman spectroscopy has been extensively used to study LIB anodes.

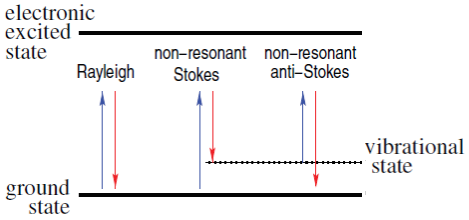

Figure 4.3 Rayleigh and Raman scattering processes. Reproduced from ref. [110] with permission from Nature

In LIBs, staging can be tracked with Raman spectroscopy because graphene layers adjacent to intercalant layers become highly charged, causing a blue shifted G-peak to arise, known as the G-charged or G_c.[107, 115, 117] Charging causes the G peak to blue shift due to increased carrier concentration.[114, 118, 119] As staging progresses, the G_c peak becomes larger as more layers become charged while the G_{uc} peak shrinks. The intensity ratio of the G_c and G_{uc} peaks is correlated to the stage number. Although the increased charge carrier density causes a blue shifted G peak, increased interlayer strained explained by the Daumas-Herold model can be seen through red shifting of the peak positions. Even though a K^+ is similar to a Li^+, the presumption that these ions stage through a similar process should not be assumed. Staging for Li^+ is drastically changed from carbonate to ether-based solvents.[120]

4.3 Experimental Details

4.3.1 Growth of Few Layer Graphene on Nickel Foam

FLG was grown on Ni foam using a homemade chemical vapor deposition (CVD) reactor. The Ni was placed under vacuum (2.0×10^{-1} torr) and heated to 750°C in Ar (250 sccm) and H_2 (two sccm) and then exposed to C_2H_2 (one sccm) for 25 minutes at thirty torr before cooling.

4.3.2 Assembly and testing of batteries

Batteries were assembled in an Ar glove box using a K metal electrode on a stainless-steel disk, 0.8 M KPF_6 in one:one EC/DEC (v:v) electrolyte, a Whatman grade GF/A glass microfiber filter separator, and CVD grown FLG on Ni foam, all encapsulated in a coin cell. Galvanostatic cycling studies from 1.5 V to 0.01 V were performed on an MTI 8 channel battery analyzer. Immediately prior to all electrochemical tests, the batteries were allowed to reach open circuit voltage over one hour. The capacity is normalized to the mass of the FLG and all voltages reported are vs K/K^+.

4.3.3 Characterization using Raman spectroscopy

Raman measurements were performed using a Renishaw inVia Raman spectrometer with a 532 nm laser. All Raman spectra are fit with a linear baseline to remove background noise and flatten the spectra. *In-situ* Raman spectroscopy was performed using a modified coin cell with a hole drilled in the top. After the coin cell was assembled and crimped in a glove box, a thin cover glass slide with epoxy was placed over the hole, with care taken to seal the glass slide to the coin cell, preventing air exposure, and not to expose the electrolyte to epoxy. A picture of the in-situ cell is shown in Figure 4.4. Since no electrochemical reactions occur above 0.5 V the voltage was set to 0.5 V and held for one hour. Then a linear sweep voltammogram (LSV) was carried out at 0.05 mV/s scan rate from 0.5 V to 0.01 V. Raman spectra were taken every 720 seconds from 0.5 to 0.37 V and every 110 seconds between 0.37 and 0.01 V.

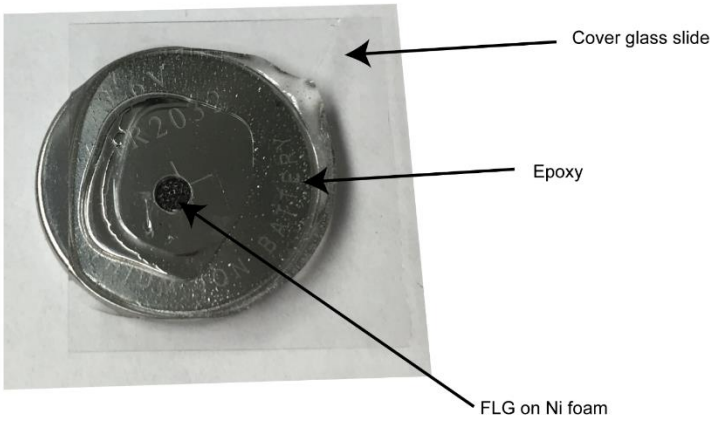

Figure 4.4 Picture of the in-situ Raman cell

4.4 Electrochemical Data

Few layer graphene on Ni foam is well-suited for *in-situ* Raman spectroscopy since the Ni foam backbone is both a structural support and current collector, and the high foam porosity allows good electrolyte penetration. A scheme of the general *in-situ* Raman spectroscopy setup, a characteristic Raman spectrum, and a characteristic transmission electron microscope (TEM) image of the FLG material are shown in Figure 4.5a-c, respectively. Raman spectroscopy using a 532 nm laser reveals two peaks, the G peak at 1582 cm^{-1} and the 2D peak at 2705 cm^{-1} (Figure 4.5b). The G peak arises from the in-plane E_{2g} vibrational mode of sp^2 carbons while the 2D mode is a two-phonon band whose position, shape, and intensity elucidate the number of graphene layers.[121] Due to the crystalline nature of the FLG, no D peak from defective sp^3 carbons is observed. A Raman map of 100 points over a 40 µm by 40 µm area has an average 2D/G ratio of 0.75 indicative of few layer graphene (Figure 4.6).[121] This is consistent with TEM images (Figure 4.5c). There is little spot to spot variation, seen the normally distributed G peak positions with an average of 1582.4 cm^{-1} and a low standard deviation of 0.66 cm^{-1}, justifying the isolation of a single point for analysis.

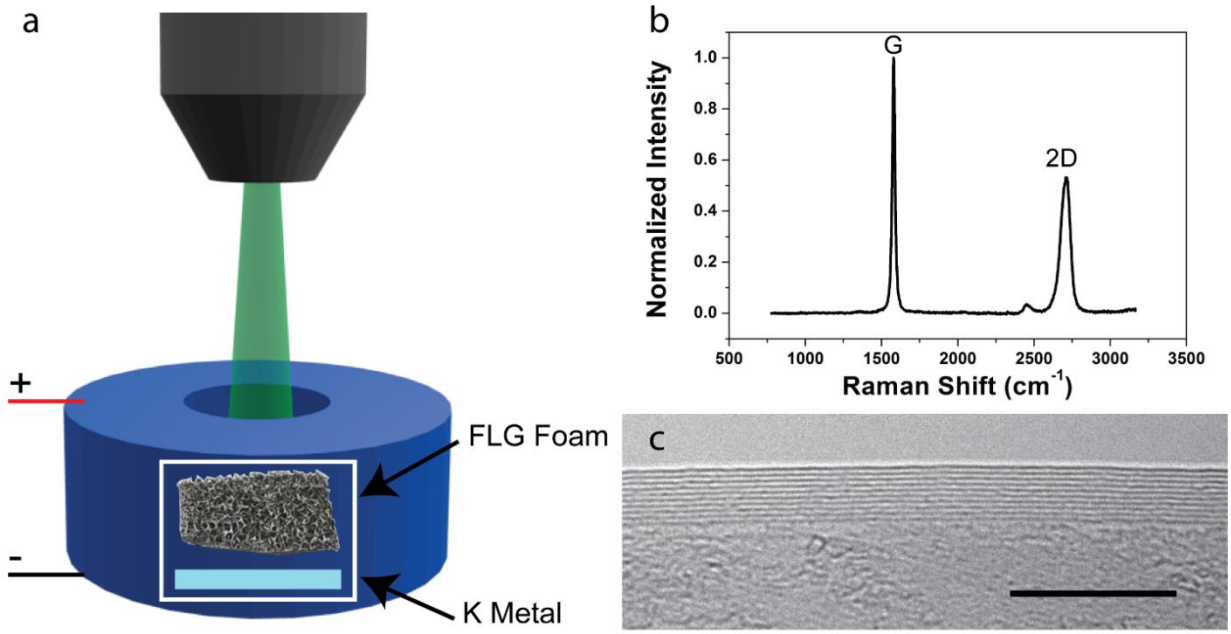

Figure 4.5 a) Schematic of the battery testing with *in-situ* Raman spectroscopy b) Raman spectrum of FLG on Ni foam. c) TEM of the few layer graphene. Scale bar = 10 nm. Reproduced from ref. [122] with permission from RSC

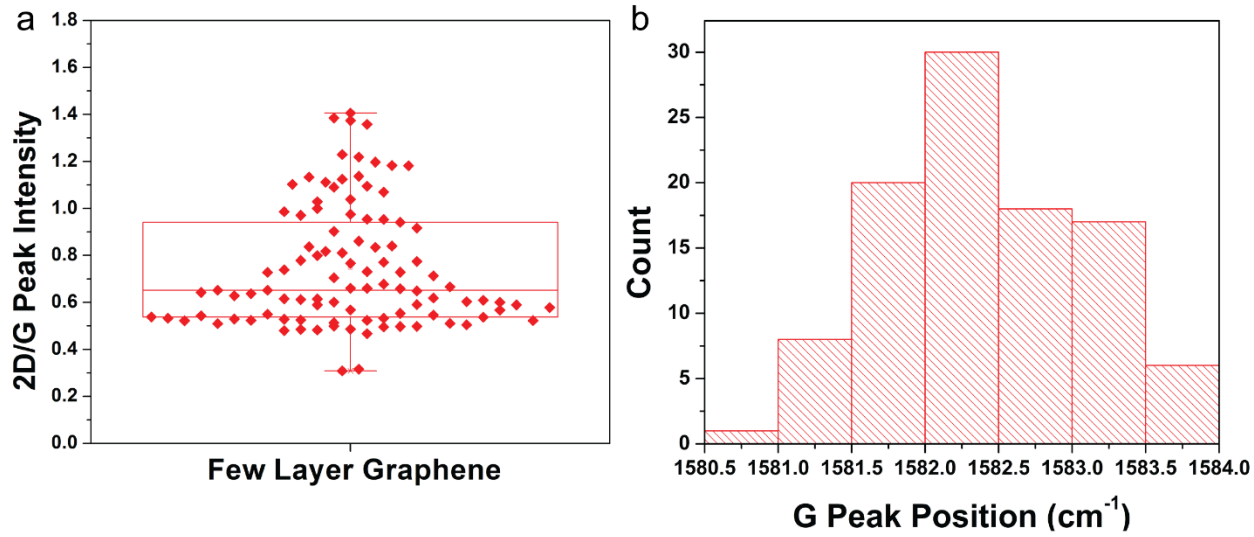

Figure 4.6 a) 2D/G intensity scatterplot of carbonized nickel foam taken over a 40 µm x 40 µm area. b) G peak variation over the Raman map. The peak positions are normally distributed with an average position of 1582.4 cm^{-1} and a standard deviation of 0.66 cm^{-1}. The low standard deviation exemplifies the small spot to spot variation and justifies the use of a single point during the in-situ testing.

A differential capacity plot (Figure 4.7a) and corresponding charge-discharge curves (inset Figure 4.7a) from galvanostatic testing at 50 mA/g reveal behavior consistent with previous reports using carbon-based anodes.[39, 40] The main reduction peak occurs from 0.2 to 0.01 V with a small shoulder around 0.18 V, while a small reduction peak around 0.8 V on the first cycle is due to SEI formation. Until now the electrochemical processes causing these peaks has not been well understood, but as a result of the *in*-situ Raman analysis presented here, we assign the shoulder to the formation of stages VI to II while the majority of the reduction peak is due to the transition from stage II to I. Similarly, there are two oxidation peaks at 0.32 V and 0.42 V due to the reverse staging process during de-intercalation. Notably, literature reports indicate disagreement between the formation of a stage II compound as KC_{24} or KC_{16}.[39, 40] During the second charge, ~ 110 mAh/g and 40 mAh/g of capacity are associated with the first and second plateaus respectively. The ratio of the capacities for these peaks is around three, which would correspond to a transition from KC_{24} to KC_8 and not KC_{16} to KC_8 which have a capacity ratio of around two. 100 charge-discharge cycles at 100 mA/g reveals expected cycling behavior for this material with an

initial decrease in capacity and a stable capacity around 140 mAh/g (Figure 4.7b). Rate testing at 50, 100, and 200 mA/g can be found in Figure 4.8 and shows agreement with that observed in other reports.[39]

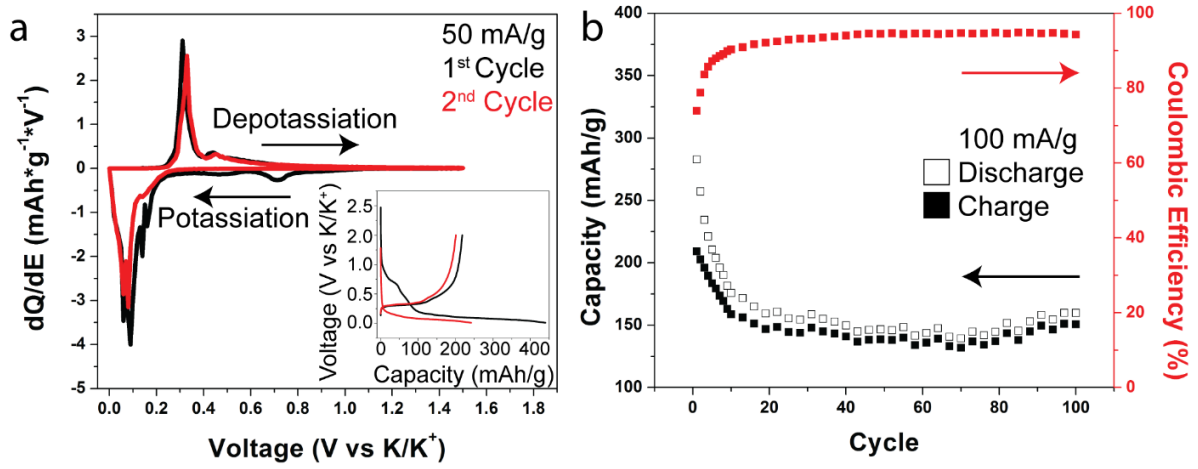

Figure 4.7 a) Differential capacity plot at 50 mA/g, inset) corresponding charge-discharge curves. b) Cycling data at 100 mA/g

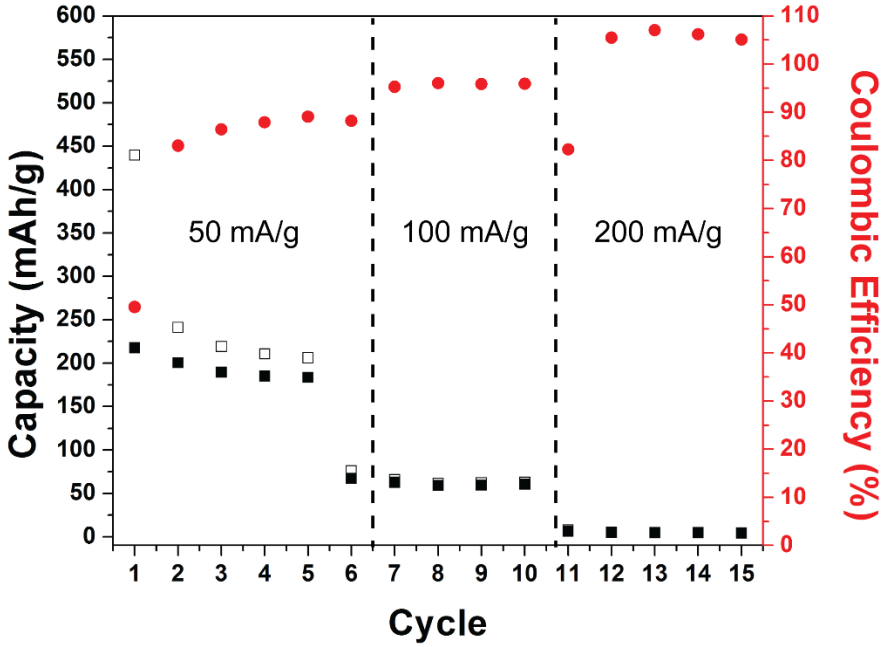

Figure 4.8 Galvanostatic rate study with five cycles at each of 50, 100, and 200 mA/g

4.5 In-situ Raman

The LSV during the *in-situ* study (Figure 4.12a, top) has a similar shape to the dQ/dE plot (Figure 4.7a) with a small peak around 0.18 V and a larger peak around 0.08 V. Relaxation times during galvanostatic intermittent titration technique (GITT) were used to ensure the electrode is near equilibrium throughout the LSV at the very slow rate of 0.05 mV/s (Figure 4.9).

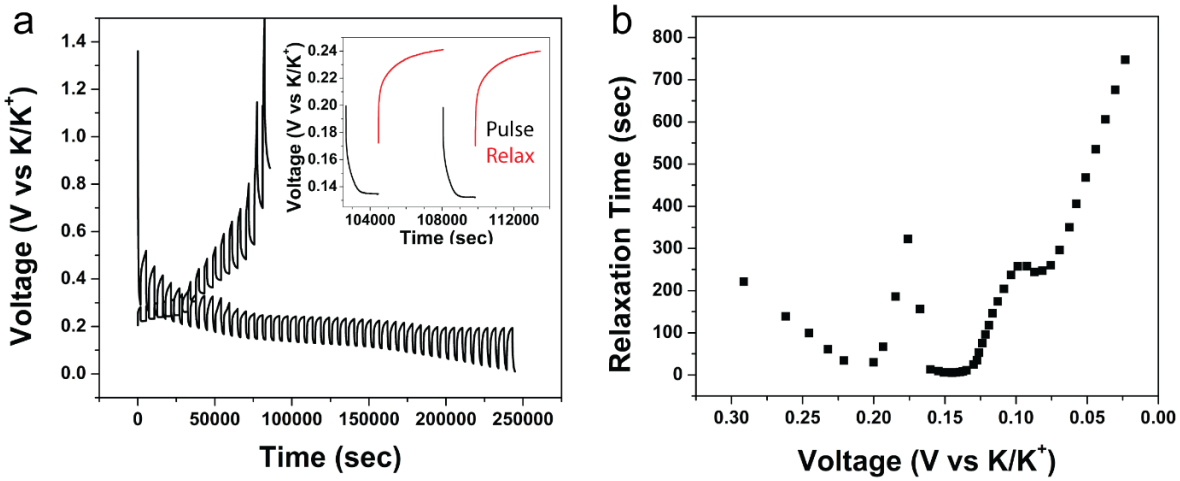

Figure 4.9 a) Galvanostatic intermittent titration technique (GITT) using a galvanostatic pulse at C/10 (27.8 mA/g) for 30 minutes followed by a one hour relaxation (inset Figure 4.9). The relaxation period in GITT allows the electrode to reach equilibrium, as seen by the potential plateau. This relaxation period can be used to assess the time it takes to reach equilibrium. For each relaxation period, the amount of time to reach 80% of the final relaxed voltage was calculated. This was plotted versus the final pulse voltage (Figure 4.9b). The maximum time in the voltage range used for Raman analysis is 300 sec, although the time to reach equilibrium during the main peak in the CV (<0.15 V) is below ten seconds. During the 0.05 mV/s CV used for the in-situ Raman experiments, the maximum relaxation time of 300 sec (an overestimate) corresponds to a 0.015 V change, within the resolution of the spectra shown in Figure 4.12b. Below 0.075 V the relaxation time increases but by that voltage the metallic nature of the near stage I GIC interferes with the Raman spectra and does not provide additional information.

The relaxation time during the main electrochemical reaction is only a few seconds and is much smaller than the Raman scan times. The G peak positions and intensities are shown in the bottom and middle of Figure 4.12a respectively. An analogous plot for the 2D peak can be found in Figure 4.10.

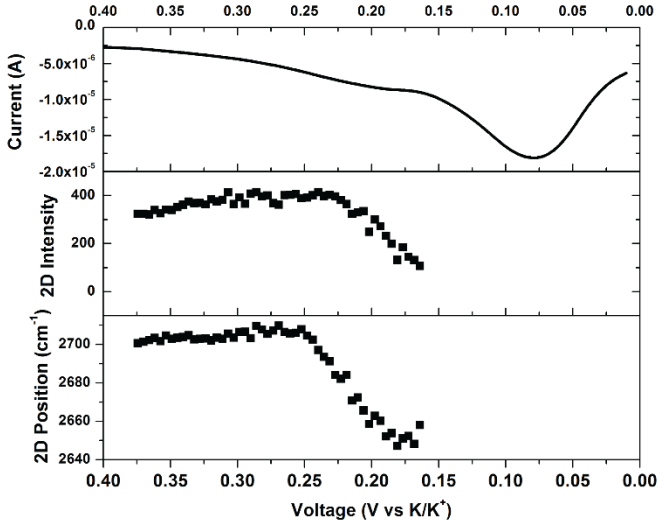

Figure 4.10 In-situ peaks fit data for the 2D peak

Selective Raman spectra are shown in Figure 4.12b for different states of charge indicated in Figure 4.12a. Figure 4.12c displays all Raman spectra taken from 0.37 V to 0.01 V in a waterfall plot. Together these plots help visualize and quantify the distinct peaks shifts and intensity changes of the Raman spectra. A D peak around 1336 cm^{-1} can arise due to degradation of the FLG but throughout the experiment, no D peak is observed (Figure 4.11).[120]

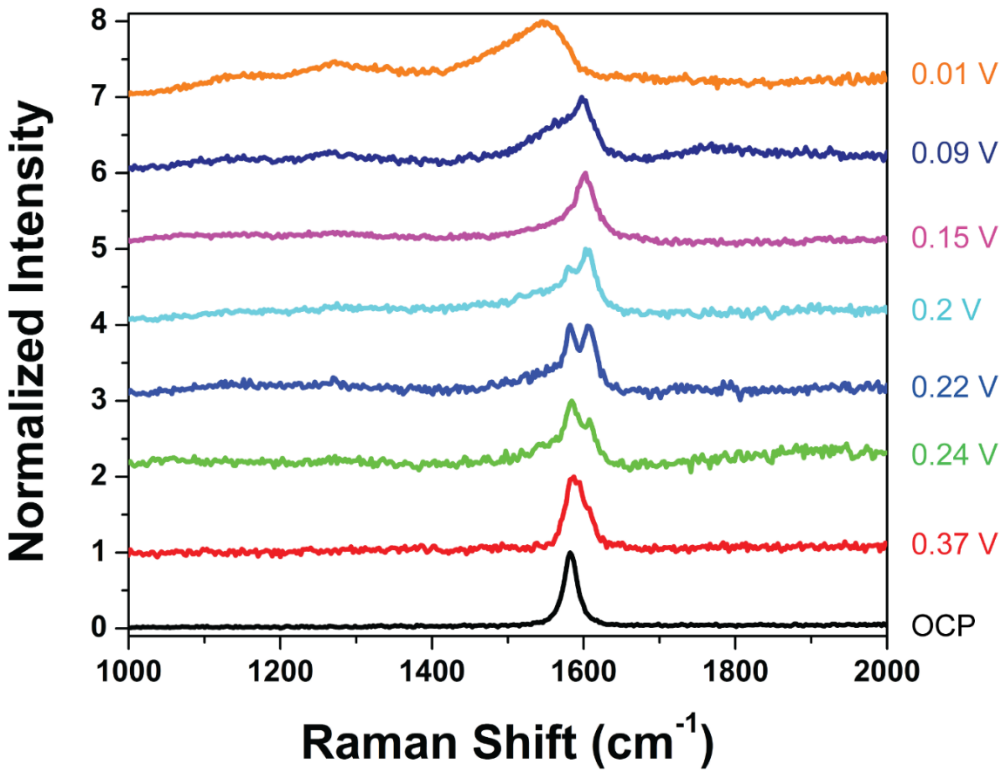

Figure 4.11 Selective Raman spectra from the *in-situ* experiment with a larger range of wavenumbers. A D peak around 1336 cm^{-1} is not observed during the *in-situ* study.

An initial scan taken at 2.0 V reveals a similar spectrum to FLG containing 2D and G peaks with the G peak at 1582 cm^{-1}. At 0.37 V the G peak blue shifts to 1589 cm^{-1} attributed to the formation of a dilute stage I GIC. The shift of the G peak to higher frequencies occurs because of a breakdown of the adiabatic Born-Oppenheimer approximation in graphene causing a stiffening of the E_{2g} mode as the carrier concentration increases uniformly.[123] From 0.37 to 0.25 V minimal change is observed in both the electrochemical and Raman data attributed to the sparse ion composition of the dilute stage I compound. Near 0.24 V the first reduction peak occurs in the LSV as ordered staging begins, indicated by a higher frequency shoulder on the G peak and a decrease in 2D intensity. Initially, charge is equally distributed between all layers and only a single uncharged G peak (G_{uc}) is present. When cations start to intercalate into graphite, the charge density increases on layers adjacent to the intercalants, forming an up-shifted G_c

(G charged) peak.[118, 120, 124] The graphene layers not adjacent to the ions continue to show the G_{uc} peak leading to a doublet in the Raman spectra at staging above stage II.[107, 117] At 0.24 V the G_c/G_{uc} intensity ratio is indicative of stage VI KC_{72}.[106] From 0.24 V to 0.15 V the G_c peak increases in intensity, the G_{uc} and 2D peaks decrease, and all peaks red shift. The opposite behavior of the G_c and G_{uc} intensities is due to continued staging where more graphene layers become charged and fewer uncharged layers remain. Both the G_{uc} peak and 2D peak have vanished by 0.15 V. The graphene 2D peak position and intensity changes can be explained by the increase in electron concentration during intercalation.[125, 126] Stage II no longer involves any uncharged graphene layers, correlating the disappearance of the G_{uc} peak to the emergence of a stage II compound. From 0.15 V to 0.01 V the Raman spectra evolve from a symmetrical G peak to an asymmetric fano-resonance shape due to interference between the metallic like behavior of stage I GICs and the resonant phonon scattering process.[106] Optical microscope images of the FLG at open circuit voltage and 0.01 V also supports the formation of stage I KC_8, seen by the change of color from grey to bright orange (inset Figure 4.12a).

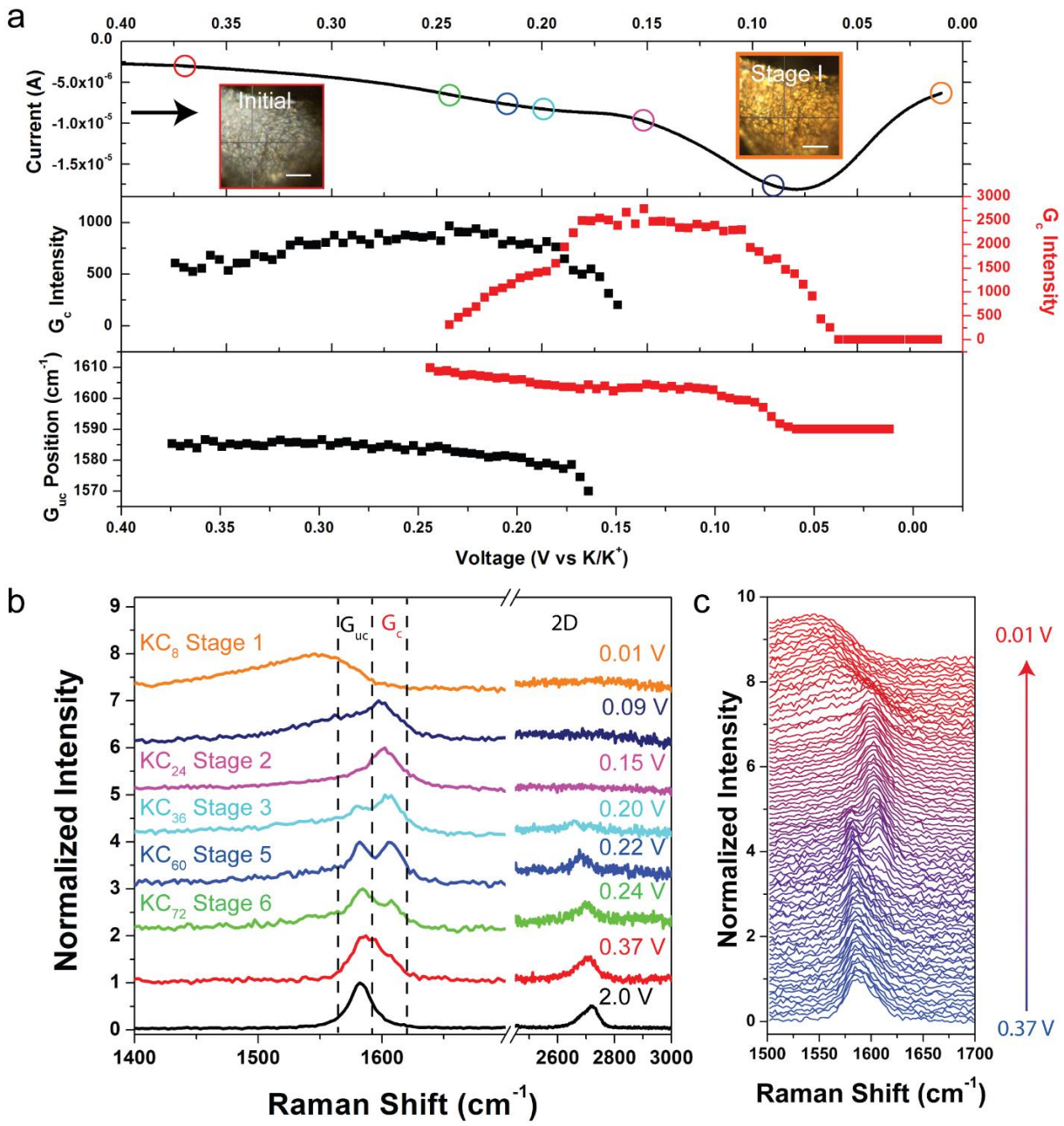

Figure 4.12 a) Top, LSV measured during the *in-situ* Raman experiment. The colored circles indicate the state of charge for the Raman spectra in Fig 3b. Middle, peak intensities for the G_{uc} and G_c peaks. Bottom, peak positions for the G_{uc} and G_c peaks. Inset) Optical microscope image of the FLG coated foam initially and fully potassiated. Scale bar = 20 µm b) Selective Raman spectra taken at different states of charge as indicated in the LSV. c) Waterfall plot of all Raman spectra taken between 0.37 V and 0.01 V.

The proposed staging mechanism is pictorially represented in Figure 4.13. Here, grey carbon layers in the schematic represent lightly strained/charged areas while orange layers represent more strained/charged sections. Raman modes are observed to red shift during potassiation due to biaxial strain that is common in electron donating GICs[28] due to expansion of the in-plane C-C bond.[127, 128] The strain originates from increasing electron density and possibly steric hindrance from intercalated ions. This is illustrated in Figure 4.13, in agreement with the Daumas-Hérold model which accounts for flexible graphene layers that can deform around intercalants.[129] Our *in-situ* Raman analysis corroborates the following staging sequence: (1) a dilute stage I compound at voltages greater than 0.24 V, (2) a transition from a stage IV compound at 0.24 V (KC_{72}) to a stage II compound at 0.15 V (KC_{24}), and (3) the formation of a stage I (KC_8) compound below 0.15 V. Despite the very different driving force between high temperature chemical potassiation and room temperature electrochemical potassiation of graphite, they proceed through similar mechanisms. Notably, this sequence is distinguished from staging of Na^+ in graphite, but is similar to the electrochemical stage of Li^+ in graphite.[114, 130] This elucidates a picture of potassium storage in graphitic materials that builds upon an extensive picture of lithium storage in graphitic materials that has emerged over the past few decades.

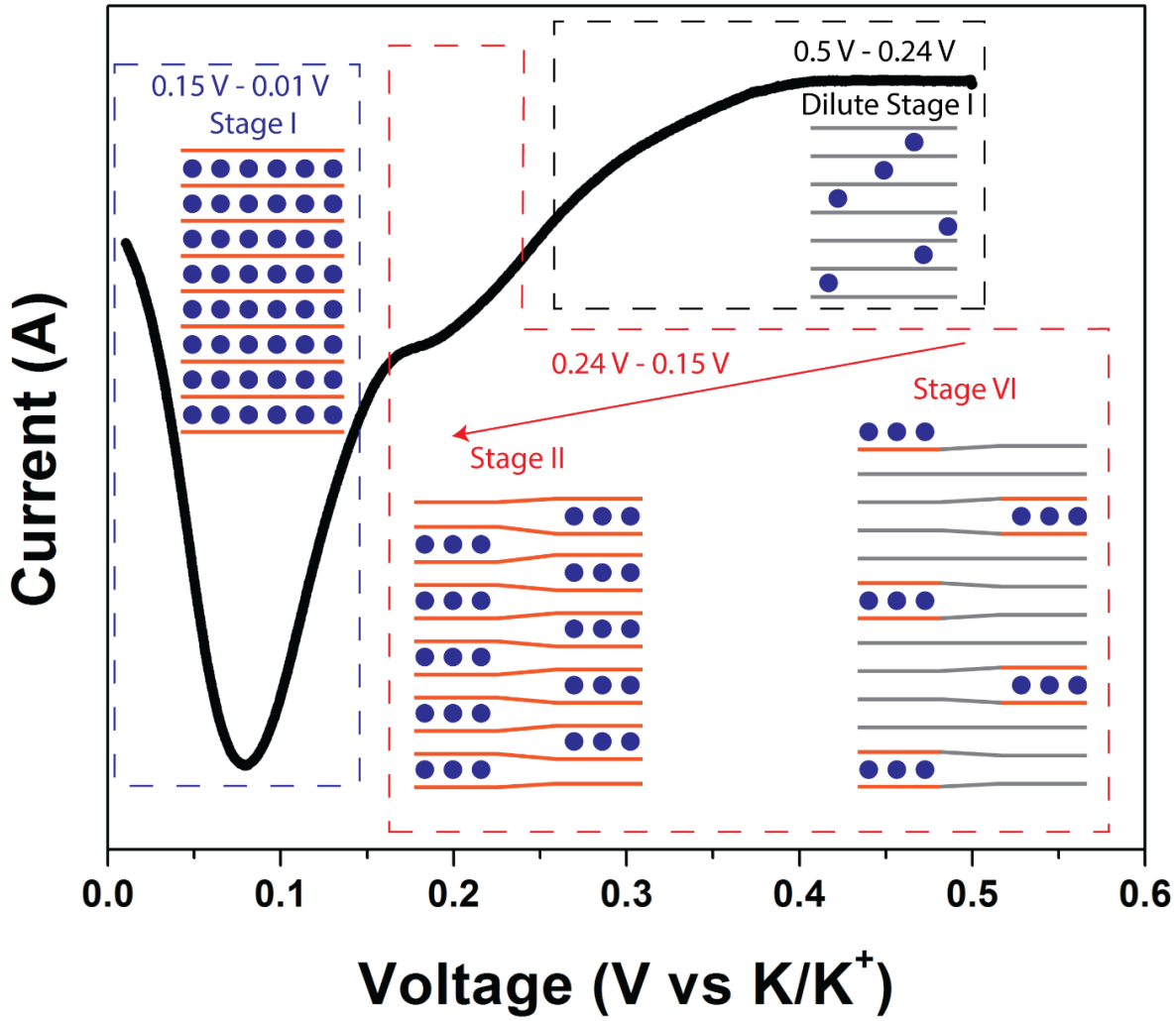

Figure 4.13 Schematic representing the staging mechanism revealed by the *in-situ* Raman experiments. The schematic shows the changes that occur in the FLG anode during potassiation. Grey graphene represents slightly charged/strained areas while orange graphene represents highly charged/strained sections.

4.6 Conclusion

In summary, we demonstrate an *in-situ* Raman spectroscopic analysis of electrochemical K-ion storage in FLG materials that reveals the first real time demonstration of staging in this system. We observe the formation of a dilute stage I compound that then transitions from ordered stage IV (KC_{72}) → stage II (KC_{24}) → stage I (KC_8) and are able to assign voltage ranges for each stage. This staging process

is notably different than that observed with Na^+ intercalation into graphitic materials, but similar to Li^+ intercalation. The similarities between staging in Li^+ and K^+, combined with ~ 1000X greater abundance of K in the earth's crust, and a higher operating voltage for K-ion compared to Na-ion elucidate a pathway for K-ion grid storage systems that can maintain performance, overcome manufacturing limitations, and build on an extensive set of knowledge obtained in past decades from the development of Li-ion systems.

Chapter 5 Role of Nitrogen-Doped Graphene for Improved High-Capacity Potassium Ion Battery Anodes

5.1 Introduction

Recent studies have identified the staging sequence in K-ion intercalation into graphitic carbons to closely resemble that of lithium intercalation. However, the bottleneck of maximum storage capacity associated with a KC_8 stage I GIC still poses a challenge to using this material as a replacement for Li-ion batteries since graphitic carbon anodes for Li-ion batteries exhibit over 30% increased capacity (LiC_6 – 372 mAh/g versus KC_8 – 278 mAh/g). To overcome this barrier, additional storage mechanisms beyond traditional staging are needed. Cathode research for PIBs is also limited. The larger K^+ size can make reversible intercalation into traditional cathodes like transition metal oxides and iron phosphates even more difficult so research has mostly focused on organic cathodes with inherently large interstitial sites.[21, 40, 131, 132] As one of the main advantages of PIBs is the use of the already commercialized graphite anode, cathode research should also be focused on adapting commercialized electrodes.

One effective strategy that has shown promise to increase the anode performance of graphitic carbons for Li-ion batteries is the introduction of charged defects or doping sites into the carbon lattice.[133] Dopants such as N alter the electronic structure and increase the reactivity by producing locally accessible active sites in the graphite lattice.[134, 135] Wang *et al.* doped graphene nanosheets with around 2% N and found a drastic improvement in the capacity and rate capability of a LIB.[136] At C/20 the capacity increased from 550 mAh/g to 900 mAh/g. Cho *et al.* formed nitrogen doped graphene layers deposited on silicon nanowires as lithium ion battery anodes.[137] Using both experimental results and DFT calculations they showed that both graphitic N and pyridine-like N can increase battery performance compared to undoped graphene. They proposed that the increased capacity is due to the formation of vacancies and dangling bonds around the N defects. Notably, recent efforts have also explored nitrogen doping for

sodium ion batteries and demonstrated the ability to improve performance even in the absence of the formation of a sodium ion GIC.[138, 139]

The scalability and control afforded by different synthetic routes of N doped graphene is important to the potential manufacturability of PIBs. Two common methods to produce doped graphene are through direct synthesis in one step such as that used in this study or doping of the graphene post synthesis through thermal or plasma treatment. Anywhere between one and ten atomic percent of N dopants are commonly achieved through either strategy.[135] Post synthesis treatment is particularly useful for battery manufacturing as the carbon electrodes currently being manufactured could be doped and improved using this method. Post synthesis methods also provide control of the bonding configuration of N dopants incorporated into the carbon.[140] Using plasma enhanced CVD for different amounts of time, Jeong et al showed that different N configurations have varying effects on ion storage, highlighting the importance of controlling the doping process to produce an optimized electrode.

In this study, we combine the use of graphitic anodes for potassium ion batteries with nitrogen doping techniques to overcome storage capacity limitations of KC_8 which bottleneck K-ion anodes from being competitive with the storage capacity of Li-ion batteries. We demonstrate that N-doping of few-layered graphene (FLG) can enable potassium storage capacity exceeding 350 mAh/g, compared to 278 mAh/g maximum capacity of KC_8, and through control studies and in-situ Raman studies identify the mechanistic role of N-doping to be related to local storage of K at N-doping sites during a staging sequence that remains invariant between doped and doped FLG.

5.2 Experimental Methods

5.2.1 Growth of FLG, N-FLG, and d-FLG

All samples were grown on Ni foam (110 ppi, >99.99% from MTI) using a homemade CVD reactor in a Lindberg Blue one inch tube furnace. In all cases the carbon was grown under vacuum ($2.0x10^{-1}$ torr). To grow FLG the Ni was heated to 750°C in Ar (250 sccm) and H_2 (2 sccm) and then exposed to C_2H_2 (1

sccm) for 25 minutes before cooling. To grow d-FLG, the Ni foam was placed in a magnetic quartz boat. The Ni was heated to 650°C in Ar (250 sccm) and H_2 (100 sccm) then exposed to C_2H_2 (10 sccm) for five minutes. Fast cooling was achieved by removing the Ni foam from the furnace using the magnetic boat. To grow N-FLG the Ni foam was heated to 550°C under Ar (250 sccm) and H_2 (100 sccm) and held for ten minutes. The temperature was then increased to 750°C. Liquid CH_3CN contained in a cylinder was opened for five minutes then closed for five minutes. The opening and closing of the cylinder was repeated two more times before slowly cooling.

5.2.2 Material Analysis

XPS analyses were performed in an Ulvac-PHI Versaprobe 5000 using monochromatic Al Kα x-rays (1486 eV), a 100 µm diameter x-ray spot, and a takeoff angle of 60 degrees off sample normal. Pass energies of 187.7 eV and 23.5 eV were used for the survey and high-resolution acquisitions, respectively. Charge neutralization was accomplished using 1.1 eV electrons and 10 eV Ar^+ ions. The energy scales of the high-resolution spectra were calibrated by placing the C-C type bonding in the carbon 1s spectrum at 284.8 eV. Relative atomic concentrations were calculated using peak areas and PHI handbook sensitivity factors.[141] Bonding configurations of nitrogen were assigned following the work of Kabir and coworkers.[142] Transmission electron microscopy was performed using an Osiris TEM at a beam voltage of 200 kV.

5.2.3 Assembly and Electrochemical Testing of Batteries

Batteries were assembled in an Ar glove box using a K metal electrode on a stainless-steel disk, 0.8 M KPF_6 in one:one EC/DEC (v:v) electrolyte, a Whatman grade GF/A glass microfiber filter separator, and a working electrode of FLG, N-FLG, or d-FLG on Ni foam, all encapsulated in a coin cell. Galvanostatic cycling and rate studies from 1.5 V to 0.01 V were performed on an MTI eight channel battery analyzer. CVs were performed using a Metrohm Aultolab Multichannel analyzer between 1.5 V and 0.01 V. The capacity is normalized to the mass of the carbon and all voltages reported are vs K/K^+.

5.2.4 In-Situ Raman Spectroscopy

Raman measurements were performed using a Renishaw inVia Raman spectrometer with a 532 nm laser and 1200 l/mm grating. All Raman spectra were baselined to remove background and normalized to the largest peak. *In-situ* Raman spectroscopy was performed using a modified coin cell with a hole drilled in the top described previously.[122] After the coin cell was assembled and crimped in a glove box, a thin cover glass slide with epoxy was placed over the hole, with care taken to seal the glass slide to the coin cell, preventing air exposure, and not to expose the electrolyte to epoxy. The voltage was set to 0.01 V for one hour and a stage I GIC was formed (seen by an orange color and an asymmetric fano-resonance line shape Raman spectrum). The battery was held at the desired voltage for thirty minutes before taking a Raman spectrum.

5.3 Material Characterization

Nitrogen doped few layer graphene (N-FLG) was grown on Ni foam using acetonitrile in a CVD process in a manner building from other reports and outlined in the methods section.[140, 143] The Raman spectra of N-FLG using a 532 nm laser is typical for that reported with N doped graphene and has multiple peaks including the G (1588 cm^{-1}), D (1365 cm^{-1}) , D' (1626 cm^{-1}), and 2D (2713 cm^{-1}) peaks (Figure 5.1a).[140]

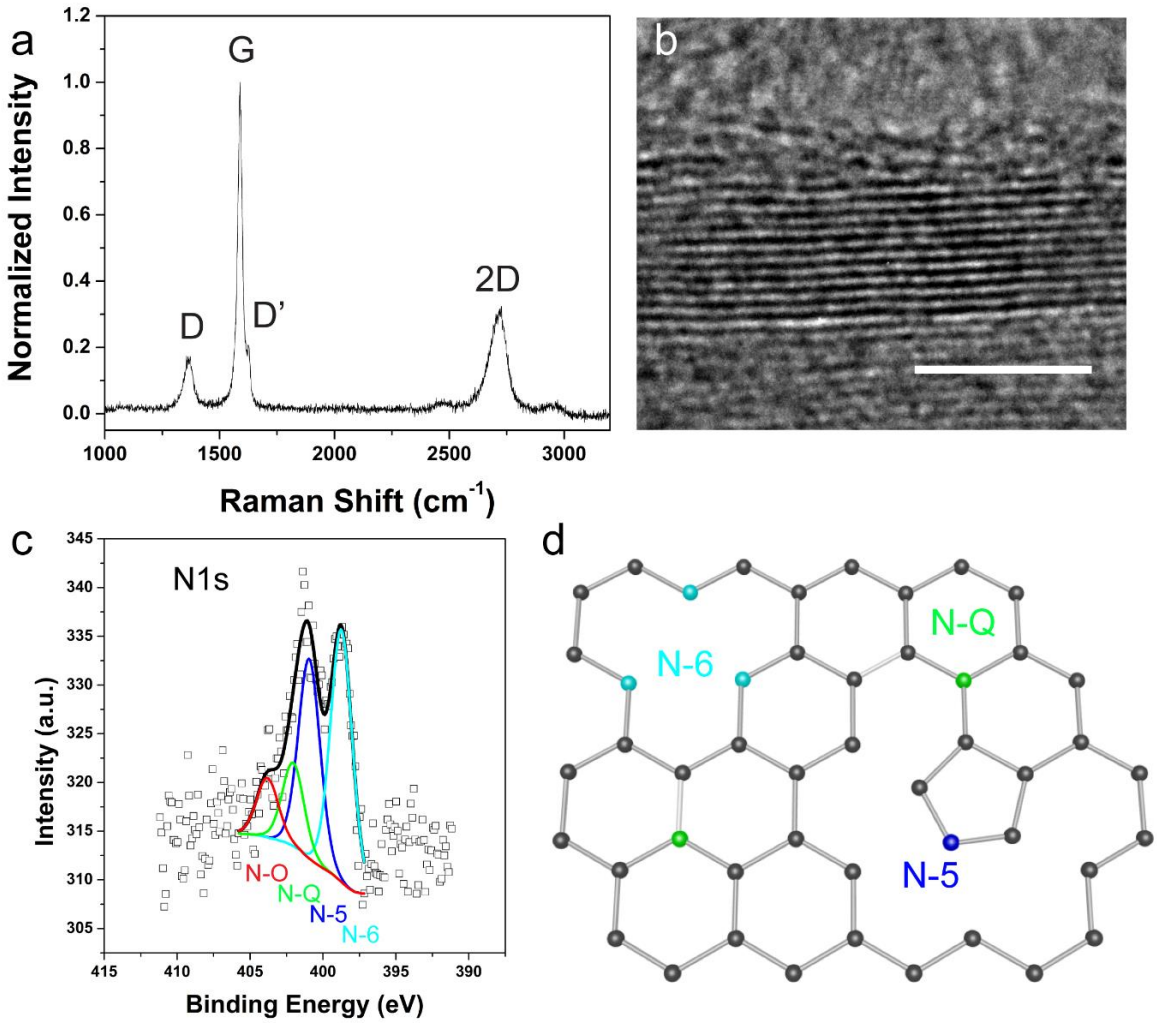

Figure 5.1 a) Raman spectra of nitrogen doped few layer graphene. b) TEM of nitrogen doped few layer graphene, scale bar = 5 nm. c) XPS data for the N1s spectra with 4 peaks from different nitrogen configurations in the lattice. d) Schematic for the different types of nitrogen defects in few layer graphene including graphitic nitrogen (N-Q), pyrrole-like nitrogen (N-5), and pyridine-like nitrogen (N-6). Reproduced from ref. [144] with permission from ACS

The G peak arises from in-plane sp^2 carbons while the D and D' are modes activated by the defects induced from N doping. In undoped samples the 2D/G ratio can be used to estimate the number of layers but the introduction of defects prevents such straightforward analysis in doped samples.[145] To assess this, TEM micrographs confirm the few-layer nature of N-FLG (Figure 5.1b) with generally 5-25 layers, similar to the number of layers in undoped FLG indicated by the 2D/G ratio and TEM (Figure 5.2a). X-ray photoelectron spectroscopy (XPS) was used to estimate the amount of nitrogen in N-FLG and to

determine the nitrogen bonding configurations in this material. Figure 5.2b displays the survey spectrum collected from the N-FLG, which contains no peaks from unexpected elements. Analysis of the XPS data determined the relative concentration of N to be approximately 2.2 at%. Four bonding configurations of the nitrogen were identified through deconvolution of the N1s spectrum (Figure 5.1c). Nitrogen with binding energies of 403.8 eV, 402.0 eV, 400.9 eV, and 398.7 eV were assigned to nitrogen-oxygen, graphitic nitrogen, pyrrolic nitrogen, and pyridinic nitrogen following the methodology of Kabir and coworkers.[142] Approximately 42.4% of the nitrogen is bonded as pyridinic nitrogen (N-6), 33.6% as pyrrolic nitrogen (N-5), 14% as graphitic nitrogen (N-Q), and 10% as N-O (Figure 5.1d).[146] Pyridinic N in particular can result in a local electron deficiency with a particularly high affinity for the electron from a nearby K atom. This can result in an increase in the number of ions stored in a given volume compared to undoped graphene.[147]

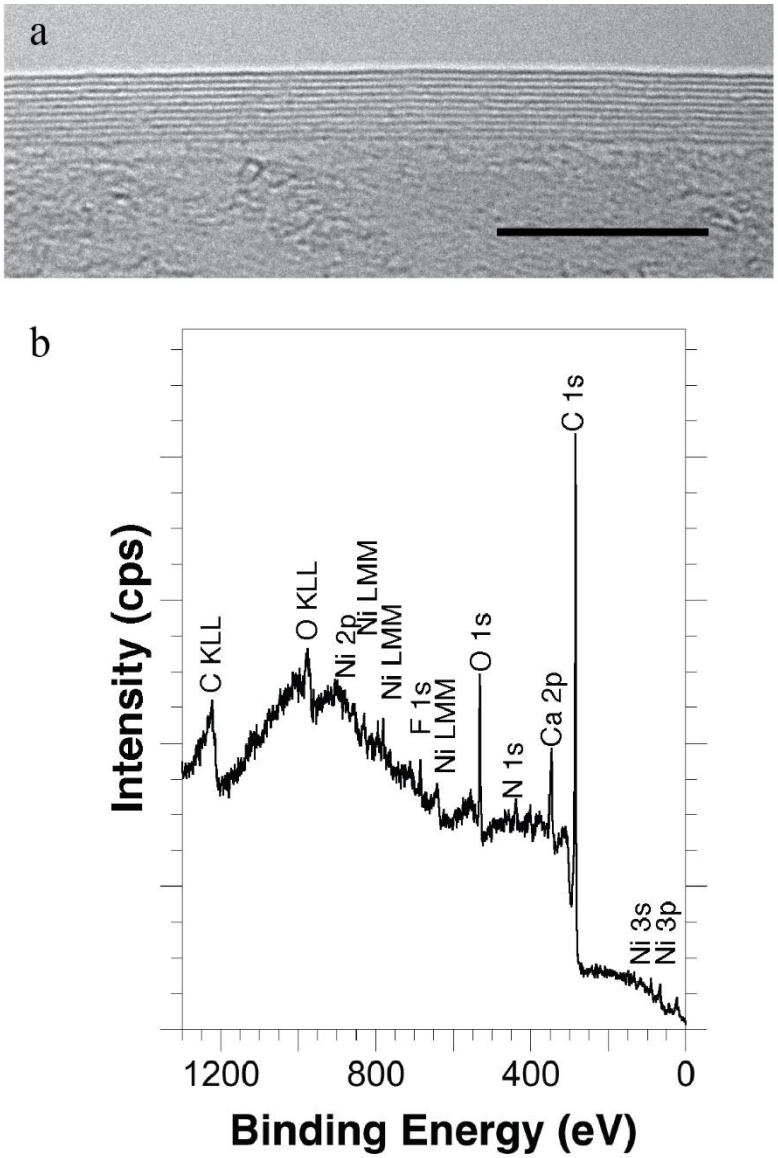

Figure 5.2 a) TEM micrograph of undoped FLG showing the few-layer structure, scale bar = 10 nm. b) XPS survey spectrum of nitrogen doped few layer graphene

5.4 Electrochemical Testing

To characterize the effect of N-FLG versus pristine FLG, electrochemical tests were carried out in a half-cell versus K/K^+ using CR2032 coin cells. Galvanostatic measurements were performed for five

cycles each at rates of 50, 100, and 200 mA/g (Figure 5.4) with charge-discharge profiles at 50 and 100 mA/g shown in Figure 5.3a and b respectively.

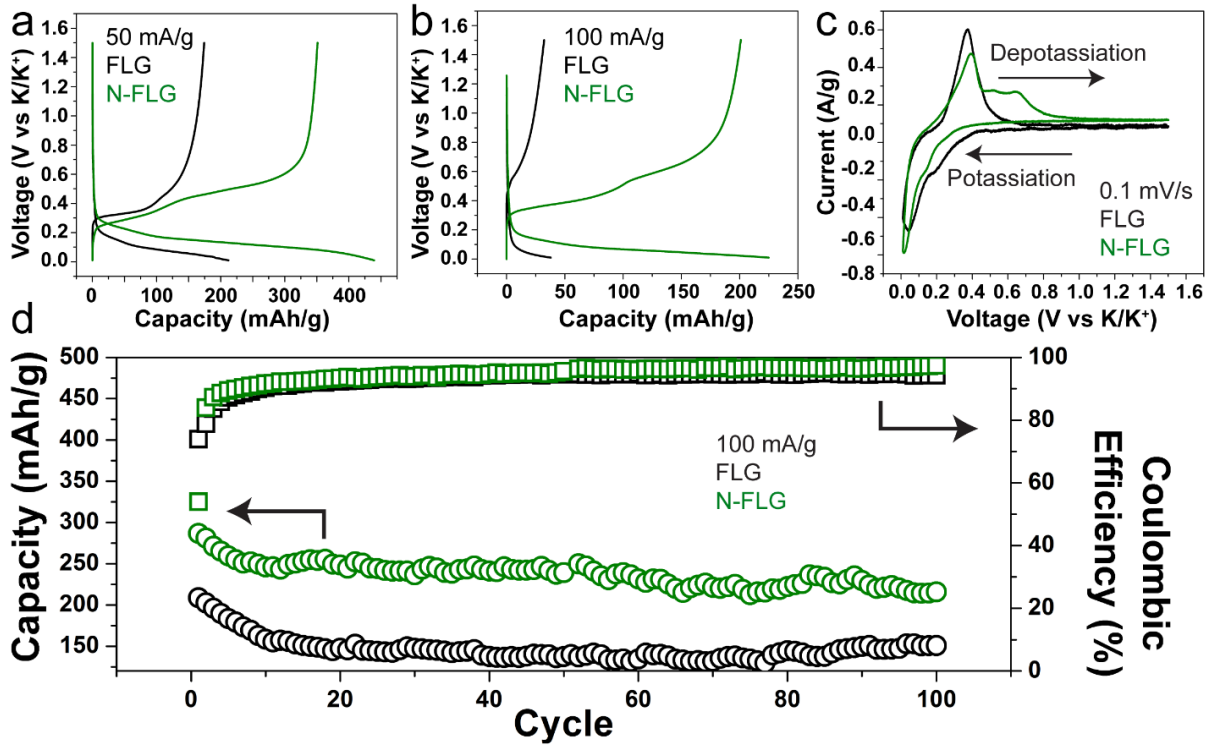

Figure 5.3 a) Galvanostatic charge-discharge curves at 50 mA/g for PIBs made from undoped and N doped few layer graphene. b) Galvanostatic charge-discharge curves at 100 mA/g c) Cyclic voltammetry at 0.1 mV/s for FLG and N-FLG d) Cycling at 100 mA/g for both FLG and N-FLG.

At rates of 50 mA/g, the initial anodic charge (depotassiation) capacity is around 350 mAh/g and remains constant over the five cycles measured at this rate. Notably, this is the highest capacity for a PIB carbon anode to date and well beyond the theoretical capacity of a stage I KC_8 GIC, approaching the theoretical Li capacity in graphite of 372 mAh/g. This is compared to the (undoped) FLG charge capacity of <200 mAh/g measured at the same rate. The capacities and charge-discharge profiles for FLG are very similar to those for graphite shown in literature.[39, 40] Galvanostatic testing at high rates up to 200 mA/g indicates capacities for the N-FLG that are over six times improved from FLG with capacity at 100 mA/g of ~200 mAh/g (N-FLG) versus ~30 mAh/g (FLG), and capacity at 200 mA/g of over 50 mAh/g (N-FLG)

versus < 5 mAh/g (FLG). This data elucidates key points that (1) N-FLG enables capacities evidently greater than that achievable in a stage I KC_8 GIC, and (2) the kinetics of K storage in N-FLG are faster than FLG. The charge-discharge curves for N-FLG in Figure 5.3a and b reveal an additional reaction plateau at higher voltages that accounts for a large amount of the increased capacity. The energetics associated with the improved K storage in N-FLG are further analyzed with cyclic voltammetry at 0.1 mV/s (Figure 5.3c). The general potassiation energetics appear to be similar in both FLG and N-FLG with small peaks around 0.18 V and larger peaks centered on 0.02 V vs. K/K^+. Although the potassiation energetics are similar, depotassiation reveals many new peaks in N-FLG not evident in FLG. Both samples exhibit a notable depotassiation peak near 0.35 V, but N-FLG further exhibits a series of additional peaks over the range of 0.4 V - 0.8 V, in agreement with the charge-discharge curves. As this emerges as the key difference in the energetics of N-FLG versus FLG K-ion storage, this is be attributed to the enhanced storage capacity observed.[122]

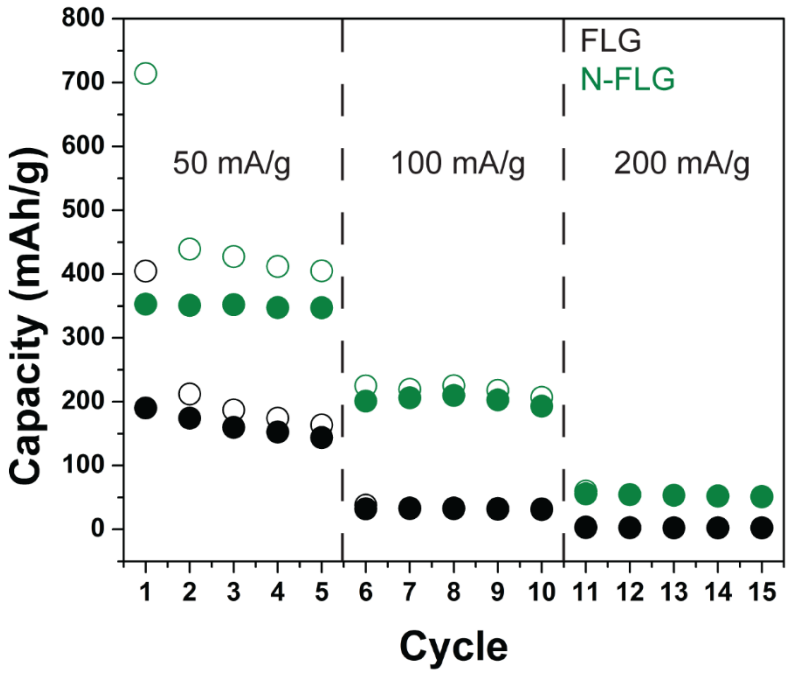

Figure 5.4 Galvanostatic rate study of N-FLG and FLG for five cycles at each rate of 50, 100, and 200 mA/g

Further studies of cycling performance for N-FLG compared to FLG (Figure 5.3d) at rates of 100 mA/g also indicates a stable, higher storage capacity for N-FLG compared to FLG. N-FLG initially starts with a capacity near 270 mAh/g and after 100 cycles remains above 210 mAh/g while FLG exhibits an initial capacity near 190 mAh/g and final capacity of only 150 mAh/g. The coulombic efficiency of N-FLG is consistently higher than FLG due to a more stable SEI and both improve over 50 cycles until steady values of 96.5% (N-FLG) and 94% (FLG) are reached.

5.5 Deconvoluting Carbon and Nitrogen Defects

At this point, one may enquire as to the origin of the observed enhancement from N-FLG being simply related to a sp^3 "defect" site in the carbon lattice or being correlated with the specific presence of N dopants in the graphitic carbon lattice. The D peak in the Raman spectrum of N-FLG (Figure 5.1a) can arise from both N defects and C sp^3 defects, and such C defects have been shown to improve storage for SIBs.[36] Ding et al investigated this C defect storage mechanism by producing carbon nanosheets with a range of D/G intensity ratios.[148] All samples displayed a combination of a nanopore filling mechanism and a pseudo graphitic reaction mechanism with Na^+. The ratio of these two mechanisms changed with D/G ratio, indicating that defective carbons contributed to the storage of Na^+. In order to determine how carbon defects affect K^+ storage defective undoped few layer graphene (d-FLG) was grown on Ni foam using acetylene. D-FLG contains sp^3 carbon defects but not N-doping, allowing for these two effects to be deconvoluted.

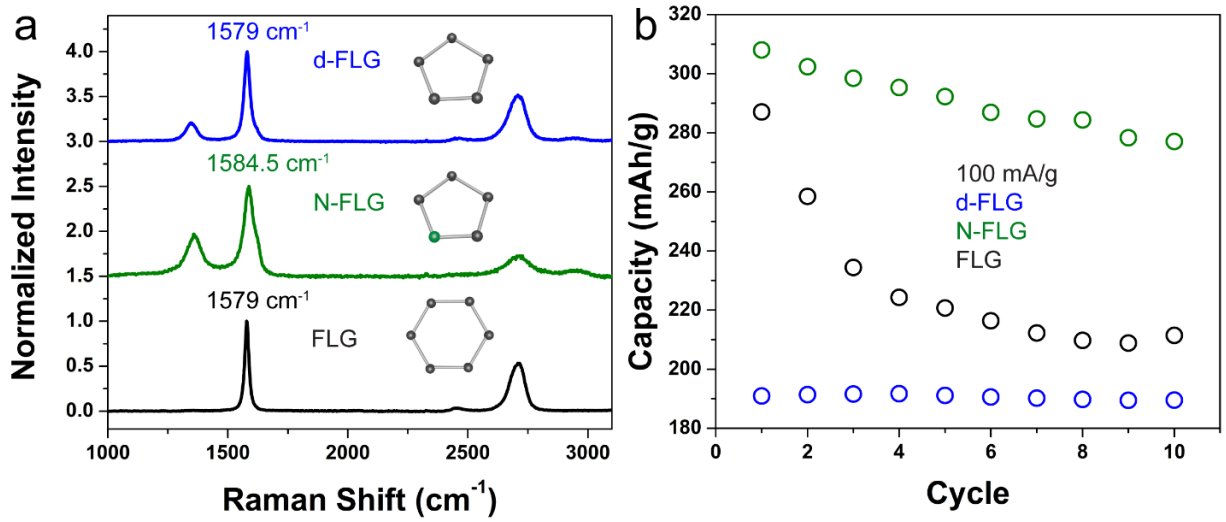

Figure 5.5 a) Raman spectra of defective, nitrogen doped, and undoped few layer graphene. b) Galvanostatic cycling at 100 mA/g for d-FLG, N-FLG, and FLG.

Representative Raman spectra of these three FLG materials (Figure 5.5a) indicate the distinctions in the relevant phonon modes that distinguish these materials. Both undoped samples have a G peak position near 1579 cm^{-1} while the N-FLG G peak is located at 1584.5 cm^{-1}. This peak is blue shifted in N-FLG due to the increased carrier concentration from doping.[123] Similarly, both the N-FLG and d-FLG exhibit a clear D peak compared to pristine FLG that exhibits no noticeable D peak. To address the role of sp^3 carbon sites versus N-doping sites on the electrochemical performance, galvanostatic testing at 100 mA/g rates was carried out (Figure 5.5b). This evidences that d-FLG exhibits a significantly compromised storage capacity in comparison to N-FLG and FLG. This provides an important distinction between K-ion and Na-ion storage in carbons, where Na-ion storage is mediated by defects in the absence of a stable GIC,[39, 149] while K-ion storage is compromised by the presence of carbon defects. This comparison emphasizes that N doping sites and *not* C defects are the source of improved capacities in N-FLG.

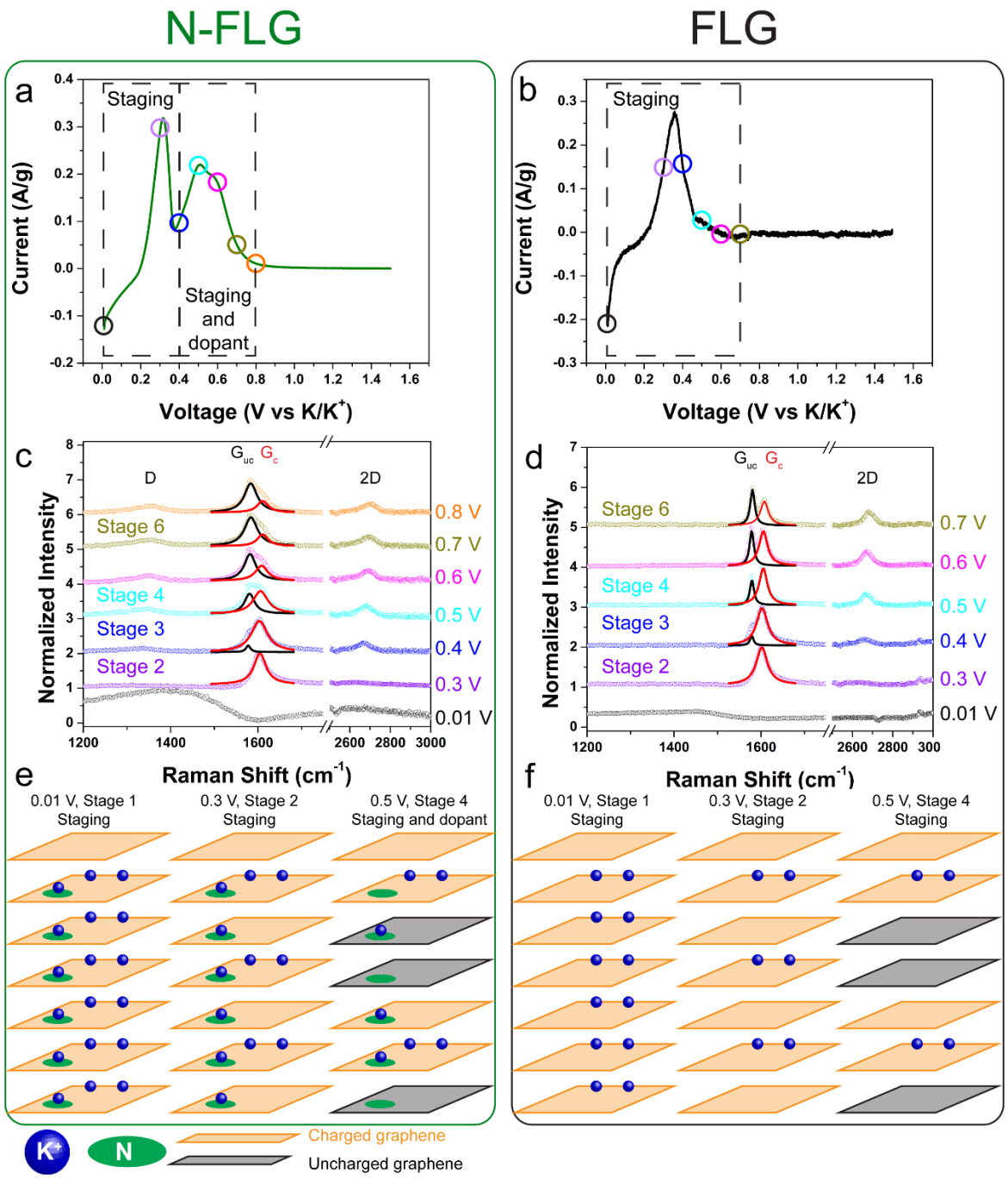

Figure 5.6 a, b) CVs at 0.05 mV/s for N-FLG and FLG respectively with indicators of the sampled voltages. c, d) Raman spectra at selected voltages for N-FLG (c) and FLG (d) with the color of the spectra corresponding to the colored circles in a, b. e, f) Schematic of the staging and defect storage mechanism in N-FLG (e) compared to traditional staging of FLG (f).

On the premise that the enhanced performance is correlated with N-doping sites, and not carbon defects, the mechanism for enhanced storage in N-FLG was further examined with *in-situ* Raman spectroscopy. *In-situ* Raman spectroscopy is a non-invasive technique for probing the electronic and structural changes in graphene and graphite and has been a powerful tool in efforts to establish a detailed understanding of Li^+ staging in carbons.[107, 114] In a staging process, the stage number refers to the number of graphene layers between intercalant layers. Graphene layers adjacent to intercalant layers become highly charged due to bonding between the ion and the graphene. This causes a blue shift of the uncharged G (G_{uc}) peak and produces the charged G (G_c) peak.[28] As staging progresses the peaks red shift and the intensity ratio of G_{uc}/G_c decreases which can be directly used to estimate the stage number.[106] To carry out *in-situ* Raman analysis, potentiostatic testing was used at different voltages, with an equilibration of 30 minutes at that voltage prior to collecting Raman spectra. Figure 5.6a, b show CV scans taken at 0.05 mV/s for N-FLG and FLG respectively over the voltage range used for *in-situ* testing. Spectra are shown in Figure 5.6c, d for N-FLG and FLG respectively, with line color corresponding to the circles in Figure 5.6a, b. Qualitatively, both samples have both G_c and G_{uc} peaks with the G_c peak decreasing in intensity and G_{uc} increasing in intensity as voltage increases. Therefore, staging can be readily assessed from the Raman spectra. At 0.01 V both samples exhibit an asymmetric Fano-resonance line shape arising due to interference between the metallic stage I compound and the phonon scattering process.[106] Both FLG and N-FLG are stage II at 0.3 V where all graphene layers are charged thus there is no G_{uc} or 2D peaks. From 0.3 to 0.7 V the Raman spectra for FLG and N-FLG are strikingly similar. Both the increasing G_{uc}/G_c intensity ratio and blue shifting peak positions follow the expected trends for a deintercalation process from a staged GIC (Figure 5.7).[106]

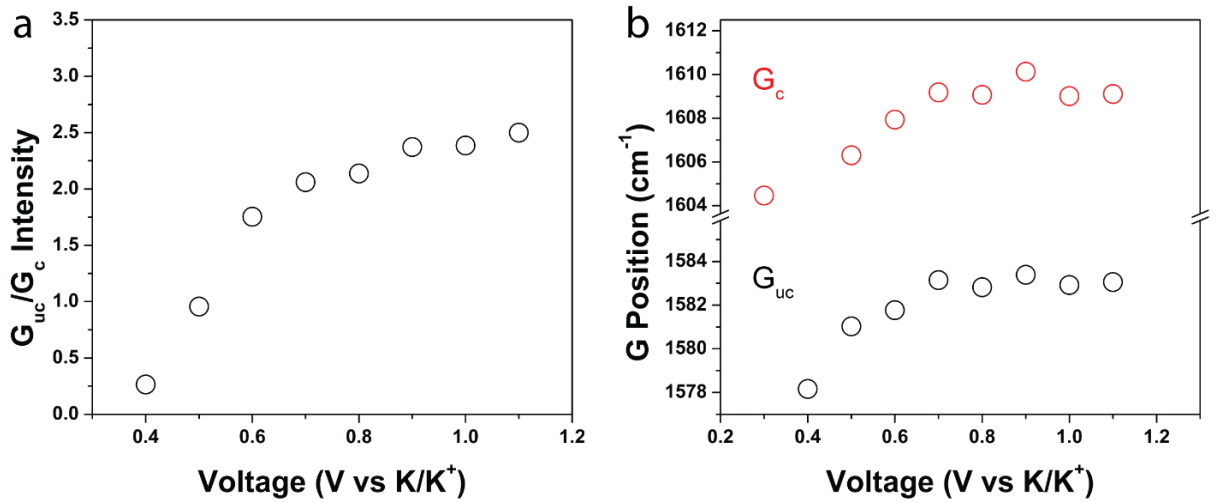

Figure 5.7 Peak fit data from the in-situ Raman testing for N-FLG. As expected during deintercalation, the G_{uc}/G_c intensity ratio (a) increases and both peaks blue shift (b).

By 0.4 V, the D peak (~1350 cm^{-1}) reemerges in N-FLG but no D peak appears in FLG through the entire voltage range (Figure 5.8). The higher order staging compounds evident from 0.4 V to 0.8 V (KC_{36} to KC_{72}) do not significantly contribute to the capacity of a battery and cannot explain the large peak in the N-FLG CV in that range. Therefore, the invariant staging sequence observed in N-FLG compared to FLG implies that N-sites do not incur a change in the staging properties of the graphitic carbon. This elucidates the role of N doping as providing sites distributed in the carbon matrix that can locally store K-ions in a manner that is not disruptive to the formation of a stage I GIC. Based on our electrochemical assessment, this is in contrast to the role of sp^3 carbon defect sites in d-FLG which compromise the capacity to levels significantly lower than that expected for a stage I GIC and hence inhibit the formation of a fully stage I GIC. A schematic representing the staging process and the role of N-doping sites in the graphitic carbon during staging is shown in Figure 5.6e, f.

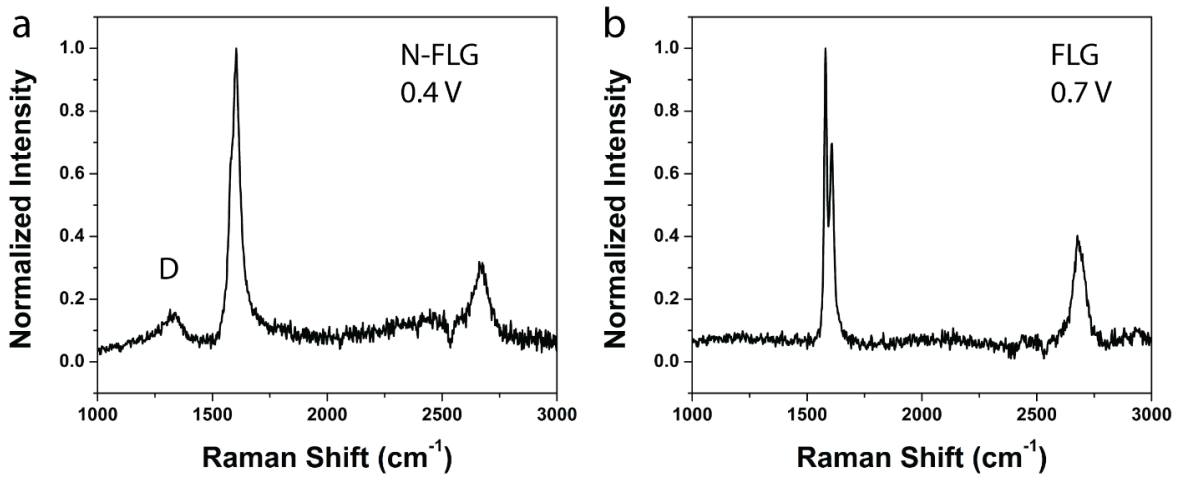

Figure 5.8 a) Raman spectra of N-FLG at 0.4 V showing the D peak. b) Even after depotassiation the Raman spectra of FLG does not show a D peak

5.7 Conclusion

Overall, the results that are presented in this study imply a key idea that atomically precise fabrication of materials can be a practical route to engineer the capacity of electrode materials for next-generation batteries. The ability to augment the storage capability of a GIC such as KC_8 with additional dopant-enabled storage sites that do not hinder the GIC storage capacity presents an exciting optimization challenge for both an experimental and theoretical researcher that stretches beyond the scope of our current study. Similar enhancements would be expected for dopants such as boron and phosphorus that can change the electronic band structure and increase localized reactivity.[150-152] Questions arise regarding the necessary relative location of dopant sites and the maximum density of dopant sites to reach the maximum possible storage capacity of an electrode material, which we observe is > 350 mAh/g for K-ion storage in N-FLG.

In summary, N-FLG has been shown in this work to overcome the limitation of K-ion storage in graphitic carbons (FLG) and exhibit storage capacity greater than 350 mAh/g – the highest reported PIB anode capacity thus far. Our results reveal this enhanced capacity to be specifically associated with N-doping sites, as undoped defective FLG leads to compromised capacity compared to crystalline FLG.

Electrochemical data combined with *in-situ* Raman spectroscopy present a mechanistic role of N-doping to simultaneously activate distributed storage sites in the carbon lattice while sustaining the energetic pathway for the formation of a stage I GIC (KC_8). This study presents an advance that can enable graphitic carbons to be an anode for potassium ion batteries with storage capability matching that of lithium ion battery anodes. This is one of many critical steps needed to address the need for lower cost rechargeable energy storage in a manner synergistic with the current state of battery manufacturing technology.

Chapter 6 Conclusion

The chapters contained in this dissertation aim to tackle the biggest challenges in the field of sodium ion batteries, potassium ion batteries, and desalination batteries. Through the application of electrochemical testing, ex-situ, and in-situ spectroscopy, I provided solutions and mechanistic understanding to advance each of these fields.

In chapter two, my goal was to solve the lack of sodium intercalation into graphite by using WSe_2 an alternative layered material. I was the first to demonstrate WSe_2 as an efficient electrode for sodium ion batteries. A high reversible capacity above 200 mAh/g was observed at 20 mA/g rate, with over 250 mAh/g capacity measured in the first sodium extraction. Assessment of electrolyte and binder materials on performance was examined and an EC/DEC electrolyte with CMC binder emerged to yield the highest capacity and cycling retention. Comparison between WS_2 and WSe_2 distinguished $WSe_2$to exhibit superior performance due to more efficient energetics bearing a small overpotential < 0.30 V. Ex-situ analysis and imaging after cycling confirmed a sodium-mediated conversion reaction that yielded isolated domains of W metal or Na_xSe and reformation of WSe_2 upon sodium extraction, enabling insight into the chemical storage pathway. This work highlighted the promise of WSe_2 comparted to other conversion-based transition metal dichalcogenides as a practical material for sodium ion batteries.

In chapter three, I focused on controlling the energy intensive process of Faradaic removal of chloride ions from salt water. I showed that smaller Ag nanoparticles lead to thinner AgCl layers, shorter diffusion lengths, reduced ionic and electronic resistances, and improved kinetics. During the removal of 53 mg Cl^-/g Ag, 25 nm Ag nanoparticles consume 30-40% less energy than 326 nm particles, requiring 0.09 Wh/L and 0.26 Wh/L at 0.25 A/g and 2.5 A/g respectively. Electrochemical testing revealed the kinetic and resistive limitations are particularly prevalent during the reduction of AgCl back to Ag. These findings revealed how nanostructures can be engineered to control the energetics and kinetics of electrochemical reactions.

In chapter four, I delved into potassium ion batteries and leveraged the strong Raman spectroscopic response of few-layered graphene to provide the first in-situ insight into the electrochemical staging sequence for K^+ ions in graphitic carbons. My analysis revealed the signature of a dilute stage I compound that precedes formation of ordered intercalation compounds transitioning from stage VI (KC_{72}), stage II (KC_{24}), and stage I (KC_8) and correlated electrochemical responses to the stage formation. Overall, my study emphasized a minimum barrier to transfer the general understanding acquired for lithium-ion battery anodes to cheaper, earth abundant K-ion battery systems ideally suited for grid-scale storage.

Finally, in chapter five, my goal was to break the barrier of the theoretical capacity of K^+ in graphite of 278 mAh/g and produce capacities on par with Li^+ storage in graphite. I demonstrated that nitrogen doping of few-layered graphene can increase the storage capacity of potassium to over 350 mAh/g, the highest reported anode capacity so far for PIBs. Control studies distinguished the importance of nitrogen dopant sites as opposed to sp^3 carbon defect sites to achieve the improved performance, which also enabled greater than 6 times increase in rate performance of doped vs undoped materials. Finally, in-situ Raman spectroscopy studies elucidated the staging sequence for doped and undoped materials and demonstrated the mechanism of the observed capacity enhancement to be correlated with distributed storage at local nitrogen sites in a staged KC_8 compound. This study demonstrated a pathway to overcome the limitations of graphic carbons for anodes in potassium ion batteries by atomically precise engineering of nanomaterials. Further improvement could be achieved through controlling the type and number of N dopants.

I hope that others are able to use what I have learned from these projects to advance these fields even further. One of the most rewarding experiences in graduate school has been to see the works published by others that build upon my research to provide additional understanding and improvement.

REFERENCES

1. Bleich, K. G., Rafael Dantas, Renewable Infrastructure: Investment Handbook: A Guide for Institutional Investors. World Economic Forum. 2016.

2. Wesoff, E. Rick Perry, Governor of Largest Wind State, Is Trump's Pick for Head of DOE. https://www.greentechmedia.com/articles/read/rick-perry-governor-of-largest-wind-power-state-is-trumps-pick-for-head-of#gs.mAt2RTQ

3. American Wind Energy Assocation. Wind Energy in Texas. http://awea.files.cms-plus.com/FileDownloads/pdfs/Texas.pdf

4. Department of Energy. U.S. Energy and Employment Report. Jan. 2017.

5. Lew, D.; Bird, L.; Milligan, M.; Speer, B.; Wang, X.; Carlini, E. M.; Estanqueiro, A.; Flynn, D.; Gomez-Lazaro, E.; Menemenlis, N. In *Wind and solar curtailment*, International Workshop on Large-Scale Integration of Wind Power Into Power Systems, 2013.

6. Curtright, A. E.; Apt, J. *Prog. Photo.* **2008,** 16, (3), 241-247.

7. Hoare, K. Solar Power Self-Consumption - The Facts. https://www.mysolarquotes.co.nz/blog/how-it-works/solar-power-self-consumption---the-facts-

8. Curry, C. Lithium-Ion Battery Costs and Market.

9. Perkowski, J. How China is Raising the Bar with Aggressive New Electric Vehicle Rules. https://www.forbes.com/sites/jackperkowski/2017/10/10/china-raises-the-bar-with-new-electric-vehicle-rules/#6425c40977ac

10. Karabasoglu, O.; Michalek, J. *Energy Policy* **2013,** 60, 445-461.

11. Tarascon, J.-M.; Armand, M. *Nature* **2001,** 414, (6861), 359-367.

12. Whittingham, M. S. *Science* **1976,** 192, (4244), 1126-1127.

13. Myung, S.-T.; Maglia, F.; Park, K.-J.; Yoon, C. S.; Lamp, P.; Kim, S.-J.; Sun, Y.-K. *ACS Energy Lett.* **2016,** 2, (1), 196-223.

14. Jessica Shankleman, T. B., Joe Ryan, and Dave Merrill We're Going to Need More Lithium. https://www.bloomberg.com/graphics/2017-lithium-battery-future/

15. Margulescu, S.; Margulescu, E. *Global Economic Observer* **2016,** 4, (2), 117.

16. Global Market Insights. Lithium Ion Battery Market Worth Over $60 billion by 2024. https://globenewswire.com/news-release/2017/12/14/1261852/0/en/Lithium-Ion-Battery-Market-worth-over-60-billion-By-2024-Global-Market-Insights-Inc.html

17. Palomares, V.; Casas-Cabanas, M.; Castillo-Martínez, E.; Han, M. H.; Rojo, T. *Energy Environ. Sci.* **2013,** 6, (8), 2312-2337.

18. Slater, M. D.; Kim, D.; Lee, E.; Johnson, C. S. *Adv. Func. Mater.* **2013,** 23, (8), 947-958.

19. Liu, Y.; Fan, F.; Wang, J.; Liu, Y.; Chen, H.; Jungjohann, K. L.; Xu, Y.; Zhu, Y.; Bigio, D.; Zhu, T. *Nano Lett.* **2014,** 14, (6), 3445-3452.

20. Komaba, S.; Hasegawa, T.; Dahbi, M.; Kubota, K. *Electrochem. Comm.* **2015,** 60, 172-175.

21. Xing, Z.; Jian, Z.; Luo, W.; Qi, Y.; Bommier, C.; Chong, E. S.; Li, Z.; Hu, L.; Ji, X. *Energy Storage Mater.* **2016,** 2, 63-68.

22. Jian, Z.; Xing, Z.; Bommier, C.; Li, Z.; Ji, X. *Adv. Energy Mater.* **2015,** 6, 1501874-1501878.

23. Lin, M.-C.; Gong, M.; Lu, B.; Wu, Y.; Wang, D.-Y.; Guan, M.; Angell, M.; Chen, C.; Yang, J.; Hwang, B.-J. *Nature* **2015,** 520, (7547), 324-328.

24. Chihara, K.; Katogi, A.; Kubota, K.; Komaba, S. *Chem. Comm.* **2017,** 53, (37), 5208-5211.

25. Palomares, V.; Serras, P.; Villaluenga, I.; Hueso, K. B.; Carretero-González, J.; Rojo, T. *Energy Environ. Sci.* **2012,** 5, (3), 5884-5901.

26. Ge, P.; Fouletier, M. *Solid State Ion.* **1988,** 28, 1172-1175.

27. Doeff, M. M.; Ma, Y.; Visco, S. J.; De Jonghe, L. C. *J. Electrochem. Soc.* **1993,** 140, (12), L169-L170.

28. Dresselhaus, M.; Dresselhaus, G. *Adv. Phys.* **1981,** 30, (2), 139-326.

29. Luo, W.; Wan, J.; Ozdemir, B.; Bao, W.; Chen, Y.; Dai, J.; Lin, H.; Xu, Y.; Gu, F.; Barone, V. *Nano letters* **2015,** 15, (11), 7671-7677.

30. Jayaprakash, N.; Das, S. K.; Archer, L. A. *Chem. Comm.* **2011,** 47, (47), 12610-12612.

31. Liu, Y.; Merinov, B. V.; Goddard, W. A. *Proc. Natl. Acad. Sci.* **2016,** 113, (14), 3735-3739.

32. Komaba, S.; Murata, W.; Ishikawa, T.; Yabuuchi, N.; Ozeki, T.; Nakayama, T.; Ogata, A.; Gotoh, K.; Fujiwara, K. *Adv. Func. Mater.* **2011,** 21, (20), 3859-3867.

33. Li, Y.; Liang, Y.; Hernandez, F. C. R.; Yoo, H. D.; An, Q.; Yao, Y. *Nano Energy* **2015,** 15, 453-461.

34. Bang, G. S.; Nam, K. W.; Kim, J. Y.; Shin, J.; Choi, J. W.; Choi, S.-Y. *ACS Appl. Maters. Interfaces* **2014,** 6, (10), 7084-7089.

35. Qie, L.; Chen, W.; Xiong, X.; Hu, C.; Zou, F.; Hu, P.; Huang, Y. *Adv. Sci.* **2015,** 2, (12).

36. Bommier, C.; Surta, T. W.; Dolgos, M.; Ji, X. *Nano Lett.* **2015,** 15, (9), 5888-5892.

37. Vaalma, C.; Buchholz, D.; Passerini, S. *Curr. Opin. Electrochem.* **2018**.

38. Wang, H.; Yang, Y.; Liang, Y.; Robinson, J. T.; Li, Y.; Jackson, A.; Cui, Y.; Dai, H. *Nano Lett.* **2011,** 11, (7), 2644-2647.

39. Jian, Z.; Luo, W.; Ji, X. *J. Am. Chem. Soc.* **2015,** 137, (36), 11566-11569.

40. Luo, W.; Wan, J.; Ozdemir, B.; Bao, W.; Chen, Y.; Dai, J.; Lin, H.; Xu, Y.; Gu, F.; Barone, V.; Hu, L. *Nano Lett.* **2015,** 15, (11), 7671-7677.

41. Elimelech, M.; Phillip, W. A. *Science* **2011,** 333, (6043), 712-717.

42. Cheslow, D., Every Day Seems Like 'Day Zero' to Some Cape Town Residents. *NPR* March 13, 2018.

43. Anderson, M. A.; Cudero, A. L.; Palma, J. *Electrochim. Acta* **2010,** 55, (12), 3845-3856.

44. Amy, G.; Ghaffour, N.; Li, Z.; Francis, L.; Linares, R. V.; Missimer, T.; Lattemann, S. *Desal.* **2017,** 401, 16-21.

45. Suss, M.; Porada, S.; Sun, X.; Biesheuvel, P.; Yoon, J.; Presser, V. *Energy Environ. Sci.* **2015,** 8, (8), 2296-2319.

46. Oren, Y. *Desal.* **2008,** 228, (1-3), 10-29.

47. Suss, M. E.; Presser, V. *Joule* **2018,** 2, (1), 10-15.

48. Pasta, M.; Wessells, C. D.; Cui, Y.; La Mantia, F. *Nano Lett.* **2012,** 12, (2), 839-843.

49. Chen, F.; Huang, Y.; Kong, D.; Ding, M.; Huang, S.; Yang, H. Y. *FlatChem* **2018**.

50. Zhou, F.; Gao, T.; Luo, M.; Li, H. *Sep. Pur. Technol.* **2018,** 191, 322-327.

51. Lee, J.; Kim, S.; Yoon, J. *ACS Omega* **2017,** 2, (4), 1653-1659.

52. Erinmwingbovo, C.; Palagonia, M. S.; Brogioli, D.; La Mantia, F. *ChemPhysChem* **2017,** 18, (8), 917-925.

53. Guo, L.; Mo, R.; Shi, W.; Huang, Y.; Leong, Z. Y.; Ding, M.; Chen, F.; Yang, H. Y. *Nanoscale* **2017,** 9, (35), 13305-13312.

54. Porada, S.; Shrivastava, A.; Bukowska, P.; Biesheuvel, P.; Smith, K. C. *Electrochim. Acta* **2017,** 255, 369-378.

55. Zhao, X.; Ren, S.; Bruns, M.; Fichtner, M. *J. Power Sources* **2014,** 245, 706-711.

56. Chen, F.; Leong, Z. Y.; Yang, H. Y. *Energy Storage Mater.* **2017,** 7, 189-194.

57. Kim, K.; Hwang, S. M.; Park, J.-S.; Han, J.; Kim, J.; Kim, Y. *J. Power Sources* **2016,** 313, 46-50.

58. Chen, F.; Huang, Y.; Guo, L.; Ding, M.; Yang, H. Y. *Nanoscale* **2017,** 9, (28), 10101-10108.

59. Nanda, K.; Maisels, A.; Kruis, F.; Fissan, H.; Stappert, S. *Phys. Rev. Lett.* **2003,** 91, (10), 106102.

60. Gribb, A. A.; Banfield, J. F. *Am. Mineral.* **1997,** 82, (7-8), 717-728.

61. Ivanova, O. S.; Zamborini, F. P. *J. Am. Chem. Soc.* **2009,** 132, (1), 70-72.

62. Mabbott, G. A. *J. Chem. Educ.* **1983,** 60, (9), 697.

63. Elgrishi, N. M.; Rountree, K. J.; Mccarthy, B. D.; Rountree, E. S.; Eisenhart, T. T.; Dempsey, J. L. *J. Chem. Educ.* **2017**.

64. Liu, H.; Su, D.; Wang, G.; Qiao, S. Z. *J. Mater. Chem.* **2012,** 22, (34), 17437-17440.

65. Park, J.; Kim, J.-S.; Park, J.-W.; Nam, T.-H.; Kim, K.-W.; Ahn, J.-H.; Wang, G.; Ahn, H.-J. *Electrochim. Acta* **2013,** 92, 427-432.

66. Liu, B.; Luo, T.; Mu, G.; Wang, X.; Chen, D.; Shen, G. *ACS Nano* **2013,** 7, (9), 8051-8058.

67. Zhang, S.; Yu, X.; Yu, H.; Chen, Y.; Gao, P.; Li, C.; Zhu, C. *ACS Appl. Maters. Interfaces* **2014,** 6, (24), 21880-21885.

68. Wang, Y.-X.; Seng, K. H.; Chou, S.-L.; Wang, J.-Z.; Guo, Z.; Wexler, D.; Liu, H.-K.; Dou, S.-X. *Chem. Comm.* **2014,** 50, (73), 10730-10733.

69. Lacey, S. D.; Wan, J.; Cresce, A. V. W.; Russell, S. M.; Dai, J.; Bao, W.; Xu, K.; Hu, L. *Nano Lett.* **2015,** 15, (2), 1018-1024.

70. Wang, X.; Shen, X.; Wang, Z.; Yu, R.; Chen, L. *ACS Nano* **2014,** 8, (11), 11394-11400.

71. Chia, X.; Ambrosi, A.; Sofer, Z.; Luxa, J.; Pumera, M. *ACS Nano* **2015**.

72. Ko, Y. N.; Choi, S. H.; Park, S. B.; Kang, Y. C. *Nanoscale* **2014,** 6, (18), 10511-10515.

73. Wang, H.; Lan, X.; Jiang, D.; Zhang, Y.; Zhong, H.; Zhang, Z.; Jiang, Y. *J. Power Sources* **2015,** 283, 187-194.

74. Su, D.; Dou, S.; Wang, G. *Chem. Comm.* **2014,** 50, (32), 4192-4195.

75. Share, K.; Lewis, J.; Oakes, L.; Carter, R. E.; Cohn, A. P.; Pint, C. L. *RSC Adv.* **2015,** 5, (123), 101262-101267.

76. Vogt, L. O.; El Kazzi, M.; JäMstorp Berg, E.; PéRez Villar, S. A.; Novák, P.; Villevieille, C. *Chem. Mater.* **2015,** 27, (4), 1210-1216.

77. Muñoz-Márquez, M. A.; Zarrabeitia, M.; Castillo-Martinez, E.; Eguía-Barrio, A.; Rojo, T.; Casas-Cabanas, M. *ACS Appl. Maters. Interfaces* **2015**.

78. Wang, X.; Li, Y.; Guan, Z.; Wang, Z.; Chen, L. *Chem. Eur. J.* **2015,** 21, (17), 6465-6468.

79. Jache, B.; Adelhelm, P. *Angew. Chem. Int. Ed.* **2014,** 53, (38), 10169-10173.

80. Sahin, H.; Tongay, S.; Horzum, S.; Fan, W.; Zhou, J.; Li, J.; Wu, J.; Peeters, F. *Phys. Rev. B* **2013,** 87, (16), 165409.

81. Herwig, C.; Schnell, M.; Becker, J. *Chem. Phys. Lett.* **2004,** 385, (5), 462-466.

82. Lucovsky, G.; Mooradian, A.; Taylor, W.; Wright, G.; Keezer, R. *Solid State Commun.* **1967,** 5, (2), 113-117.

83. Mcdowell, M. T.; Lu, Z.; Koski, K. J.; Yu, J. H.; Zheng, G.; Cui, Y. *Nano Lett.* **2015,** 15, (2), 1264-1271.

84. Chhowalla, M.; Shin, H. S.; Eda, G.; Li, L.-J.; Loh, K. P.; Zhang, H. *Nat. Chem.* **2013,** 5, (4), 263-275.

85. Xu, M.; Yi, F.; Niu, Y.; Xie, J.; Hou, J.; Liu, S.; Hu, W.; Li, Y.; Li, C. M. *J. Mater. Chem. A* **2015,** 3, (18), 9932-9937.

86. Ryu, W.-H.; Jung, J.-W.; Park, K.; Kim, S.-J.; Kim, I.-D. *Nanoscale* **2014,** 6, (19), 10975-10981.

87. Ahmed, B.; Anjum, D. H.; Hedhili, M. N.; Alshareef, H. N. *Small* **2015**.

88. Wang, J.; Luo, C.; Gao, T.; Langrock, A.; Mignerey, A. C.; Wang, C. *Small* **2014**.

89. David, L.; Bhandavat, R.; Singh, G. *ACS Nano* **2014,** 8, (2), 1759-1770.

90. Xie, X.; Ao, Z.; Su, D.; Zhang, J.; Wang, G. *Adv. Func. Mater.* **2015**.

91. Nam, D.-H.; Choi, K.-S. *J. Am. Chem. Soc.* **2017,** 139, (32), 11055-11063.

92. Kim, T.; Gorski, C. A.; Logan, B. E. *Environ. Sci. Technol. Lett.* **2017,** 4, (10), 444-449.

93. Porada, S.; Bukowska, P.; Shrivastava, A.; Biesheuvel, P.; Smith, K. C. *arXiv preprint arXiv:1612.08293* **2016**.

94. Kim, D.; Jeong, S.; Moon, J. *Nanotech.* **2006,** 17, (16), 4019.

95. Jelić, D.; Penavin-Škundrić, J.; Majstorović, D.; Mentus, S. *Thermochim. Acta* **2011,** 526, (1-2), 252-256.

96. Moon, K.-S.; Dong, H.; Maric, R.; Pothukuchi, S.; Hunt, A.; Li, Y.; Wong, C. *J. Electronic. Mater.* **2005,** 34, (2), 168-175.

97. Cai, W.; Zhong, H.; Zhang, L. *J. Appl. Phys.* **1998,** 83, (3), 1705-1710.

98. Nicholson, R. S. *Anal. Chem.* **1965,** 37, (11), 1351-1355.

99. Bard, A. J.; Faulkner, L. R.; Leddy, J.; Zoski, C. G., *Electrochemical Methods: Fundamentals and Applications*. Wiley New York: 1980; Vol. 2.

100. Jin, X.; Lu, J.; Liu, P.; Tong, H. *J. Electroanal. Chem.* **2003,** 542, 85-96.

101. Zhu, Y.; Wang, C. *J. Power Sources* **2011,** 196, (3), 1442-1448.

102. Bardhan, R.; Hedges, L. O.; Pint, C. L.; Javey, A.; Whitelam, S.; Urban, J. J. *Nat. Mater.* **2013,** 12, (10), 905.

103. Saravanan, K.; Mason, C. W.; Rudola, A.; Wong, K. H.; Balaya, P. *Adv. Energy Mater.* **2013,** 3, (4), 444-450.

104. Ha, H.; Payer, J. *Electrochim. Acta* **2011,** 56, (7), 2781-2791.

105. Zhang, L.; Wang, Z.; Mehio, N.; Jin, X.; Dai, S. *ChemSusChem* **2016,** 9, (5), 428-432.

106. Chacon-Torres, J. C.; Wirtz, L.; Pichler, T. *ACS Nano* **2013,** 7, (10), 9249-9259.

107. Inaba, M.; Yoshida, H.; Ogumi, Z.; Abe, T.; Mizutani, Y.; Asano, M. *J. Electrochem. Soc.* **1995,** 142, (1), 20-26.

108. Lerf, A. *Dalton Trans.* **2014,** 43, (27), 10276-10291.

109. Daumas, N.; Herold, A. *C.R. Acad. Sci., Ser. IIc: Chim* **1969**, (286), 373.

110. Ferrari, A. C.; Basko, D. M. *Nat. Nanotechnol.* **2013,** 8, (4), 235.

111. Dresselhaus, M. S.; Jorio, A.; Hofmann, M.; Dresselhaus, G.; Saito, R. *Nano Lett.* **2010,** 10, (3), 751-758.

112. Rao, R.; Liptak, D.; Cherukuri, T.; Yakobson, B. I.; Maruyama, B. *Nat. Mater.* **2012,** 11, (3), 213.

113. Rao, R.; Pierce, N.; Liptak, D.; Hooper, D.; Sargent, G.; Semiatin, S. L.; Curtarolo, S.; Harutyunyan, A. R.; Maruyama, B. *ACS Nano* **2013,** 7, (2), 1100-1107.

114. Sole, C.; Drewett, N. E.; Hardwick, L. J. *Faraday Discuss.* **2014,** 172, 223-237.

115. Huang, W.; Frech, R. *J. Electrochem. Soc.* **1998,** 145, (3), 765-770.

116. Ferrari, A. C.; Meyer, J.; Scardaci, V.; Casiraghi, C.; Lazzeri, M.; Mauri, F.; Piscanec, S.; Jiang, D.; Novoselov, K.; Roth, S. *Phys. Rev. Lett.* **2006,** 97, (18), 187401.

117. Shi, Q.; Dokko, K.; Scherson, D. A. *J. Phys. Chem. B* **2004,** 108, (15), 4789-4793.

118. Baddour-Hadjean, R.; Pereira-Ramos, J.-P. *Chem. Rev.* **2009,** 110, (3), 1278-1319.

119. Das, A.; Pisana, S.; Chakraborty, B.; Piscanec, S.; Saha, S.; Waghmare, U.; Novoselov, K.; Krishnamurthy, H.; Geim, A.; Ferrari, A. *Nat. Nanotechnol.* **2008,** 3, (4), nnano. 2008.67.

120. Cohn, A. P.; Share, K.; Carter, R.; Oakes, L.; Pint, C. L. *Nano Lett.* **2015,** 16, (1), 543-548.

121. Malard, L.; Pimenta, M.; Dresselhaus, G.; Dresselhaus, M. *Phys. Rep.* **2009,** 473, (5), 51-87.

122. Share, K.; Cohn, A. P.; Carter, R. E.; Pint, C. L. *Nanoscale* **2016,** 8, (36), 16435-16439.

123. Pisana, S.; Lazzeri, M.; Casiraghi, C.; Novoselov, K. S.; Geim, A. K.; Ferrari, A. C.; Mauri, F. *Nat. Mater.* **2007,** 6, (3), 198-201.

124. Malard, L.; Elias, D.; Alves, E.; Pimenta, M. *Phys. Rev. Lett.* **2008,** 101, (25), 257401.

125. Das, A.; Pisana, S.; Chakraborty, B.; Piscanec, S.; Saha, S.; Waghmare, U.; Novoselov, K.; Krishnamurthy, H.; Geim, A.; Ferrari, A. *Nat. Nanotech.* **2008,** 3, (4), 210-215.

126. Chen, C.-F.; Park, C.-H.; Boudouris, B. W.; Horng, J.; Geng, B.; Girit, C.; Zettl, A.; Crommie, M. F.; Segalman, R. A.; Louie, S. G. *Nature* **2011,** 471, (7340), 617-620.

127. Nemanich, R. J.; Solin, S.; Guerard, D. *Phys. Rev. B* **1977,** 16, (6), 2965.

128. Nixon, D.; Parry, G. *J. Phys. C* **1969,** 2, (10), 1732.

129. Nishitani, R.; Uno, Y.; Suematsu, H. *Phys. Rev. B* **1983,** 27, (10), 6572.

130. Eklund, P.; Dresselhaus, G.; Dresselhaus, M.; Fischer, J. *Phys. Rev. B* **1977,** 16, (8), 3330.

131. Mathew, V.; Kim, S.; Kang, J.; Gim, J.; Song, J.; Baboo, J. P.; Park, W.; Ahn, D.; Han, J.; Gu, L. *NPG Asia Mater.* **2014,** 6, (10), e138.

132. Jian, Z.; Liang, Y.; Pérez, I. a. R.; Yao, Y.; Ji, X. *Electrochem. Comm.* **2016,** 71, 5-8.

133. Wu, Z.-S.; Ren, W.; Xu, L.; Li, F.; Cheng, H.-M. *ACS Nano* **2011,** 5, (7), 5463-5471.

134. Wu, Z. S.; Winter, A.; Chen, L.; Sun, Y.; Turchanin, A.; Feng, X.; Müllen, K. *Adv. Mater.* **2012,** 24, (37), 5130-5135.

135. Wang, H.; Maiyalagan, T.; Wang, X. *ACS Catal.* **2012,** 2, (5), 781-794.

136. Wang, H.; Zhang, C.; Liu, Z.; Wang, L.; Han, P.; Xu, H.; Zhang, K.; Dong, S.; Yao, J.; Cui, G. *J. Mater. Chem.* **2011,** 21, (14), 5430-5434.

137. Cho, Y. J.; Kim, H. S.; Im, H.; Myung, Y.; Jung, G. B.; Lee, C. W.; Park, J.; Park, M.-H.; Cho, J.; Kang, H. S. *J. Phys. Chem. C* **2011,** 115, (19), 9451-9457.

138. Wang, Z.; Qie, L.; Yuan, L.; Zhang, W.; Hu, X.; Huang, Y. *Carbon* **2013,** 55, 328-334.

139. Wang, H. G.; Wu, Z.; Meng, F. L.; Ma, D. L.; Huang, X. L.; Wang, L. M.; Zhang, X. B. *ChemSusChem* **2013,** 6, (1), 56-60.

140. Reddy, A. L. M.; Srivastava, A.; Gowda, S. R.; Gullapalli, H.; Dubey, M.; Ajayan, P. M. *ACS Nano* **2010,** 4, (11), 6337-6342.

141. John F. Moulder, W. F. S., Peter E. Sobol, Kenneth D. Bomben, *Handbook of X-ray photoelectron spectroscopy*. Physical Electronics USA, Inc.: Chanhassen, Minnesota, 1995.

142. Kabir, S.; Artyushkova, K.; Serov, A.; Kiefer, B.; Atanassov, P. *Surf. Interface Anal.* **2016,** 48, (5), 293-300.

143. Pint, C. L.; Sun, Z.; Moghazy, S.; Xu, Y.-Q.; Tour, J. M.; Hauge, R. H. *ACS Nano* **2011,** 5, (9), 6925-6934.

144. Share, K.; Cohn, A. P.; Carter, R.; Rogers, B.; Pint, C. L. *ACS Nano* **2016,** 10, (10), 9738-9744.

145. Das, A.; Chakraborty, B.; Sood, A. *Bull. Mater. Sci.* **2008,** 31, (3), 579-584.

146. Wei, D.; Liu, Y.; Wang, Y.; Zhang, H.; Huang, L.; Yu, G. *Nano Lett.* **2009,** 9, (5), 1752-1758.

147. Ma, C.; Shao, X.; Cao, D. *J. Mater. Chem.* **2012,** 22, (18), 8911-8915.

148. Ding, J.; Wang, H.; Li, Z.; Kohandehghan, A.; Cui, K.; Xu, Z.; Zahiri, B.; Tan, X.; Lotfabad, E. M.; Olsen, B. C. *ACS Nano* **2013,** 7, (12), 11004-11015.

149. Jian, Z.; Xing, Z.; Bommier, C.; Li, Z.; Ji, X. *Adv. Energy Mater.* **2016,** 6, (3), 1501874.

150. Zhang, C.; Mahmood, N.; Yin, H.; Liu, F.; Hou, Y. *Adv. Mater.* **2013,** 25, (35), 4932-4937.

151. Ling, C.; Mizuno, F. *Phys. Chem. Chem. Phys.* **2014,** 16, (22), 10419-10424.

152. Wang, X.; Zeng, Z.; Ahn, H.; Wang, G. *Appl. Phys. Lett.* **2009,** 95, (18), 183103.